DEVELOPMENT OF A BULK ACOUSTIC RESONATOR SENSING PLATFORM FOR CANCER BIOMARKER DETECTION

A Dissertation
Presented to
The Academic Faculty

By

Stephen J. Mobley

In Partial Fulfillment
of the Requirements for the Degree
Doctor of Philosophy
in
Electrical and Computer Engineering

School of Electrical and Computer Engineering
Georgia Institute of Technology
December 2015

DEVELOPMENT OF A BULK ACOUSTIC RESONATOR SENSING PLATFORM FOR CANCER BIOMARKER DETECTION

Approved by:

Dr. Pamela Bhatti, Committee Chair
Assoc. Professor, School of ECE
Georgia Institute of Technology

Dr. Paul Doetsch
Professor, Dept. of Radiation Oncology
Emory University

Dr. William Hunt, Advisor
Professor, School of ECE
Georgia Institute of Technology

Dr. James Stevenson Kenney
Professor, School of ECE
Georgia Institute of Technology

Dr. Oliver Brand
Professor, School of ECE
Georgia Institute of Technology

Date Approved: 06 August 2015

ACKNOWLEDGMENT

There are many individuals that I have to thank for the success of this project. I will attempt to keep it short, however the words written in this section are not enough to truly express my gratitude (also because I'm long winded...).

First, I would like to thank my advisor: Dr. William Hunt. At first I must admit, I wasn't too sure about working with his group and becoming a part of the Micro Acoustics Group (MAG). My background was computer engineering and their focus was microelectronics and in particular device physics, which was way out of my comfort zone. However, their goals of applying MEMS devices to solve issues facing the medical field was in line with my aspirations and therefore I dove in head first. Dr. Hunt takes a more hands-off approach and it was challenging during the process, but in the end rewarding. He has helped to develop my confidence in creating ideas from scratch and building them up one component at a time. He has also helped me broaden my scope from software development to microelectronics to circuit board layouts.

Next, I would like to thank all of the "old heads" of MAG. Dr. Adam Wathen, the coolest dude around that showed me the ropes of microelectronics and scared the living daylights out of me with background textbooks about the governing equations of our devices. Dr. Farasat Munir assisted me in finalizing my grasp of the group's work and working alongside me for fabricating the ZnO wafers. Also, he came up with the awesome characterization idea that I wish I had the time to develop. Dr. Ryan Westafer, always there to lead a helping hand and an expert (as far as I'm concerned) with the operation of all lab equipment. Even after getting done, he was just an email away working at GTRI and helping our group to explore the ideas of previous members. Drs. Desmond Stubbs, Sang-Hun Lee, Christoper Corso, and Anthony Dickherber, all of which I have met at one time or another. Each of them provided vital contributions to the group without which this project would not have been possible.

A short thanks to all the undergraduates of MAG; who although their time was short, each made their individual impacts. Sunil Yalamanchili, the business man that we drafted from the biomedical engineering department, who helped spearhead the ACμRay project and became a co-author of our joint publication with Emory. Stephen Mihalko, the longest and most committed undergraduate of the group. From designing automation software to attending conferences, he worked hard and I think he would make an awesome researcher. God bless you all in each of your endeavors!

Outside of MAG, many other individuals helped to make this work possible. To the "A-Team" of Oak Ridge National Laboratories: Joseph Dorris, Kim Phan, Travron Taylor, and Arianna Arevalo. You guys are awesome and the differential evolution optimization would not have been completed without your work. God bless each and every one of you on your career paths! Dr. Nashlie Sephus and Ivan Walker, thank you guys for your advice and direction about the field of pattern recognition. May God give you the strength and guidance to make a larger impact on society than you already have done!

A shout out to the men and women behind the scenes helping to keep the department together. The administrators of the ECE graduate office have come through with funding options for me at the last minute for almost every semester I've been at Tech. Also, to Jill and Julie of the ORS program. It was great working with you guys and if it wasn't for the positions that you provided for me semester after semester, I would not have been able to write this document. Thanks and God bless your program with favor, success, and influence for years to come.

To my family members, who have raised me to be the man that I am today. My mother, Cheryl Mobley, I know we haven't always seen eye to eye but you have been my inspiration since I was young. Fearless and determined, you were willing to do what it takes to get the job done for your kids. It is that drive and your faith in God that has illustrated the essentials of overcoming any difficult trial (such as a PhD at GA Tech). My brother, Jonathan Mobley, we have been partners in crime since your birth! You still encourage me to go big in all that

I do, so that I can continue to be a role model for you. Keep focusing on the Lord and let him use you for your pharmacy degree! And to my new family members, Elizabeth George and all the brothers of the Girma family. Although I've known you for but a short time, it seems like I've been a part of your family forever. Thanks for all the love and support and I will serve you guys as your brother/son-in-law for the rest of my days.

I was told that by an older student that you go to graduate school in order to get married. And in my experience, I think that the statement is true. God has truly blessed me with my beautiful wife, Feben Girma. "He who finds a wife finds a good thing, and obtains favor from the Lord" Prov. 18:22. This statement rings very true for my situation. God used my wife to motivate me and push me out of my lazy "I'll do it tomorrow" ways, developed my pursuit of God ,and has taught me more about how to love. I love you baby, and we will continue to grow deeper in our affection for one another.

And last but not least, the Holy Spirit. The Bible says that God is the "Author and Finisher of our faith" Hebrews 12:2. You are so gifted at the way that You write the stories of our lives. You know that I'm more of a team player and yet You lead me to a group in which all the other graduate students left right after I got my feet wet. All for the purpose of developing my dependency on You as the source of my understanding. You have even pointed out specific technical issues, such as the time You revealed to me that the helium cooling system was down for the evaporator that I had absolutely no clue about. May this project serve as a mere stepping stone to a deeper and more intimate relationship with You while I'm here on this earth. All glory and honor to Jesus Christ my Lord!

TABLE OF CONTENTS

LIST OF TABLES

LIST OF FIGURES

SUMMARY

Cancer is one of the leading causes of death for patients within the United States and throughout the world. When diagnosed in early growth stages, tumors (regions of uncontrolled cell division) can be more effectively treated and patients are more likely to survive. Therefore, the development of screening technology for early detection of cancer is essential to improve patient survival rates and serves as the motivation for this work.

The objective of this dissertation is the design and implementation of a sensing platform for the detection of cancer biomarkers within aqueous patient samples. The system's transducer is based on previously developed zinc oxide (ZnO) bulk acoustic wave (BAW) resonators that are capable of exciting multiple types of acoustic modes.

Chapter 1 presents the motivation for this work along with a short review of gravimetric biosensors used in aqueous applications. Chapter 2 focuses on the history, theoretical derivation, and fabrication protocol for the system transducers and array configuration. In Chapter 3, the Universal Serial Bus (USB) is examined as a potential radio frequency bus for device characterization of MEMs devices. Chapter 4 presents the optimization of a module design for isolating the circuitry from the fluidics pathways for sample exposure. Combining the work of the previous chapters, Chapter 5 validates the ability of the designed system to serve as a biosensing platform. Each individual sensor is functionalized with antibodies selectively binding the desired biomarker. Lastly, Chapter 6 demonstrates a protocol for extracting features from raw sensor data to develop classification models. Thus, providing diagnostic information about the sample exposed to the device.

CHAPTER 1

INTRODUCTION

1.1 Cancer Research

Cancer is a category of disease types in which cells begin to multiply uncontrollably resulting in a growth known as a tumor. Tumors are classified into different developmental stages ranging from benign to malignant; at which point, ordinary bodily functions are inhibited, for example, blood flow and oxygen uptake. The initial cause of this abnormal cell growth can range from genetics, prolonged exposure to carcinogens, and other unknown causes. According to the 2012 cancer statistics, over 1.6 million new cancer diagnosis are discovered each year, and over 550,000 American patients die each year because of the complications stemming from cancer [1]. Figure 1 shows the survival rates for American patients over a five year period (starting in 2002) for select types of cancer (named based on the initially afflicted organ system). An observation from Figure 1 is that an earlier initial diagnosis of the disease tends to lead to higher survival rates for each patient. This trend is attributed to increased efficacy of treatment options, for instance, chemo therapy, radiation, or surgery. Therefore, the development of systems and protocols capable of offering early diagnostic information are essential for increasing patient survival rates.

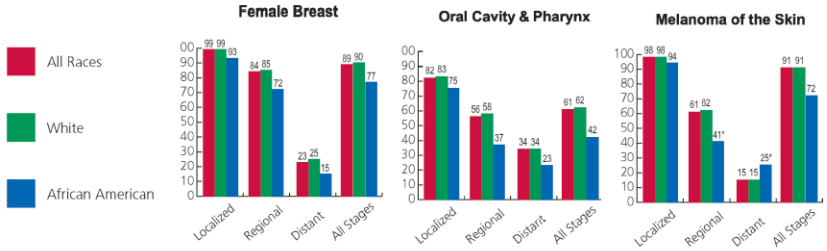

Figure 1: Five year study of cancer patient initial diagnostic stage vs. survival rate [1].

For cancers, diagnostic assessment of a patient's symptoms by a health professional is the predominant means of disease diagnosis. However, as symptoms begin to manifest, the tumor growth is usually in its later stages and has begun to affect the function of major

biological systems. Another approach is by physical examination, for instance, palpating for lumps within different regions of the body. This process alludes to the fact that the tumor is close enough to the surface to be noticed and is large enough to seem abnormal. Technological advances have allowed for health professionals to perform more comprehensive studies with deep tissue imaging such as magnetic resonance imaging (MRI) and computerized tomography (CT). However, because of their cost and technical complexity, these systems are primarily utilized as a means to confirm a potential diagnosis rather than for regular screening.

Therefore, low-cost screening protocols have been developed to proactively detect diseases in early stages by examining patient samples. One such process is the enzyme-linked immunosorbent serum assay (ELISA), which is conducted in a 96-well petri dish tray wherein desired antigens, known as biomarkers whose presence may indicate disease, are assessed. Antibodies immobilized on the surface of each well bind these biomarkers and are subsequently bonded by another florescence tagged antibodies for result assessment [7]. However, results are based on the optical density (e.g. color) for each well which results in poor resolution and detection limits [8]. Therefore, a wide range of biosensing platforms have been developed in order to provide both an analytic and quantitative approach to patient screening.

1.2 Sensor Types

Biological sensing platforms contain each of the components outlined in Figure 2. The analyte or biomarker is the target molecule that provides the desired analytical information, for instance, disease diagnosis. The surface chemistry or sensing layer serves as the intermediate between the sensor and the biological environment. This layer is responsible for selectively binding to the target molecule and repelling any undesired interactions. The transducer amplifies and converts the biological binding event into an electrical signal, which requires further processing in order to determine the desired analytical information

[9].

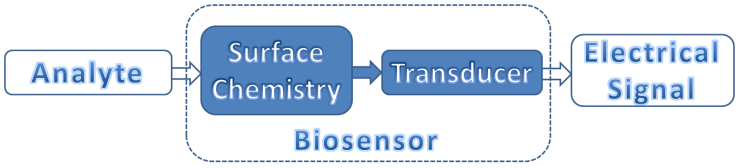

Figure 2: Components of biosensing platforms.

Biosensing platforms are categorized by their transduction system and have been separated into four categories [10]. Electrochemical sensors monitor changes in the electrical properties of the chemical environment. This class of sensors is further divided into one of three subcategories: amperometric, potentiometric and conductimetric; which monitor changes in current, voltage and capacitance respectively. Optical sensors utilize a lighting source to examine the desired region. This assessment can be via direct analysis, in which the optical signal provides the analytical data, or indirectly, by using the light source to induce a phenomenon that extracts the desired information. Thermal sensors convert temperature changes into electrical signals. The source of the thermal energy can be caused by the biological recognition event or indirectly by another process that can serve as a biomarker. However, this sensor platform is not widely used for aqueous applications because of the large heat capacity of the surrounding environment which drastically reduces the device's sensitivity. Mass or gravimetric sensors convert mechanical stress caused by surface loading into electrical signals. Gravimetric sensors are the category for the transducer of this work and are further discussed in the following sections.

1.3 Gravimetric Sensors

Gravimetric sensors can be operated with either passive or active excitation. Passive operation relies on the structure of the device containing either a type of deformation or vibrational mode that is modified by mass loading. Additionally, these devices require some

form of transducer to convert the loading event into an electrical signal for proper characterization. Active devices excite vibrational modes within a predetermined sensing area by an input electrical signal. For active devices, the transducer can both excite and characterize the device simultaneously. The following sections provide a short review of current and past gravimetric sensing platform technologies. We limit our examples to biosensing platforms applied to protein or cell detection within an aqueous environment.

1.3.1 Microcantilevers

Microcantilevers are suspended bridge-like structures designed based on composite beam theory. These devices can be both passively and actively excited; additionally, they can be utilized in either deflection (static) or resonant (dynamic) operational modes.

Dynamic mode relies on the eigenfrequencies of the beam motion that becomes detuned upon the adsorption of mass on the device's surface. However, the majority of the particle displacement is transverse to the plane of the cantilever; therefore, mechanical energy leaks into the surrounding aqueous environment, causing a reduction in the resonator's quality factor or Q factor. Static mode devices monitor the deflection of the cantilever caused by a change in the surface energy of the beam which is sensitive to mass adsorption. Static mode devices are more widely used for aqueous biosensing, as they do not rely on mechanical energy trapping for proper operation.

Yen et al. developed V-shaped microcantilevers using static operation for the study of antibody immobilization [11]. Utilizing the charged properties of proteins, they designed a fluidics cavity in which applied electric fields increase the surface density of immobilized antibodies. Ricciardi et al. developed a biosensing platform for the detection of Angiopoietin-1 tumor marker with an active cantilever system [12]. Devices were excited via a piezoelectric disk and separately characterized by an optical laser deflected to a position sensitive device (PSD). Comprehensive review articles have been published for microcantilevers used in biosensing applications [13, 14].

1.3.2 Capacitive Membrane Devices

Capacitive micromachined ultrasound transducers (CMUT) are resonate structures that contain an array of electrostatically actuated plates supported by isolating posts with a sealed vacuum cavities [15]. Device operation is based on the deformation of the top layer of the membrane and the existence of a resonance mode based on the restorative forces in the device. Therefore, both the capacitance (or impedance) and the resonant frequency of the device can be monitored in real time and correlated to mass adsorption on the surface. The cavity deformation is caused by the pressure difference between the membrane to the surrounding environment and a bias voltage applied to the top and bottom of the device.

Ramanaviciene et al. first used CMUT devices for biosensing applications [16]. They monitored shifts in the resonant frequency (12 MHz) and the real part of the impedance with the binding of bovine leukemia virus antigen gp51. Later, Virzonis et al. developed two types of CMUT devices, high frequency (40 MHz) and low frequency (7 MHz), for the detection of the same anitgen (bovine leukemia virus gp51), using two different surface functionalization [15]. They used these results to assess each devices sensitivity and influences caused by the surface functionalization for sensing applications.

1.3.3 Acoustic Wave Sensors

Acoustic wave sensors utilize a piezoelectric film to excite vibrational waves within the dimensions of the device. The two types of acoustic wave devices are surface acoustic wave (SAW) and bulk acoustic wave (BAW). Each type is named based on the primary wave mode propagating through the device. Additionally, acoustic wave devices require proper orientation of the applied electric field to the existing dipoles within the piezoelectric substrate. These dipoles can either be applied in ferromagnetic materials or naturally occurring in select crystalline substrates, e.g., quartz (SiO_2) and aluminum nitride (AlN). Some device titles will also specify the growth orientation of the piezoelectric film, as this substrate property is essential to excite particular wave types.

1.3.4 Shear Horizontal SAW

A majority of SAW devices have particle displacement normal to the plane of the substrate. As mentioned earlier, this diminishes sensor performance in aqueous solutions. Shear horizontal SAW (SHSAW) devices primarily have particle displacement in the plane of the substrate and transverse to the wave propagation direction [17]. Waves are excited by a piezoelectric interdigitated transducer (IDT) and propagate to an output transducer.

Berkenpas et al. developed a Langasite ($La_3Ga_5SiO_{14}$) SHSAW device with waves propagating along the Euler angles of the substrate [18]. They used the devices to detect Escherichia coli with self-assembling monolayer (SAM) immobilized antibodies using both a drop-dry and flow through technique. Perng et al. developed an RFID-tagged SHSAW device with Lithium Niobate ($LiNbO_3$) IDTs operating at 220 MHz [19]. They demonstrated the ability to detect FITC molecules with antibodies immobilized by a SAM.

1.3.5 Love wave devices

Love mode SAW devices require a crystalline substrate that is capable of exciting a surface skimming bulk wave (SSBW) in which reflected bulk waves do not interfere with the device performance [17]. The majority of the particle displacement is in the plane of the device surface, making these devices ideal for biosensing applications.

Fertier et al. developed an AT-cut quartz love mode SAW device for the detection of Murine antibodies [20]. Moll et al. used 3-glycidoxypropyl trimethoxysilane (GPTS) for the detection of Escherichia coli with an AT-cut quartz love mode SAW operating at 118 MHz [21]. Both devices were excited and monitored in real time using an oscillator loop with electrical feedback to compensate for the insertion loss of the wave within the sensing area. Kalantar-Zadeh et al. developed two types of love mode SAW devices (ZnO/90^o rotated and SiO_2/90^o rotated) to monitor the adsorption of antibodies [22]. Both devices were characterized by a feedback loop with a broadband amplifier and reference sensor.

1.3.6 Quartz Crystal Microbalance

Quartz Crystal Microbalance (QCM) are the most commonly used form of bulk acoustic resonators for sensing applications, for example, analytical chemistry and fabrication technology process monitoring. The majority of QCMs have two electrodes on either side of an AT-cut or BT-cut quartz crystal to excite shear bulk waves within the cavity of the device. The resonant and/or harmonic frequencies are then monitored via electrical characterization. Any shifts in these frequencies can then be correlated to mass adsorption using equations such as the one developed by Sauerbrey in 1959 [23]. QCMs have been applied to many aqueous biosensing applications and a comprehensive review has been compiled to summarize the both commercially available systems and current research trends [24].

In 1998, Hook et al. developed a process for assessing both mass and elastic properties of biological films by examining both resonant frequency shifts and energy dissipation in QCM devices [25]. This work along with other developments led to the design of Boston Scientific's Q-Sense platform. The Q-Sense system utilizes quartz crystal microbalance with dissipation (QCM-D) transduction devices. The system includes individual flow chambers which isolate each sensor and gives the user control of environmental parameters. Each device is characterized by an impulse excitation system using a ring-down technique. This technique involves oscillator circuitry that excites the QCM-Ds with short pulse AC signals in order to monitor the reflected signal for formulating the S_{11} parameters and energy dissipation [26]. The Q-Sense system has been used to conduct studies in many different fields, e.g., surface chemistry, food industry, and pharmaceuticals.

1.3.7 Thin Film Bulk Acoustic Resonator

Thin film bulk acoustic resonators (TFBAR) are a type of gravimetric sensor in which are capable of operating in the GHz range with cavity thicknesses on the order of hundreds of nanometers. Several studies have been conducted utilizing these devices for aqueous biosensing applications. Wingquist et al. developed a c-axis AlN TFBAR micro-fluidics sensing platform for the detection of narcotic drugs such as cocaine and heroin [27]. They

used a competitive binding approach, in which antibodies would release an immobilized synthetic antigen with lower binding affinity and bind the target molecule. Yan et al. developed a ZnO TFBAR system operating at 3.94 GHz for real-time monitoring of an antibody sandwich [28]. This category of devices serves as the focus of this work, as we look to develop a ZnO TFBAR sensing platform for the simultaneous detection of multiple cancer biomarkers for patient screening and diagnostic applications. There are several type of TFBAR devices with different methods for isolating acoustic energy such as etching an air cavity below the device. For this study, we have developed a solidly mounted resonators (SMR) with an acoustic reflector to emulate an air boundary for proper device performance.

CHAPTER 2

DEVELOPMENT AND FABRICATION OF ZINC OXIDE SURFACE MOUNT RESONATORS

2.1 Piezoelectric Resonator Background

Piezoelectric materials are structures that exhibit internal stress and strain when exposed to an electromagnetic field. This phenomenon was first discovered by Pierre and Jacques Curie back in 1880 [29]; however, wide spread application of the technology as devices started in the 1920s with the advent of the quartz crystal oscillators. Materials capable of exhibiting piezoelectricity can be either ferroelectrics such as lead zirconate titanate (PZT) or non-ferroelectric polar crystalline structures such as aluminum nitride (AlN) or zinc oxide (ZnO).

For non-ferroelectric materials, crystalline growth orientation with respect to the electric excitation fields is an important design consideration. These devices depend on the presence of inherit bond dipoles within the lattice. Figure 3 shows an example of a hexagonal unit cell for piezoelectric materials [2]. The arrows illustrate the movement of individual atoms within the lattice when an external electric field is applied.

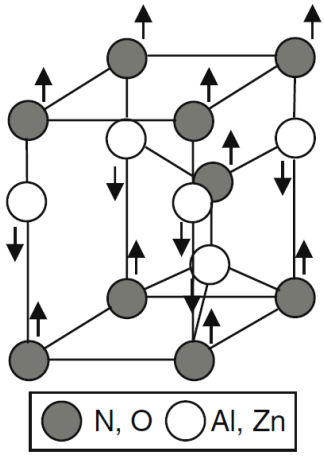

Figure 3: Hexagonal unit cell for ZnO and AlN Crystalline structures [2].

The discover of piezoelectricity has lead to the design of several types of electromechanical devices, for example, transducers and resonators. Resonators are devices that oscillate at specific frequencies depending on several factors such as cavity thickness, substrate material properties, and mechanical boundary conditions. MEMs resonators are derived from several device types such as microcantilevers, surface acoustic wave (SAW) and bulk acoustic wave (BAW) devices, which were discussed earlier in Section 1.3.

2.1.1 Resonator Modeling

In 1959, Sauerbrey develop an equation (1) correlating mass deposition on the surface of a quartz crystal microbalance (QCM) sensor to the shift in the device's resonant frequency [23].

$$\Delta f = \frac{-2f_o^2 \Delta m}{A\sqrt{\rho_q \mu_q}} \tag{1}$$

ρ_q is the density of quartz, μ_q is the stiffness of the crystal, A is the surface area of the resonator and f_o is the unloaded resonance frequency. Δf is a shift in the resonant frequency and Δm is the mass adsorbed to the surface of the device.

However, the Sauerbrey equation makes the assumption that the loaded mass has the same density as the underlining quartz substrate. For biological detection applications, this is an improper assumption as the density of loaded particles can be orders of magnitude less dense than that of quartz, for example, proteins and cells. Also, stiffness and viscosity changes are not taken into account and can lead to improper signal analysis.

Hunt et al. developed a model that incorporates both the viscosity and stiffness of the loaded membrane for biological sensing applications [30]. Assuming that the absorbed film properties do not vary with time, the Hunt equation reduces to the form seen in equation (2) resembling the Sauerbrey equation.

$$\Delta f = \frac{-2f_o^2 h_f}{\sqrt{\rho_q \mu_q}} \left[\Delta\rho_f - \frac{\Delta\mu_f}{V_s^2} \right] \tag{2}$$

However, instead of just a change in loaded mass, it takes into account changes in film density ($\Delta\rho_f$) and stiffness ($\Delta\mu_f$) based on the thickness of the film (h_f). V_s is the velocity

of a shear acoustic wave.

Mechanical and electrical properties of an acoustic resonator can also be represented as electrical circuit components for simulation. The Butterworth-Van Dyke (BVD) model consists of four electrical components to simulate the series and parallel frequencies of a cavity resonator [31, 32] (Fig. 4). C_o is the static capacitance, R represents energy lost into the surrounding environment, L correlates to the mass and density of the device and C_a is the vibrational energy or stress within the cavity of the resonator. Each component value is derived based on the material properties and vibrational modes of the resonator [33]. However, this model lacks a representation of changes within the mechanical boundary conditions for sensors within various sensing environments.

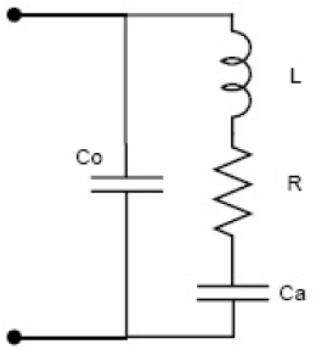

Figure 4: BVD circuit model for resonators.

Ballato developed a circuit model that incorporates mechanical ports for both longitudinal and shear mass loading events for resonators [3]. Additionally, the model includes an electrical port to account for the piezoelectric coupling of the electrical and mechanical energy. Transmission line (TL) models are used to simulate the acoustic wave propagation within the cavity of the resonator. TL parameters are defined based on wave speed of the device's vibrational mode and other physical properties such as cavity thickness. This model can be modified for simulating multi-mode, piezoelectric, piezomagnetic, and other types of resonator structures [3]. Figure 5 shows the circuit model in which ports

1-6 are mechanical ports for simulating different types of mass loading (shear and longitudinal). Port 7 is the electrical port for the excitation and response signal and each of the transformers represent the piezoelectric coupling factor of the transducer.

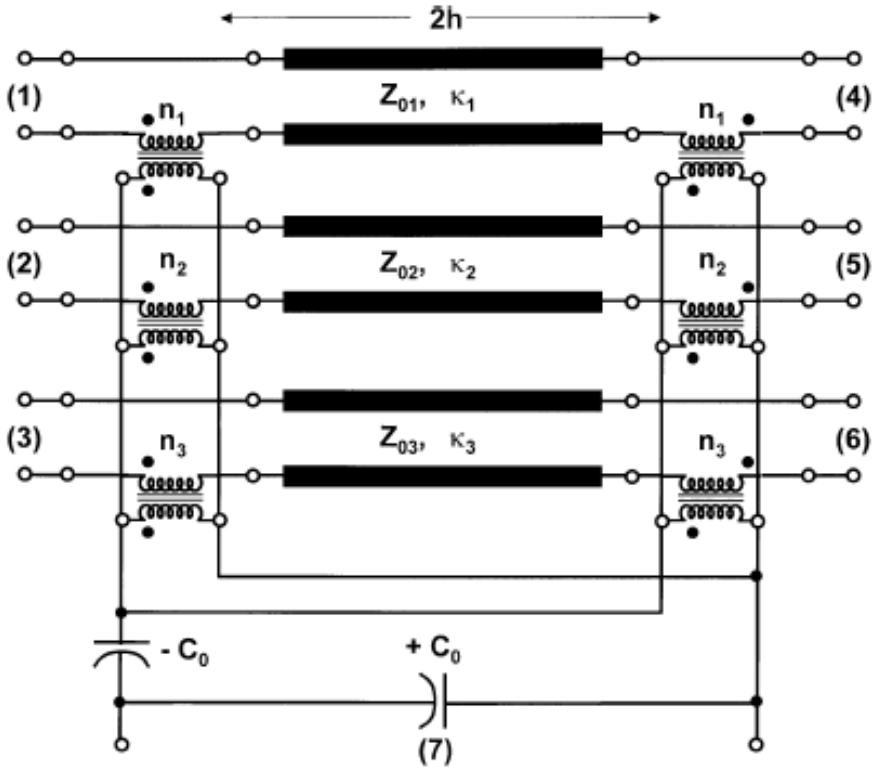

Figure 5: Ballato circuit model for resonators [3].

2.2 Theoretical Derivation

2.2.1 Longitudinal and Shear Vibrational Modes

For theoretical derivation of the device operation of BAW ZnO resonators, we look to determine the existent of both pure longitudinal and shear vibrational modes. We start with the stress tensor for a three dimensional space (equation (3)) and the electrical field vector derived from a scalar applied potential (Φ) (equation (4)). u is the particle displacement vector.

$$\mathbf{S} = \nabla_s \mathbf{u} = \begin{bmatrix} \frac{\partial u_1}{\partial x_1} \\ \frac{\partial u_2}{\partial x_2} \\ \frac{\partial u_3}{\partial x_3} \\ \frac{\partial u_2}{\partial x_3} + \frac{\partial u_3}{\partial x_2} \\ \frac{\partial u_1}{\partial x_3} + \frac{\partial u_3}{\partial x_1} \\ \frac{\partial u_1}{\partial x_2} + \frac{\partial u_2}{\partial x_1} \end{bmatrix} \tag{3}$$

$$\mathbf{E} = -\nabla \mathbf{\Phi} = \begin{bmatrix} -\frac{\partial \Phi}{\partial x_1} \\ -\frac{\partial \Phi}{\partial x_2} \\ -\frac{\partial \Phi}{\partial x_3} \end{bmatrix} \tag{4}$$

As mentioned previously, ZnO crystal has hexagonal symmetry and therefore the material property tensors reduce to the following forms [34].

$$
\begin{aligned}
\mathbf{c}^{\mathbf{E}} &= \begin{bmatrix} c_{11} & c_{12} & c_{13} & 0 & 0 & 0 \\ c_{11} & c_{11} & c_{13} & 0 & 0 & 0 \\ c_{13} & c_{13} & c_{33} & 0 & 0 & 0 \\ 0 & 0 & 0 & c_{44} & 0 & 0 \\ 0 & 0 & 0 & 0 & c_{44} & 0 \\ 0 & 0 & 0 & 0 & 0 & c_{66} \end{bmatrix} \\
\mathbf{e} &= \begin{bmatrix} 0 & 0 & 0 & 0 & e_{15} & 0 \\ 0 & 0 & 0 & e_{15} & 0 & 0 \\ e_{31} & e_{31} & e_{33} & 0 & 0 & 0 \end{bmatrix} \\
\epsilon^{\mathbf{S}} &= \begin{bmatrix} \epsilon_{11} & 0 & 0 \\ 0 & \epsilon_{11} & 0 \\ 0 & 0 & \epsilon_{33} \end{bmatrix}
\end{aligned}
\tag{5}
$$

$\mathbf{c}^{\mathbf{E}}$ is the stiffness tensor under a constant electric field, $\mathbf{e}$ is the piezoelectric coupling factor, and $\epsilon^{\mathbf{S}}$ is the permittivity tensor under constant stress.

We assume that our device operation is under isothermal conditions; therefore, equations (6) serve as the constitutive equations for piezoelectric materials derived from Gibbs free energy [35].

$$
\begin{aligned}
\mathbf{T} &= \bar{\mathbf{c}}^{\mathbf{E}} \cdot \mathbf{S} - \bar{\mathbf{e}} \cdot \mathbf{E} \\
\mathbf{D} &= \mathbf{e} \cdot \mathbf{S} - \epsilon^{\mathbf{S}} \cdot \mathbf{E}
\end{aligned}
\tag{6}
$$

$\mathbf{T}$ is the stress tensor and $\mathbf{D}$ is the electric displacement vector.

We reduce the problem into two-dimensional space as seen in Figure 6. Therefore, there is no particle displacement (i.e. $u_2 = 0$) or field variation (i.e. $\partial/\partial x_2 = 0$) within the axis of x_2.

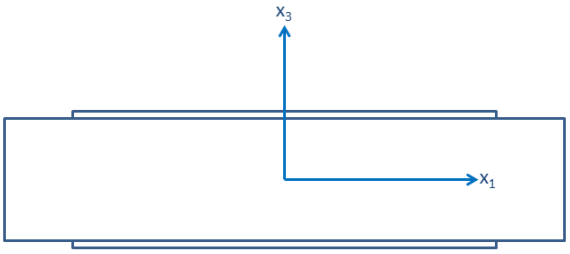

Figure 6: Coordinate axis for resonator.

Plugging each of the parameters (equation (5)) into the constricting equations (equation (6)) and removing any terms with respect to the x_2 axis results in the following stress tensor and electrical displacement vector.

$$\mathbf{T} = \begin{bmatrix} c_{11}\frac{\partial u_1}{\partial x_1} + c_{13}\frac{\partial u_3}{\partial x_3} + e_{31}\frac{\partial \Phi}{\partial x_3} \\ c_{12}\frac{\partial u_1}{\partial x_1} + c_{13}\frac{\partial u_3}{\partial x_3} + e_{31}\frac{\partial \Phi}{\partial x_3} \\ c_{13}\frac{\partial u_1}{\partial x_1} + c_{33}\frac{\partial u_3}{\partial x_3} + e_{33}\frac{\partial \Phi}{\partial x_3} \\ 0 \\ c_{44}\frac{\partial u_1}{\partial x_3} + c_{44}\frac{\partial u_3}{\partial x_1} + e_{15}\frac{\partial \Phi}{\partial x_1} \\ 0 \end{bmatrix} \tag{7}$$

$$\mathbf{D} = \begin{bmatrix} e_{15}\frac{\partial u_1}{\partial x_3} + e_{15}\frac{\partial u_3}{\partial x_1} - \epsilon_{11}\frac{\partial \Phi}{\partial x_1} \\ 0 \\ e_{31}\frac{\partial u_1}{\partial x_1} + e_{33}\frac{\partial u_3}{\partial x_3} - \epsilon_{33}\frac{\partial \Phi}{\partial x_3} \end{bmatrix} \tag{8}$$

Applying both Newton's second law of motion (equation (9)) and Gauss's law (equation (10)) to the these results and assuming harmonic operation gives us the governing equations for acoustic waves within a piezoelectric cavity in the x_1-x_3 plane (equations (11)).

$$\nabla \cdot \mathbf{T} = \rho \frac{\partial^2 \mathbf{u}}{\partial t^2} \tag{9}$$

$$\nabla \cdot \mathbf{D} = 0 \tag{10}$$

$$
\begin{aligned}
c_{11}\frac{\partial^2 u_1}{\partial x_1^2} + (c_{13}+c_{44})\frac{\partial^2 u_3}{\partial x_1 \partial x_3} + (e_{31}+e_{15})\frac{\partial^2 \Phi}{\partial x_1 \partial x_3} + c_{44}\frac{\partial^2 u_1}{\partial x_3^2} &= -\rho\omega^2 u_1 \\
c_{44}\frac{\partial^2 u_3}{\partial x_1^2} + (c_{44}+c_{13})\frac{\partial^2 u_1}{\partial x_1 \partial x_3} + e_{33}\frac{\partial^2 \Phi}{\partial x_3^2} + e_{15}\frac{\partial^2 \Phi}{\partial x_1^2} + c_{33}\frac{\partial^2 u_3}{\partial x_3^2} &= -\rho\omega^2 u_3 \\
(e_{15}+e_{31})\frac{\partial^2 u_1}{\partial x_1 \partial x_3} + e_{15}\frac{\partial^2 u_3}{\partial x_1^2} + e_{33}\frac{\partial^2 u_3}{\partial x_3^2} - \epsilon_{11}\frac{\partial^2 \Phi}{\partial x_1^2} - \epsilon_{33}\frac{\partial^2 \Phi}{\partial x_3^2} &= 0
\end{aligned}
\tag{11}
$$

For the devices in this study, we desire to excite both pure longitudinal and pure shear modes also known as thickness excitation (TE) and thickness shear modes (TSM). For pure TSM, particle displacement would be completely along the x_1 axis (i.e. $u_3 = 0$) with no wave variations (i.e. $\partial/\partial x_1 = 0$). Incorporating these assumptions into equation (11) reduces to the following (equation (12)), which is the TSM wave equation.

$$
c_{44}\frac{\partial^2 u_1}{\partial x_3^2} = -\rho\omega^2 u_1 \tag{12}
$$

For pure TE, we now assume that all particle displacement is along the x_3 axis (i.e. $u_1 = 0$) and that again there are no field variations along the x_1 axis (i.e. $\partial/\partial x_1 = 0$). Plugging these assumptions into equation (11) results in the following:

$$
c_{33}\frac{\partial^2 u_3}{\partial x_3^2} + e_{33}\frac{\partial^2 \Phi}{\partial x_3^2} = -\rho\omega^2 u_3 \tag{13}
$$

Next, we plug these same assumptions into equation (11) in order to solve for the $\partial^2\Phi/\partial x_3^2$ term.

$$
e_{33}\frac{\partial^2 u_3}{\partial x_3^2} = \epsilon_{33}\frac{\partial^2 \Phi}{\partial x_3^2} \tag{14}
$$

Plugging this back into the equation (13), we get the following (equation (15)) which is the TE wave equation.

$$
\left(c_{33} + \frac{e_{33}^2}{\epsilon_{33}}\right)\frac{\partial^2 u_3}{\partial x_3^2} = -\rho\omega^2 u_3 \tag{15}
$$

2.2.2 Hybrid Mode

Wathen et al. [36] observed the existence of a hybrid operational mode within ZnO BAW device that are capable of exciting both TE and TSM waves. The governing equations for these devices are show in equations (11). However, this mode is known to have both

longitudinal and shear particle displacement, therefore assumptions of particle displacement do not apply. Additional experimental and theoretical work would need to be done to determine the coupling factor between particle displacement and applied potential along multiple axes.

2.2.3 Acoustic Energy Trapping

Proper electric field orientation with respect to the lattice structure of the piezoelectric material is necessary for the excitation of certain vibrational modes. Additionally, for proper resonator operation, acoustic or mechanical energy must be trapped within the cavity of the device rather than propagating into the surrounding environment.

For sensing applications, device sensitivity is directly correlated to operational frequency. However, resonant frequency is inversely correlated to cavity thickness. In order to achieve higher resonant frequencies, the device thickness must decrease, which gives rise to fragility.

Munir et al. utilized an acoustic reflector built up on the surface of a support silicon wafer to emulate an acoustic wave boundary close to air [4]. They achieve this by depositing layers of alternating mechanical properties; layers of both high (Tungsten W) and low (quartz SiO_2) acoustic impedance.

As reported in [37], for acoustic reflectors with two quarter wavelength layers, the input impedance observed by a vibrational wave is seen in equation (16). For a six layer stack on top of silicon substrate would have the form of equation (17).

$$Z_{in} = Z_N \frac{Z_N}{Z_{N-1}} \tag{16}$$

$$Z_{in} = Z_l \cdot \frac{Z_l}{Z_h} \cdot \frac{Z_l}{Z_h} \cdot \frac{Z_l}{Z_h} \cdot \frac{Z_{Si}}{Z_h} \tag{17}$$

Z_{in} is the acoustic impedance seen at the boundary, Z_N or Z_l is the impedance of quartz layer, Z_{N-1} or Z_h is the impedance of the tungsten layer, and Z_{Si} is the impedance of the underlining silicon substrate.

Munir et al. [4] utilized a Matlab® script to simulate the resultant reflection coefficient at the boundary of the reflector with respect to various thicknesses of ZnO. In an effort to define cavity heights capable of sustaining both TE and TSM modes (Fig. 7). This result provides the desired thickness for the piezoelectric region (1125nm ± 80nm) with a quartz layer (1000nm) and tungsten layer (640nm).

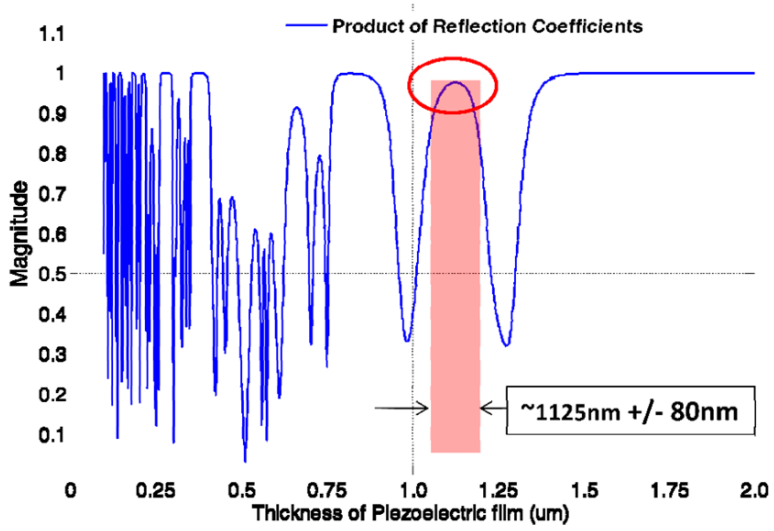

Figure 7: Resultant acoustic reflection coefficient for both TE and TSM modes in a six layer reflector stack [4].

2.3 Design Considerations

2.3.1 Device Types

Munir et al. [4] developed a multi-mode device which is capable of sustaining both TE and TSM vibrational modes based on the wave equations and energy trapping methods presented in Section 2.2. These devices are also capable of exciting a third hybrid vibrational mode that contains portions of TE and TSM vibrational modes.

Corso et al. [38] developed a ZnO solidly mounted resonator (SMR) lateral field excitation (LFE) device. These devices are capable of exciting a pure TSM resonance within the cavity of the device. TSM devices are advantage to TE devices within aqueous applications, because of the fact that solutions are capable of sustaining longitudinal acoustic

waves. Therefore, TE resonators tend to leak energy into the surrounding environment and this leads to a decrease the Q factor.

2.3.2 Array Configuration

For the detection of biomarkers, devices must be individually functionalized for a particular antigen. Device functionalization will be further expounded upon in Section 5.2. Even with proper functionalization and specificity for a particular biomarker, there are still environmental factors that may alter the device's response. Several examples of such environmental factors can be temperature changes, competitive bonding of antibodies, and other interferants within the sample under test. In order to reduce the effects of these environmental factors, a reference sensor, either functionalized for a biomarker that will not be present in the sample or with no functionalization layer, must be exposed to the sample simultaneously with all other sensors.

Additionally, utilizing only one biomarker may lead to a false diagnosis of a disease. Even a well-established biomarker, for instance, Prostate Specific Antigen (PSA) has come under recent scrutiny for accuracy in the diagnosis of prostate cancer [39]. Therefore, it is essential that an array of devices functionalized for multiple biomarkers are expose to the same environmental parameters simultaneously.

Figure 8 shows both the layout and actual array configuration of the devices designed and fabricated by the author. Figure 8a show the array configuration of the staggered LFE devices (400μm x 400μm) and Figure 8b shows the scaled size of the multi-mode devices (400μm x 400μm). Each device would be individually functionalized to detect a different type of biomarker. The excitation circuitry for each device connects with bonding pads that are on the edges of the wafer die. The circular shape in Figure 8a,b is the region in which SU-8 photoresist interacts with an O-ring order to isolate the aqueous solution from the electronics of the circuit. The following section is the fabrication steps in which the author followed in order to create the devices.

(a)

(b)

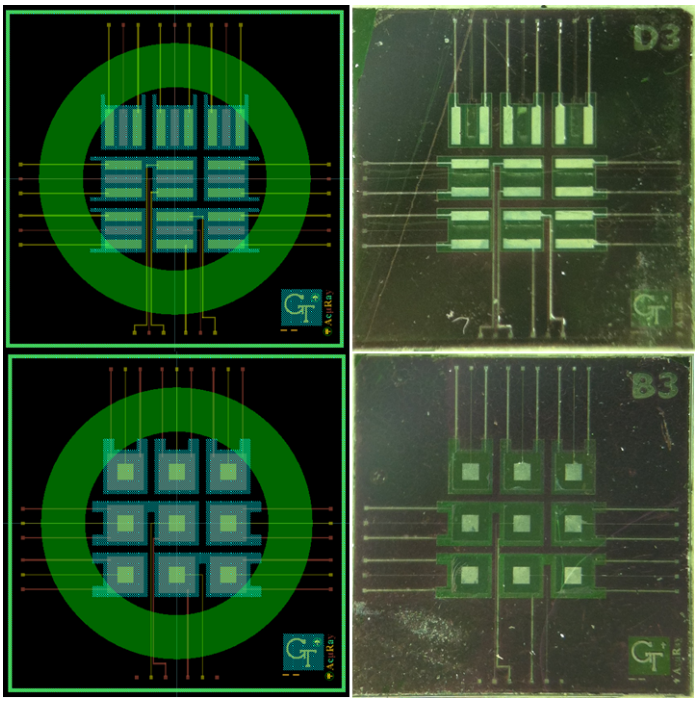

Figure 8: Design and real images of (a) LFE and (b) multi-mode devices.

2.4 Fabrication Protocol

Each device was constructed first by building up the acoustic reflector and then patterning the electrodes and piezoelectric regions. Each layer was deposited by DC and RF sputtering using a Unifilm PVD-300 sputtering system. All W layers were 640 nm thick and SiO_2 layers were 1 μm thick according to the simulation results presented in Section 2.2.3. Table 1 denotes the sputtering parameters used for depositing each layer of the acoustic reflector along with the piezoelectric layer (ZnO).

Table 1: Sputtering parameters for several layers.

Material	Tungsten	Quartz	Zinc Oxide
Power (Watts)	0.86 DC	281 RF	142 RF
Oxygen Gas	N/A	2.5%	3%
Argon Gas	100%	97.5%	97%
Temperature	20°C	20°C	325°C
Pressure	$\approx 5.00 \cdot 10^{-3}$ Torr		
Deposition Rate	300 nm/sec		

For the patterning of the electrode layers, lift-off lithography was utilized, in which

a positive photoresist layer (Microposit SC1805) where first patterned and cured prior to deposition of the electrode material (aluminum Al). The photoresist was then subsequently chemically etched away by acetone leaving only the desired electrode pattern remaining. The electrode material was deposited by a CVC E-Beam Evaporator.

The piezoelectric layer requires a high quality crystalline structure. Martin et al. developed a protocol for the crystalline growth of AlN utilizing a heated sputtering system [40], and Krishnaswamy et al. optimized that protocol for the growth of c-axis (normal to the plane of the substrate) ZnO [41]. Table 1 denotes the sputtering parameters used for the deposition of the ZnO piezoelectric material. The layer is then patterned with photoresist and exposed for a set time to an acidic solution according to the reaction seen in equation (18) [42].

$$ZnO + 2H^{+} \rightarrow ZnO^{2+} + H_2O \tag{18}$$

The process parameters for both types of photoresist and chemical etchants are outlined in Table 2.

Table 2: Chemical processing for photoresist and etching.

Photoresist						
Name	Spin Coat	Thickness	Prebake	Exposure	Soft Bake	Developer
Futurrex NR9-1500PY	1000 rpm for 40 sec	$\approx 2.5\mu m$	150^oC for 5 min	365 nm for 60 sec	100^oC for 5 min	RD-6 for 30 sec
Microposit SC1805	4000 rpm for 30 sec	$\approx 0.5\mu m$	100^oC for 2 min	405 nm for 3 sec	100^oC for 2 min	MF-319 for 60 sec
Wet Etchants						
Name	Target Material		Operating Temp		Etch Rate	
Acetone	Photoresist		20°C		Very High	
HCl:HNO_3:H_2O 1:3:80	Zinc Oxide		20°C		$\approx$ 50 nm/sec	

2.5 Device Performance

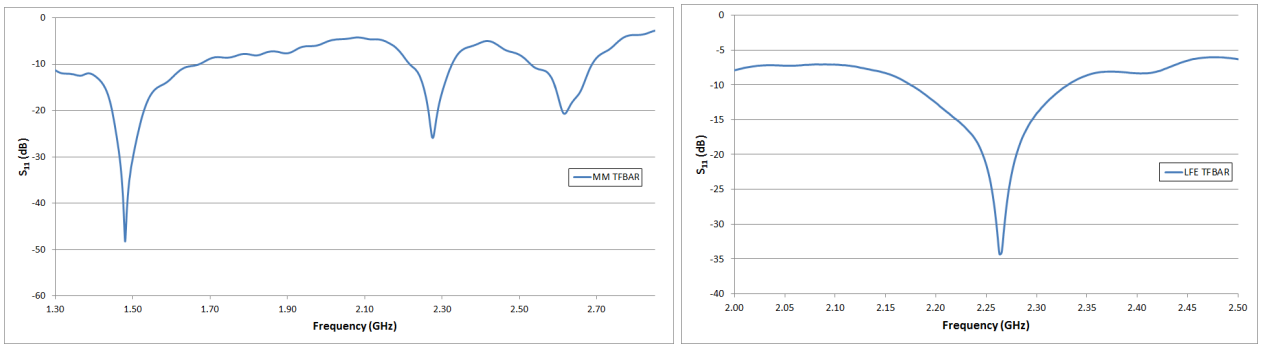

(a) (b)

Figure 9: S_{11} Parameters for (a) multi-mode and (b) LFE devices.

Table 3: Average resonant frequency and Q factors for both multi-mode and LFE devices.

	LFE	Multi-Mode		
Vibration Mode	TSM	TSM	Hybrid	TE
Resonant Frequency (GHz)	2.50	1.50	2.30	2.70
Q factor	330	260	200	45

Figure 33 shows the one-port scattering (S_{11}) parameters of both the multi-mode and LFE devices designed and fabricated by the author using the aforementioned protocol. Figure 33a shows all three of the modes of operation for the multi-mode devices (TE, TSM, and Hybrid). Figure 33b shows the TSM mode of the sandwich LFE device. Table 3 outlines the average device parameters (resonant frequency and Q factor) for both device types.

Figure 10 shows several scanning electron microscope images of the completely fabricated devices taking by Zeiss Ultra60 FE-SEM. Figure 10a shows a cross section view of the device stack with the supporting silicon wafer and Figure 10b shows a zoomed in view of the Bragg reflector and the top piezoelectric cavity of ZnO.

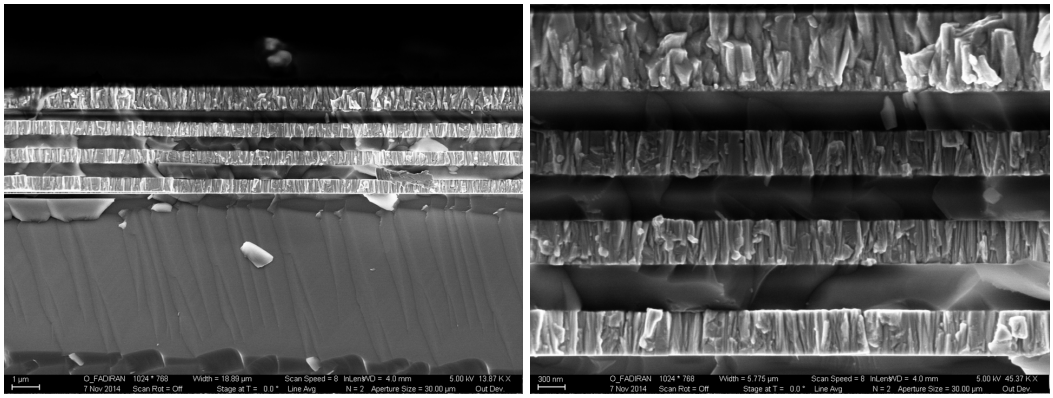

(a) (b)

Figure 10: SEM images of the (a) acoustic reflector on a silicon wafer and a (b) close cross section of the device layer stack.

2.6 Conclusion/Discussion

The design and fabrication of zinc oxide (ZnO) solidly mounted resonators (SMR) was described for the application of biomarker detection. Fundamental research findings were presented starting with the discovery of piezoelectricity. A short description was provided of several mathematical and electrical circuit models for simulating resonator performance. A theoretical derivation proved the existence of pure TE and TSM modes for device operation. Prior work was presented for the existence of a hybrid mode in the multi-mode devices and mechanical energy trapping is accomplished with the design of an acoustic reflector. Lastly, the fabrication protocol outlined in Section 2.4 was used for the development of each device array. For the remaining chapters (excluding Chapter 6), all data is based on the devices described in this section.

CHAPTER 3

RADIO FREQUENCY CHARACTERIZATION OF USB 3.0A CONNECTORS

3.1 Introduction

Modular systems with sensors operating in the radio frequency (RF) spectrum require electrical characterization to excite the governing phenomena (e.g. piezoelectricity) and extract any analytical information about the environment (e.g. biomarker detection). Therefore, the electrical connection between the characterization unit and the sensor module must be capable of sustaining these RF signals. Typically this is achieved with coax connectors, for instance, SubMiniature version A (SMA). RF connectors are usually single port, which can be limiting for biosensing applications as an array of devices characterized simultaneously increases the robustness of an analysis. Additionally, the targeted end-users for point-of-care systems would be medical staff (i.e. nurses, doctors, laboratory technicians) whom may be unfamiliar with currently available RF connectors.

Universal Serial Bus (USB) is a communication protocol first developed by the USB Implementers' Forum back in the 1990s. Each release version of this protocol includes the mechanical, electrical, and telecommunication requirements. The recently developed USB 3.0 provides nice electrical traces as compared to its predecessors and is rated for data rates of 5 Gbps [43]. Although USB ports are primarily for digital serial communication, the limiting factor for higher frequency operation is each electrical trace's rise and fall times. Therefore, these devices can potentially be utilized as an L/S-Band (0.5-4.0 GHz) RF communication bus.

In the following chapter, we examine the feasibility of utilizing USB 3.0 connectors as a radio frequency characterization bus. A three dimensional computer aided design (CAD) model has been developed and evaluated by finite element analysis (FEA) in order to extract the capacitance matrix between each port. These results are then compared to the

capacitance matrix derived from measured scattering parameter (S-parameter) data from a USB 3.0 test bench. Lastly, a comparison of the frequency response of a zinc oxide surface mount resonator (SMR) characterized both via a USB port and vector network analyzer (VNA) probe tips is demonstrated.

3.2 COMSOL CAD Simulation

Simulated USB 3.0 performance is calculated based on FEA results of the CAD model seen in Figure 11. The model was developed in SolidWorks® [44], a 3D CAD design platform, with dimensions based on the data sheets supplied for the ordered parts [45, 46]. FEA is performed by COMSOL Multiphysics® [47], a simulation platform that solves various boundary condition problems in tandem, especially for coupling phenomena such as piezoelectricity. The LiveLink for SolidWorks interface was utilized for transferring model domain definitions from SolidWorks into the COMSOL system framework.

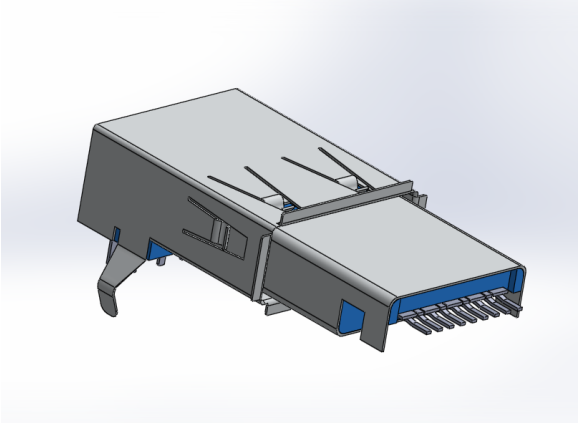

Figure 11: CAD model of USB plug and connector.

COMSOL's AC/DC module, electrostatic interface, utilizes the differential form of Maxwell's equations to determine charge distribution within a model. This interface provides a feature of calculating the capacitance matrix for multiport devices [48]. Each domain of the model has electrical properties applied based on the reported materials within the data sheets; property values are outlined in Table 4. All metal conponents of the USB

connector and plug (traces and shielding) are removed from the simulation using the difference Boolean operator as they are treated as perfect electrical conductors. Terminal port conditions are applied to the boundary of each electric trace in order to calculate the coupling capacitance values. The starting conditions, charge conservation and zero initial charge, are applied to all other regions; an example FEA setup is explained in detail in the reference [49]. The simulation is then executed iteratively with the stationary solver by switching the excitation ports to calculate all of the coupling factors for the capacitance matrix; additional simulation information is listed in Table 4.

Table 4: COMSOL Settings for material properties and mesh complexity.

Material Properties	
Material	Relative Permittivity (ϵ_r)
Air	1.0
LCP	3.5
Mesh Statistics	
Total Elements	1070911
Degrees of Freedom	1557560
Mesh Volume	47700.0 mm^3
Solution Time Per Port	1 min 17 sec

3.3 Simulation Results

3.3.1 Coupling Images

Figures 12 and 13 show several cross section images of the USB simulated data for port 3 (Figure 12) and port 7 (Figure 13). The color plot displays the electric potential distribution from the excitation port. The streamlines represent the electric field that illustrates how each port is coupled to the neighboring ports or to ground (the outer most shielding).

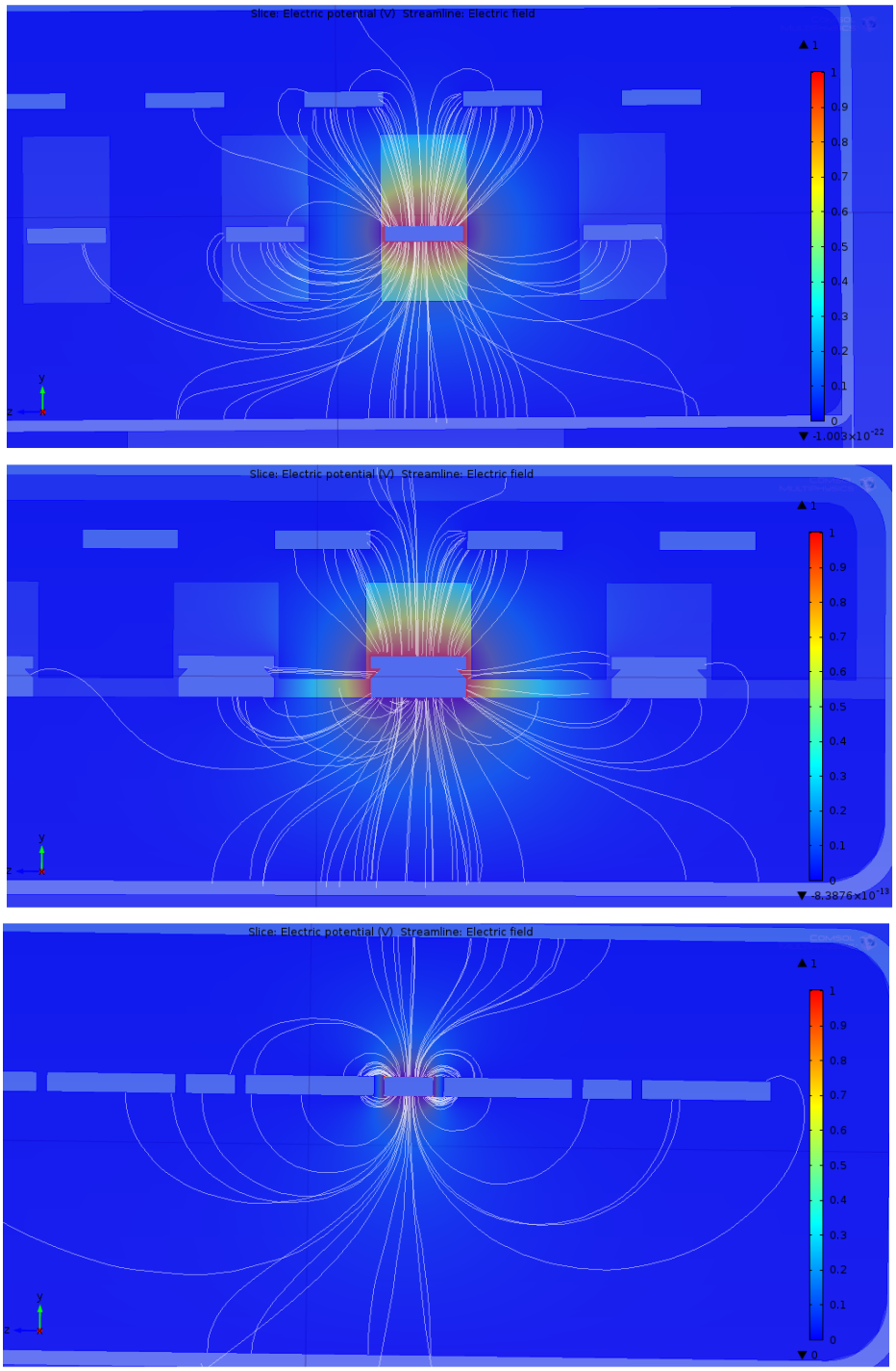

Figure 12: FEM cross section images for solutions excited by port 3. Images are extracted from the USB (a) connector, (b) contact pads, and (c) plug. Color plot represents the voltage distribution and the streamlines are an example of the electric field.

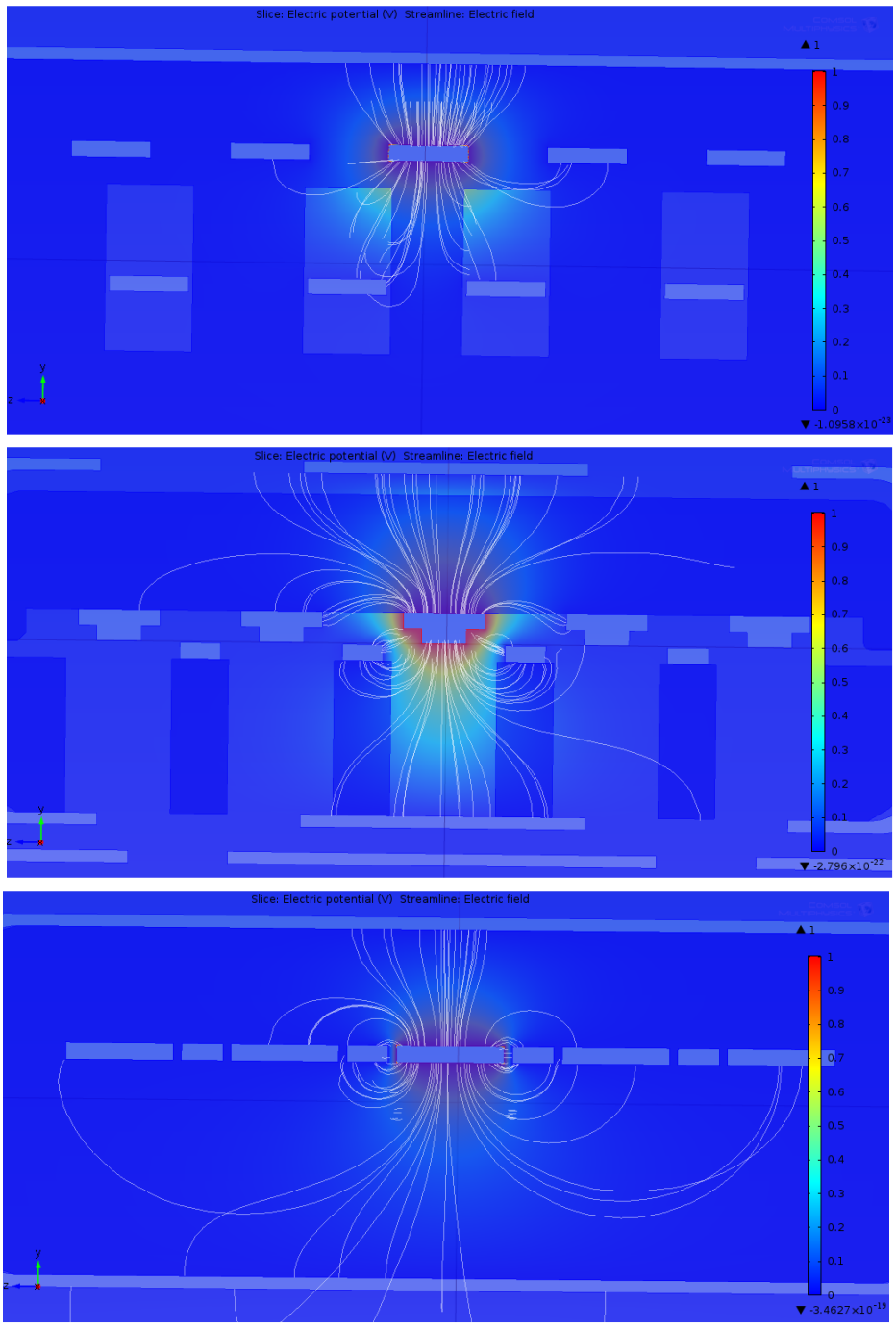

Figure 13: FEM cross section images for solutions excited by port 7. Images are extracted from the USB (a) connector, (b) contact pads, and (c) plug. Color plot represents the voltage distribution and the streamlines are an example of the electric field.

3.3.2 Simulated Capacitance Matrix

Table 5 is the complete capacitance matrix based on the COMSOL FEM simulated data. The resultant capacitance values are determined under static wave conditions. Therefore, high frequency effects, e.g., skin effect and fringe fields are not taken into account. In order to account for these factors that affect inter-port coupling factors, we now examine the experimental data.

Table 5: Coupling capacitance matrix values based on simulated FEM values.

	Excitation Port								
Sensing Port	Port 1	Port 2	Port 3	Port 4	Port 5	Port 6	Port 7	Port 8	Port 9
Port 1	1.52 pF	-82.5 fF	-5.47 fF	-1.23 fF	-0.80 fF	-1.53 fF	-8.10 fF	-0.51 pF	-0.61 pF
Port 2	-82.5 fF	1.53 pF	-0.12 pF	-5.47 fF	-1.96 fF	-10.2 fF	-0.54 pF	-0.55 pF	-13.9 fF
Port 3	-5.47 fF	-0.12 pF	1.53 pF	-82.6 fF	-13.9 fF	-0.55 pF	-0.54 pF	-10.2 fF	-1.96 fF
Port 4	-1.23 fF	-5.47 fF	-82.6 fF	1.52 pF	-0.62 pF	-0.50 pF	-8.11 fF	-1.53 fF	-0.80 fF
Port 5	-0.80 fF	-1.96 fF	-13.9 fF	-0.62 pF	1.66 pF	-0.13 pF	-5.57 fF	-1.64 fF	-0.96 fF
Port 6	-1.53 fF	-10.2 fF	-0.55 pF	-0.50 pF	-0.13 pF	1.95 pF	-0.13 pF	-4.89 fF	-1.65 fF
Port 7	-8.10 fF	-0.54 pF	-0.54 pF	-8.11 fF	-5.57 fF	-0.13 pF	1.97 pF	-0.13 pF	-5.58 fF
Port 8	-0.51 pF	-0.55 pF	-10.2 fF	-1.53 fF	-1.64 fF	-4.89 fF	-0.13 pF	1.95 pF	-0.13 pF
Port 9	-0.61 pF	-13.9 fF	-1.96 fF	-0.80 fF	-0.96 fF	-1.65 fF	-5.58 fF	-0.13 pF	1.66 pF

3.4 Test Bench Setup

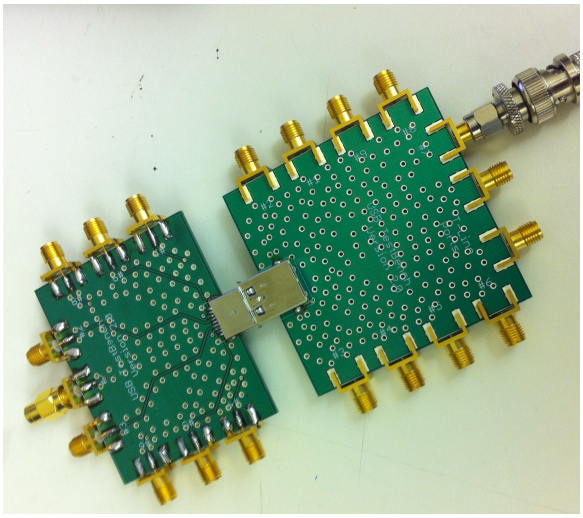

Figure 14: PCB test bench for the USB S-Parameter measurements.

Figure 14 shows an image of the printed circuit board (PCB) test bench developed to

extract the S-parameters via SMA ports. The design is based off the recommended test bench setup provided by the USB developer's white paper [43]. To minimize coupling and interferences cause by the PCB, basic design considerations such as trace width sizing, spacing and via fences were implemented based on recommendations from previous work [50]. All S-parameter measurements were conducted by a HP8753 Virtual Network Analyzer. Time-domain reflectometer (TDR) measurements were obtained to determine the source of any reflections within the connector for each port. All TDR measurements were conducted by a Mohr CT100®.

Capacitance matrix data was calculated utilizing a process previously developed by Young and Sparkman [51]. First, this protocol requires open termination (with match load termination for all other ports) and measuring the S_{11} parameters of each port; these measurements determine the main diagonal values of the capacitance matrix (**C**) and conductance matrix (**G**) from equation (19). Subsequently, S_{12} parameters are measured for each port combination with open terminations (and match load termination for all other ports) to calculate the remaining matrix values from equation (20).

$$(\mathbf{G} + j\omega\mathbf{C})^{-1}_{mm} = Z_o \frac{1 + S_{mm}}{1 - S_{mm}} \tag{19}$$

$$(\mathbf{G} + j\omega\mathbf{C})^{-1}_{mn} = \left[Z_o + (\mathbf{G} + j\omega\mathbf{C})^{-1}_{mm}\right] \frac{S_{mn}}{1 - S_{nn}} \tag{20}$$

The variables m and n are port numbers (port #1-9) and ω is the angular frequency of the excitation signal ($2\pi f$). For determining the final capacitance matrix, capacitance values are calculated based on S-parameter values sampled every 175 MHz within the target range (0.5-4.0 GHz).

3.5 Test Bench Results

3.5.1 Connector Reflections

In order to characterize the properties of connection under test (USB 3.0), parasitic effects of the PCB test bench must be minimized. As stated above, the board was designed using via fences and proper trace widths in order to match the impedance within the target frequency range (0.5 - 4.0 GHz).

Figure 15 shows the TDR measurements for both port 3 (a) and port 7 (b), demonstrating the reflection coefficient verses distance from the source signal. These two ports are selected as examples because of they are close to the interior of the connector and should have the largest coupling effects from all other ports. Each region denotes a different component in which the signal pulse has traveled through. First the instrument cord, then the first PCB, the USB connector, the second PCB and finally the open termination. The average measured impedance values for all USB ports are listed in Table 6. From Figure 15, the largest impedance mismatch is within the USB connector and implies that it is the source of the majority of the signal reflections prior to the final open termination. This observation is essential as the S-parameter data in the following sections only denotes the total amount of reflected energy back to the source with no capability of determine the source of the reflected energy.

(a)

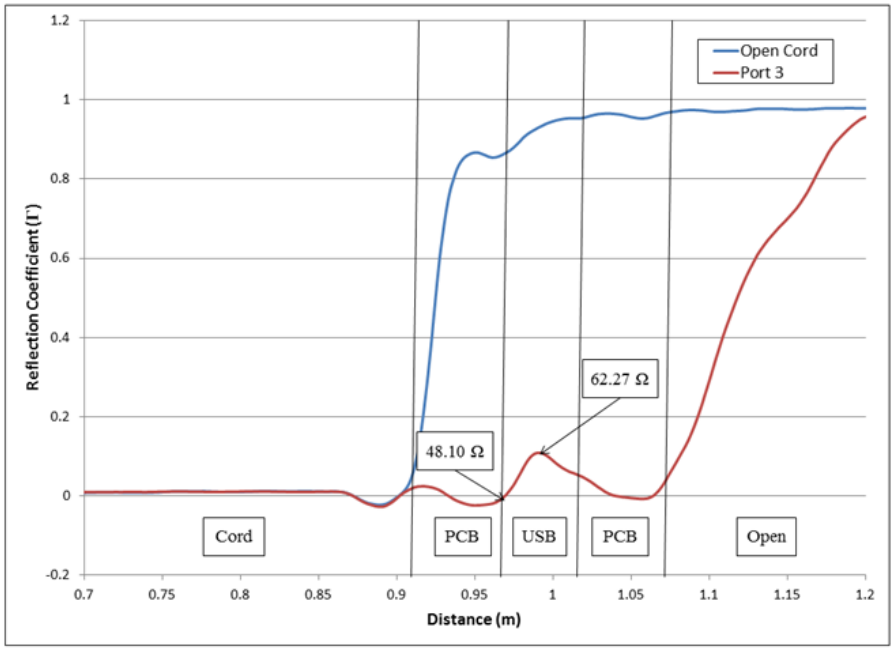

(b)

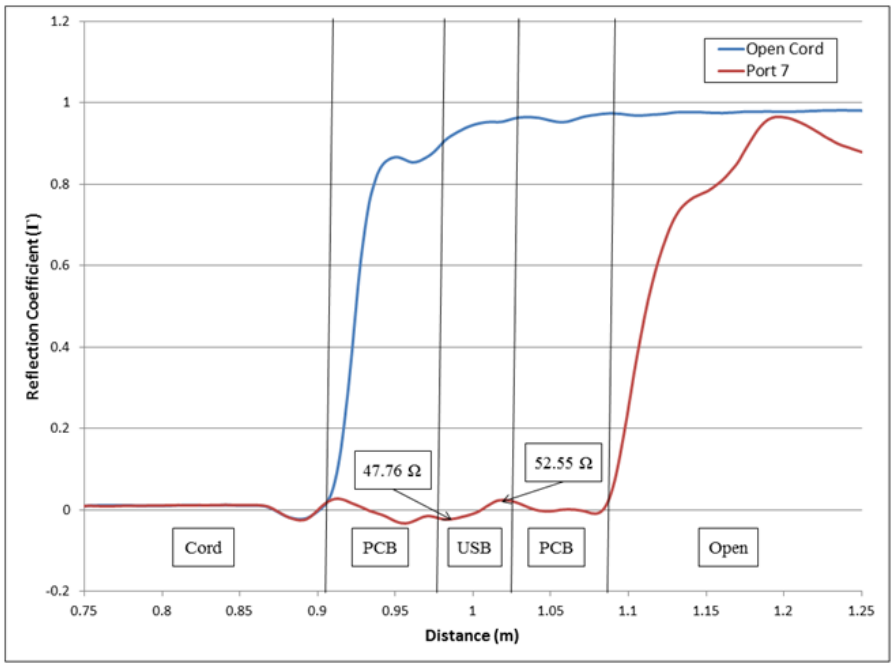

Figure 15: TDR measurements for (a) port 3 and (b) port 7 of the PCB test bench.

Table 6: Impedance ranges for each connector port.

Ports 1-4	61.91 ± 0.35 Ω, 47.55 ± 0.60 Ω
Ports 5-9	53.50 ± 0.95 Ω, 47.60 ± 0.57 Ω

3.5.2 Wideband Characterization

Proper device characterization requires signal integrity through the USB 3.0 connector. This means that the signal will interact with the impedance mismatch of the connector twice (during the round trip). We can examine the amount of energy delivered and received via the characterization unit by changing the electrical path termination and compare the results.

Figures 16 and 17 shows two separate S_{11} Parameter measurements with various termination conditions on both port 3 (Fig. 16) and port 7 (Fig. 17). For the matched load plot, the majority of the reflected energy is caused by the connector impedance mismatch. As for the open load plot, the received energy to be a combination of the connector impedance mismatch and the energy reflected off the termination. This scenario is similar to the characterization of a device, in which the returned signal contains the analytical information of the device, for instance, the resonant frequency. All other ports were terminated by a matched load to remove the coupling effects from these measurements.

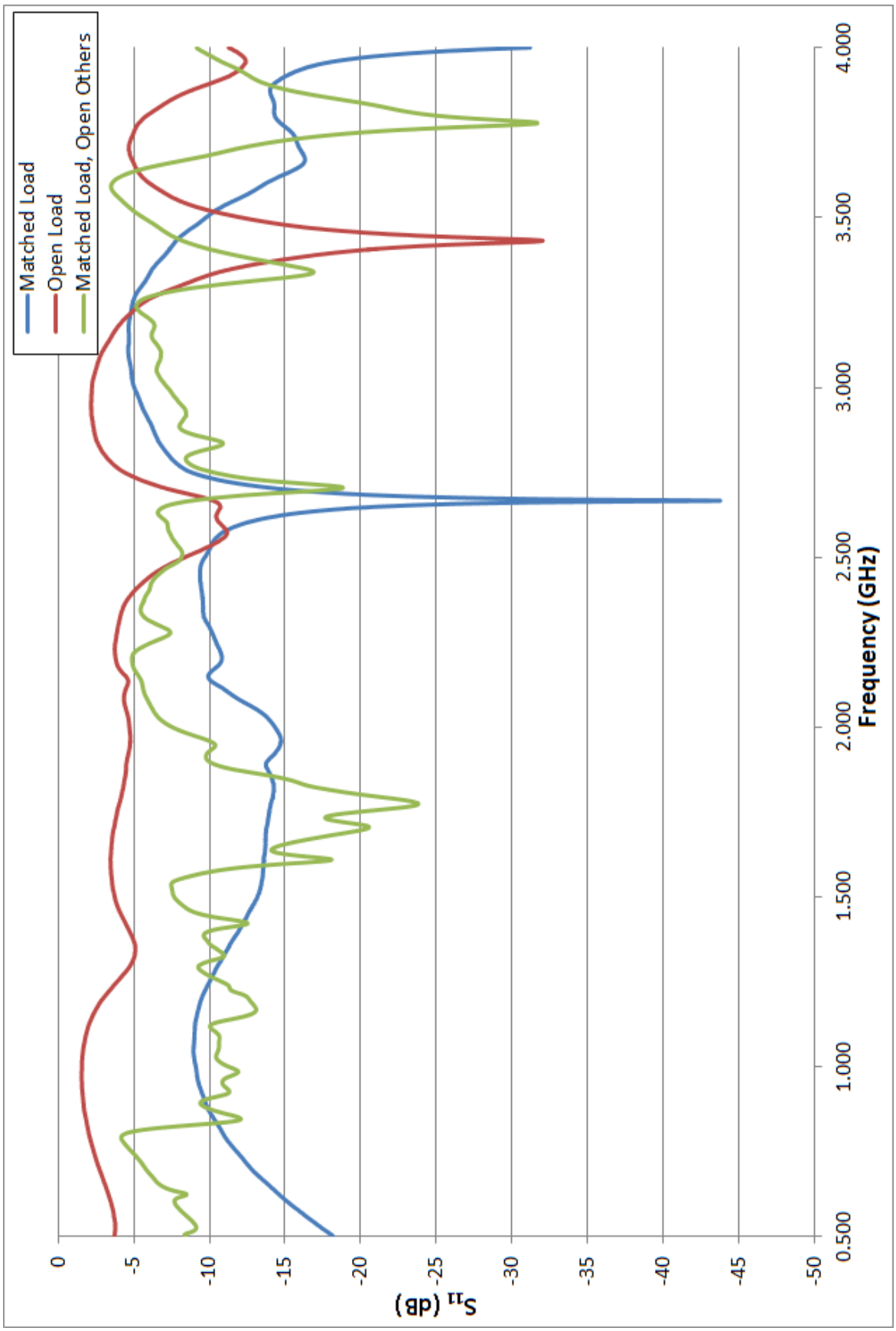

Figure 16: S_{11} measurements with varying termination conditions (open and matched load) for port 3.

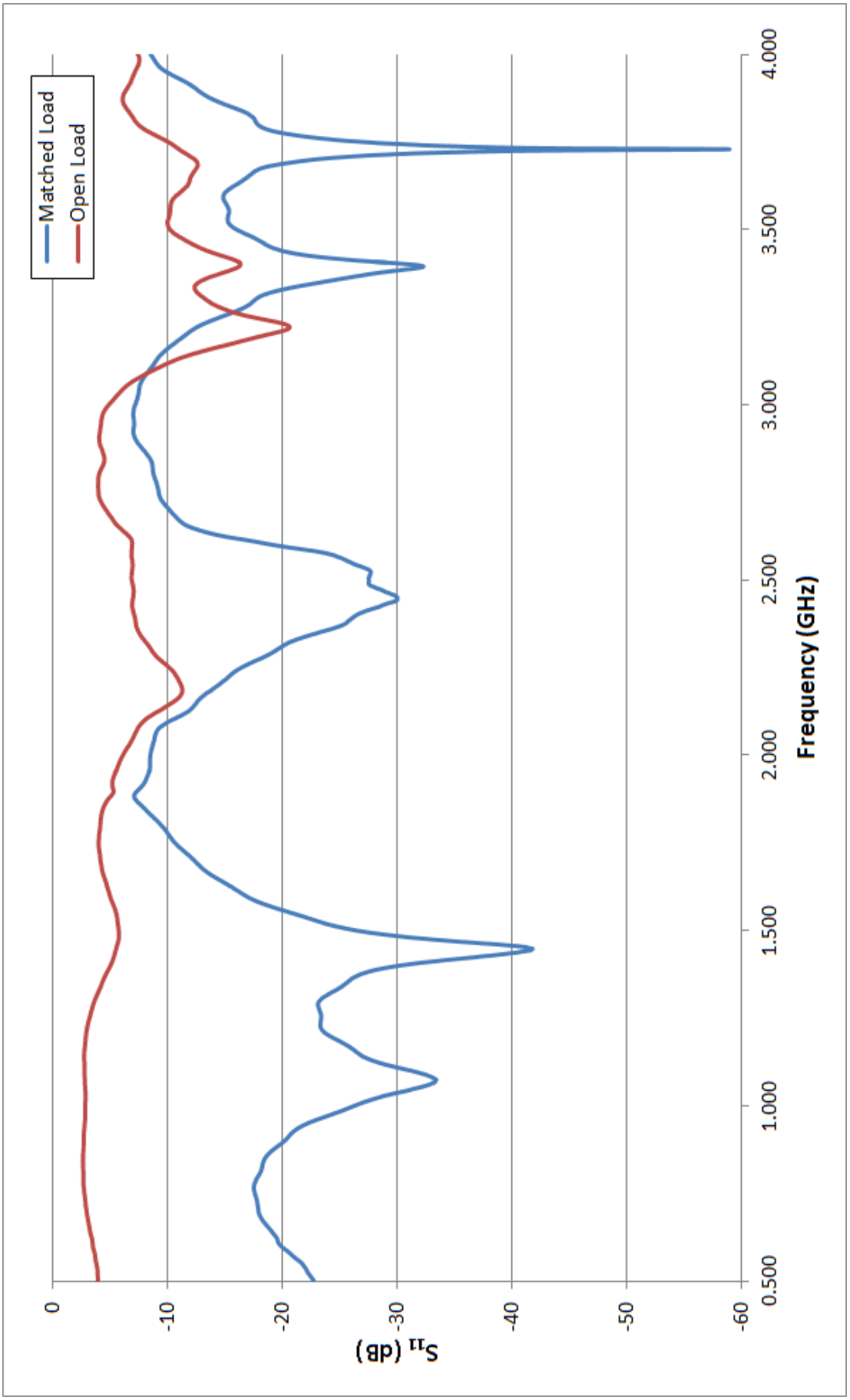

Figure 17: S_{11} measurements with varying termination conditions (open and matched load) for port 7.

Using the two different plots, we can define regions in which the USB connector is capable of properly characterizing the device under test. For regions in which the open termination energy level exceeds the match load energy level, for example, in Figure 17 from 0.5 GHz to 1.5 GHz; implying that the majority of the reflected energy is caused by the termination (or the device under test). Any other region in which the two plots either reach similar energy levels or vice versa where the matched load plot's energy level is higher designates regions in which the USB connector's parasitic effects drastically decrease the signal to noise ratio (SNR). Table 7 outlines all of the acceptable regions of operation for each USB port in accordance with the above assumption with a signal separation greater than 3 dB.

Lastly, the "matched load, open others" plot (Fig. 16) is an example of the effects of open termination of all other ports with match load termination for port 3. The effects of the open termination increase the reflected energy from the USB connector because of the coupling effects of the other ports; similar to the effects of a directional coupler that is not properly terminated. This drastically decreases the SNR for each individual port; therefore it is essential that all other ports are properly terminated for high frequency operation of the USB Connector.

Table 7: Regions of acceptable operation for USB 3.0 connector per port, based on comparison of S_{11} parameters for both open and match load termination with greater than 3 dB separation.

USB Port #	Acceptable Operation Ranges (GHz)
1	0.500-2.528, 3.055-3.307, 3.342-3.958
2	0.500-2.423, 2.615-2.968, 3.532-4.000
3	0.500-2.451, 2.613-2.978, 3.545-4.000
4	0.500-2.539, 3.092-3.983
5	0.500-2.322, 2.381-2.661, 2.692-3.648
6	0.500-2.005, 2.198-2.828, 3.280-3.974
7	0.500-1.861, 2.195-2.913, 3.285-3.943
8	0.500-1.865, 2.333-2.915, 3.280-4.000
9	0.500-2.217, 2.950-3.613

3.5.3 Measured Capacitance Matrix

Table 8 is the complete measured capacitance matrix over the target frequency range. The measured values were calculated based on the S-parameter data measured via a network analyzer and Equations (19) and (20). 21 discrete data points were evenly sampled over the target frequency range (0.5 GHz - 4.0 GHz). For each S_{11} measurement, the data is smoothed with a local first order regression algorithm to minimize the effects of parasitic resonances from the capacitance calculations. Each selected frequency sample is converted to a capacitance matrix and the mean values of all frequency values are presented in Table 8.

Table 8: Coupling capacitance matrix values based on measured USB test bench values converted via Equations (19) and (20).

	Excitation Port								
Sensing Port	Port 1	Port 2	Port 3	Port 4	Port 5	Port 6	Port 7	Port 8	Port 9
Port 1	1.44 pF	-0.35 pF	-0.23 pF	-0.28 pF	-0.29 pF	-0.36 pF	-0.22 pF	-0.46 pF	-0.69 pF
Port 2	-0.41 pF	1.15 pF	-0.37 pF	-0.22 pF	-0.30 pF	-0.54 pF	-0.40 pF	-0.41 pF	-0.43 pF
Port 3	-0.24 pF	-0.40 pF	1.18 pF	-0.36 pF	-0.34 pF	-0.37 pF	-0.39 pF	-0.48 pF	-0.27 pF
Port 4	-0.28 pF	-0.28 pF	-0.40 pF	1.38 pF	-0.80 pF	-0.49 pF	-0.23 pF	-0.41 pF	-0.30 pF
Port 5	-0.35 pF	-0.38 pF	-0.51 pF	-0.76 pF	1.23 pF	-0.62 pF	-0.27 pF	-0.48 pF	-0.39 pF
Port 6	-0.42 pF	-0.53 pF	-0.52 pF	-0.60 pF	-0.58 pF	1.06 pF	-0.44 pF	-0.33 pF	-0.42 pF
Port 7	-0.40 pF	-0.59 pF	-0.53 pF	-0.31 pF	-0.32 pF	-0.53 pF	1.19 pF	-0.50 pF	-0.43 pF
Port 8	-0.58 pF	-0.48 pF	-0.51 pF	-0.45 pF	-0.47 pF	-0.36 pF	-0.43 pF	0.96 pF	-0.58 pF
Port 9	-0.70 pF	-0.40 pF	-0.32 pF	-0.33 pF	-0.37 pF	-0.51 pF	-0.26 pF	-0.56 pF	1.39 pF

3.6 MEMS Characterization

Figure 18 shows an example device characterization. The plot is a frequency response of a LFE ZnO SMR devices wire bonded and mounted in a ceramic pin grid array (CPGA) package. The device-under-test (DUT) is characterized via a vector network analyzer (VNA) first with probe tips and second, through the complete USB test bench via coax cable connectors. The reason for the difference in the Q factor of the resonant frequencies of the device is attributed to the quality of the connections to the DUT as wire bonding creates an alloy with the device. This plot demonstrates the ability to properly characterize high frequency MEMs devices through the USB connector with some insertions losses.

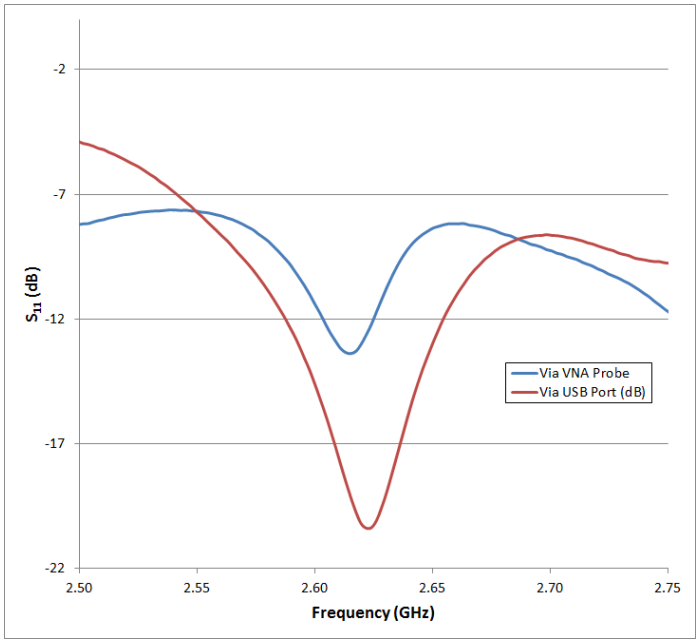

Figure 18: Example S_{11} parameter characterization of Zinc Oxide (ZnO) Solidly mounted Resonator (SMR) thickness shear mode (TSM) measured with VNA probe tip and through the USB test bench.

3.7 Conclusion/Discussion

USB 3.0A connectors were examined as a potential radio frequency characterization bus. Both a simulated and experimental approach was performed. For the simulated data, a 3D CAD model was developed and evaluated by finite element analysis (FEA) in order to

extract the capacitance matrix between each port. For the experimental data, a USB 3.0 test bench was designed and characterized by a time-domain reflectometer and a vector network analyzer. The scattering parameter (S-parameter) data is then converted to the capacitance matrix. Lastly, the frequency response of a zinc oxide surface mount resonator (SMR) was obtained via the USB test bench and VNA probe tips to demonstrate the ability of the USB connector to provide proper characterization of a device under test.

CHAPTER 4

DESIGN AND OPTIMIZATION OF USB FLUIDICS MODULE

Patient screening serves as a proactive approach to disease diagnostics for patients who have yet to exhibit symptoms. These protocols can provide early detection of malignant diseases and increase the effectiveness of treatment measures. A variety of methods have been developed for screening patient samples, e.g., Enzyme-Linked Immunosorbent Assay (ELISA) and Mass Spectrometry [52].

ELISA is a protocol performed in 96-well plates where immobilized proteins on the bottom of each well and subsequently bonded to a combination of serum and/or synthetic antibodies. These antibodies can be tagged with enzymes to react with products in the solution creating a color change in the solution to determine concentration levels. However, since this analysis is based on the optical density of the enzymatic product for each well; results have poor resolution and detection limits [53].

Mass Spectrometry is another method for screening patient samples which utilizes an ionization source to charge sample particles for extracting mass-to-charge ratios. Although these systems are capable of low detection limits and wide measurement ranges, their high price and complex results hinders their usage as a distributed screening technology [54].

Therefore, there is a focus to develop low-cost, simple, and quantitative systems also known as point-of-care (POC) systems. POC systems require inexpensive and potentially disposable module design for ease of use. Specific design considerations must be accounted for depending on the desired application and the type of sensor devices utilized.

The following chapter details the design and optimization of a radio frequency (RF) Universal Serial Bus (USB) module for real-time characterization of biological sensors. An initial fluidics packaging design is first developed with computer aided design (CAD) software and an acceptable design space was determined. Potential design solutions are

then optimized utilizing the differential evolution (DE) algorithm. Subsequently, we utilized the USB 3.0 as a RF signal port in order to extract scattering parameter (S-Parameter) data for an example device with varying environmental conditions.

4.1 Differential Evolution

Differential evolution (DE) is a biologically inspired algorithm designed to be an effective and practical method for solving a wide variety of optimization problems. This variation on evolutionary algorithms and was first introduced by Storn and Price [55]. It has been proven to be effective when functions are non-differentiable and non-linear and have good convergence properties [55]. Additionally, this algorithm is effective in cases where cost functions are computationally intensive because it is highly parallelizable.

DE control variables are defined at the beginning of the problem to describe various aspects of how the algorithm will behave. Figure 19 shows the primary code segment for this optimization scheme. F is the mutation scale factor which controls the size of the differential vector during the mutation step. Values range from 0 to 1 however for this study, we set this parameter to 0.5 in order to minimize step sizes and prevent premature convergence [56]. Cr is the crossover probability and also has a value range between 0 and 1 [56]. This parameter determines the probably of an evolved solution to inherit values from its parent or mutated vectors. For this study we set Cr to 1, removing the crossover process because the algorithm tends to converge more quickly [55]. NP is the number of candidate solutions making up the population. This values should be set between 5 to 10 times the number of objective parameters (values being optimized) to allow a sufficient representation of the parameter design space [55].

A DE optimization begins by initializing the population of size NP with random vectors with each objective parameter within the allowed range specified by the user. Each individual member is then evaluated according to the objective cost functions to determine all preliminary design cost values. Subsequently, mutant vectors are created according to

```
//First generation initialized with randomly scattered members
P0 = generate_poulation();
//Determine cost values for each member
C = find_cost( P0 );

//Repeat until last generation Gmax
while(G <= Gmax)
{
        gen_best = P0[min_cost( C )];          //Find member with the smallest cost
        for(int i = 0, i < NP , i++)
        {
                //Create evolved member based on selected strategy
                trial = P0[i];
                apply_DE( trial );
                //Determine new member cost value
                testcost = find_cost( trial );

                //Replace parent vector with trial if the cost less
                if(testcost < C[i])
                {
                        P1[i] = trial;
                        C[i] = testcost;
                }
                else
                P1[i] = P0[i];
        }
G++; //move to next generation
P0 = P1; //copy created generation to current generation
}
```

Figure 19: Example pseudocode for the differential algorithm.

the selected algorithm strategy, for example, Best2Bin shown in Figure 20. Each mutant vector is evaluated according to the objective cost functions and if its cost value is less than the parent's cost then it replaces it in the next generation; if not the parent moves onto the next generation. After a new generation is completed, the mutation and selection steps are repeated until a stopping criterion is reached, e.g., a maximum number of generations or reaching a desired objective function value [55]. For this study, optimization was stopped after a specified number of generations.

The originators of DE, Storn and Price, have not filed for intellectual property protection of this algorithm, which has led to end-user development of multiple freeware implementations of DE [57]. This allows users to customize the code for their applications. For instance, when a design is limited by multiple restrictions, DE can be set up to find the combined optimal solution rather than individually optimize separate objectives which is known as multi-objective optimization [58].

For this study, we utilize SolidWorks® [59], a computer aided design (CAD) software to create an initial design for a fluidics flow chamber seen in Figure 21. The CAD model

```
//Best2Bin strategy
public void apply_DE ( trial )
{
        //go through every dimension
        for(int i = 0, i < dim, i++)
        {
                //Alter dimension only if the random number is less than Cr
                if( ((randNum() % 100) / 100) < Cr)
                {
                //Define new dimension for the best member and randomly
                //selected members of the population weighted by F
                trial[i] = gen_best[i] + (F * (P0[rand()][i] + P0[rand()][i] - P0[rand()][i] - P0[rand()][i]));
                }
        }
}
```

Figure 20: Example pseudocode for the Best2Bin parameter selection strategy.

is parameterized and an acceptable value range is established for each objective parameter prior to optimization (Table 9). SolidWorks provides finite element modeling (FEM) structural and flow dynamics add-ins which is further explained in references [60]. We utilize these systems to set up and extract objective cost function values for each design.

4.2 Optimization Setup and Parameters

Figure 21 shows an example of the fluidics chamber to be optimized. We defined three types of objective parameters for the design optimization, the inlet and outlet shaft inner radius and the depth of the chamber (Fig. 21a-c). Each parameter has a predetermined range of acceptable values outlined in Table 9.

Table 9: Range of acceptable values for fluidics chamber design.

Design Space			
	Dimension Name	Min Value (mm)	Max Value (mm)
Fig. 21a	D1@Sketch23	0.6	1.73
Fig. 21b	D2@Sketch23	0.6	1.73
Fig. 21c	D1@Cut-Extrude1	0.2	2.2

The goal of this chamber design is to optimize the fluid dynamics of the chamber to minimize turbulent flow. Turbulent flow features can alter the sensors response to molecule concentration and result in incorrect measurements [61]. The Reynolds number [62] serves as a metric to denote fluidic flow patterns for various situations. The lower the value the

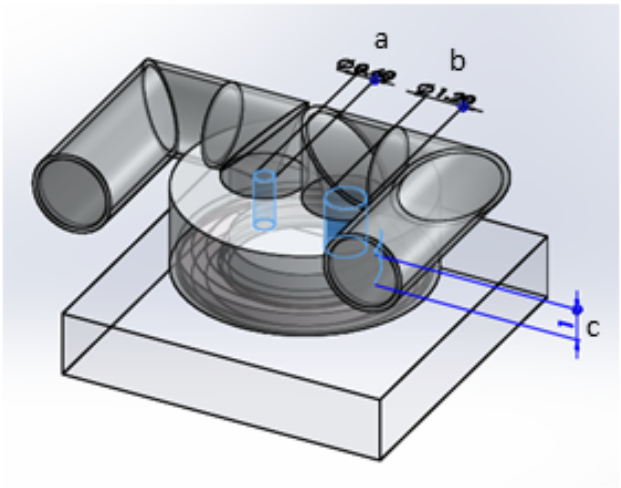

Figure 21: Variable dimensions for the fluidics chamber design.

more laminar the flow, the higher the value, more turbulent properties are present.

For this study, we look to optimize the flow properties right above the bottom surface of the chamber, where any mounted devices would be located. John Matsson [63] developed a protocol for determining the Reynolds number for a surface based on the calculated velocity and stress values from a SolidWorks FEA model. Based on this protocol, we have developed a simulation to determine the Reynolds number over a two dimensional surface as seen in Figure 22. The normal frictional force and in-plane velocity magnitude are calculated at each point. Subsequently, the Reynolds number is calculated (Equ. 21) for each of the selected flow paths (Fig. 22a-e) and then averaged to determine the complete Reynolds number for that design (Equ. 22).

$$Re_{xyi} = \frac{v_f \times d_{xy}}{\nu} \tag{21}$$

$$Re_{xy} = \frac{\sum_i Re_{xyi}}{5}, \quad i = [a, b, \ldots, e] \tag{22}$$

v_f is the velocity of the fluid, d_{xy} is the distance from the inlet in the xy-plane (parallel to the surface), and ν is the kinematic viscosity of water ($1.516 \times 10^{-5}\ m^2/s$), and Re_{xyi} corresponds to the calculated Reynolds number for each pathway (Fig. 22a-e).

Finite element modeling is performed on each design according to the setup explained

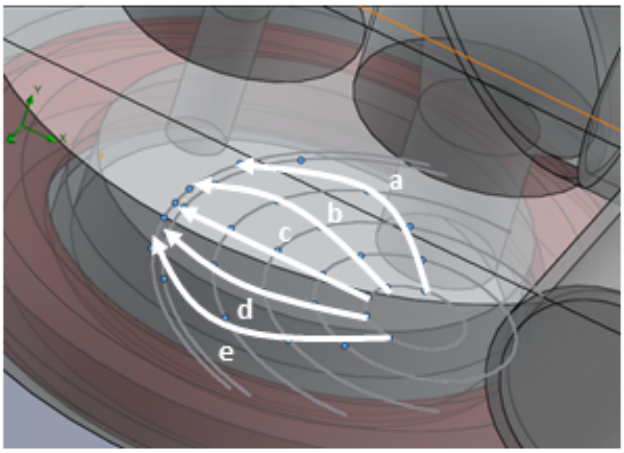

Figure 22: Flow paths in which the Reynolds number is calculated for each design.

previously. Four optimization processes were performed and the differential evolution parameters are outlined in Table 10. Mesh failures are FEA models that failed to converge on a solution for various reasons, for instance, minimal computer resources or overnight issues as each optimization took over three days to complete. These designs where assigned a high cost value and excluded from the optimization.

Table 10: Differentiation evolution parameters for each optimization.

Differential Evolution Parameters						
	Strategy	Population	# of Gen	Cr	F	Mesh Failures
Optimization #1	Best2Bin	23	50	1.0	0.5	431
Optimization #2	Rand2Bin	30	40	1.0	0.5	197
Optimization #3	Best2Bin	23	50	1.0	0.5	323
Optimization #4	Rand2Bin	30	40	1.0	0.5	180

4.3 Optimization Results

Figure 23 shows the results of the optimization #1, with each object variables normalized to their respective ranges outlined in Table 9. The total design cost value is determined based on the total Reynolds number of each design (eq. 22). Although this optimization minimizes the objective cost of our design based on minimizing the Reynolds number, all of the objective parameters tend to migrate to their minimum allowed values. These results support the fact that microfluidics platform maintain high levels of laminar flow [61]. However, this is not an acceptable solution for the design space initially selected.

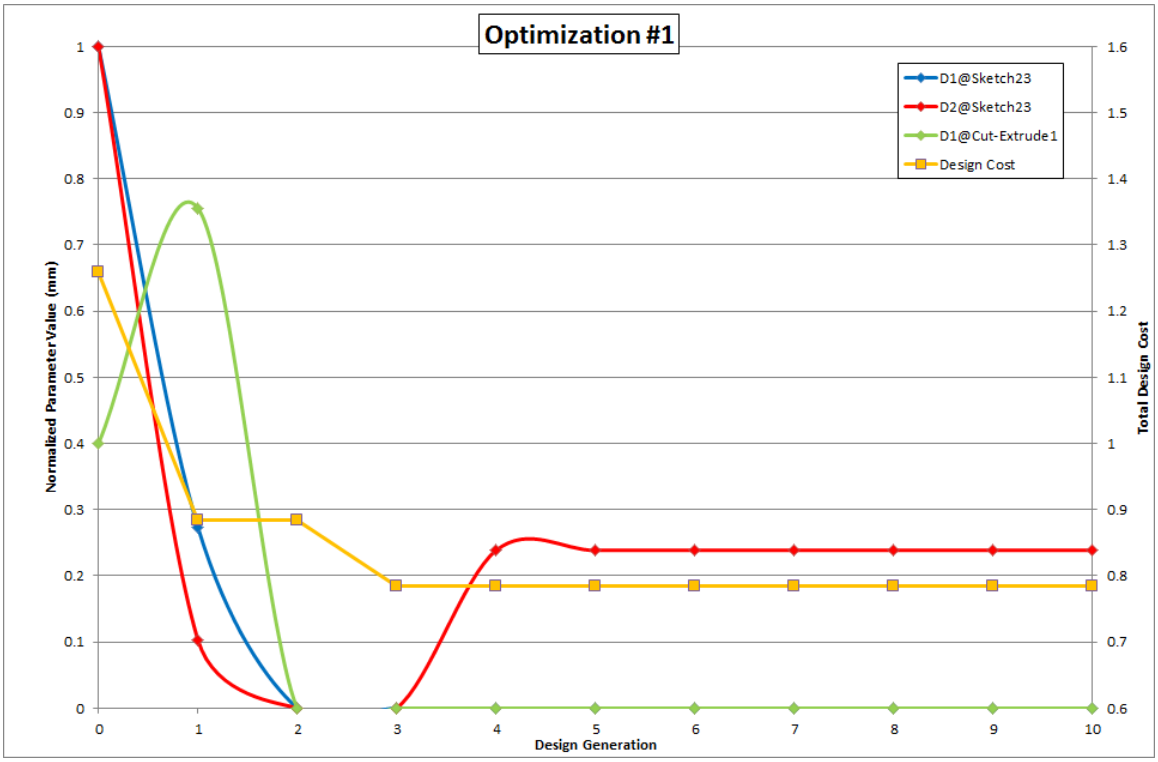

Figure 23: DE Parameters and total design cost for each generation of the optimization.

Table 11: Final results for each design parameter.

Optimized Design			
	D1@Sketch23	D2@Sketch23	D1@Cut-Extrude1
Initial Design	1.73 mm	1.73 mm	1.0 mm
Optimization #1	0.6 mm	0.84 mm	0.2 mm
Optimization #2	0.6 mm	0.6 mm	0.2 mm

In order to avoid this convergence issue, we again initialize the DE optimization scheme utilizing a multi-objective optimization approach. In addition to minimizing the Reynolds number for laminar flow, we will also minimize the volume of the material to reduce cost associated with fabrication of the design. As the previous results show the tendency for the parameters to minimize based on Reynolds number minimization, the opposite is true for reducing the volume of the design, as the maximum object variables means less material to produce each individual part. The DE algorithm will serve the purpose of finding the most optimal solution to these conflicting objective cost functions. Figure 24 shows the normalized results of optimization #3 and Table 12 shows the final parameter values after each optimization was performed.

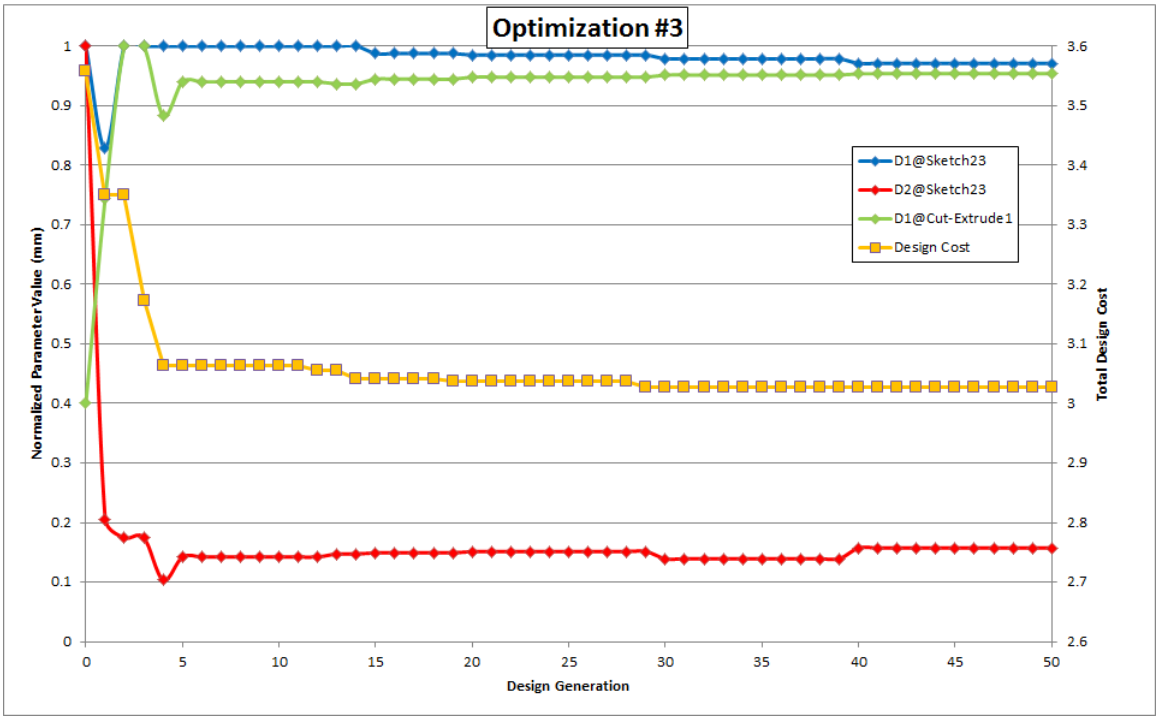

Figure 24: DE Parameters and total design cost for each generation of the optimization.

Table 12: Final results for each design parameter.

Optimized Design			
	D1@Sketch23	D2@Sketch23	D1@Cut-Extrude1
Initial Design	1.73 mm	1.73 mm	1.0 mm
Optimization #3	1.7 mm	0.78 mm	2.11 mm
Optimization #4	1.73 mm	0.85 mm	2.08 mm

Figure 25 show the flow trajectory for final chamber design. The color plot represents the particle velocity of the aqueous solution flowing through the design. The solution enters from the right and exits on the left. In actual operation, the flow rate would be controlled by a motor (e.g. a syringe pump).

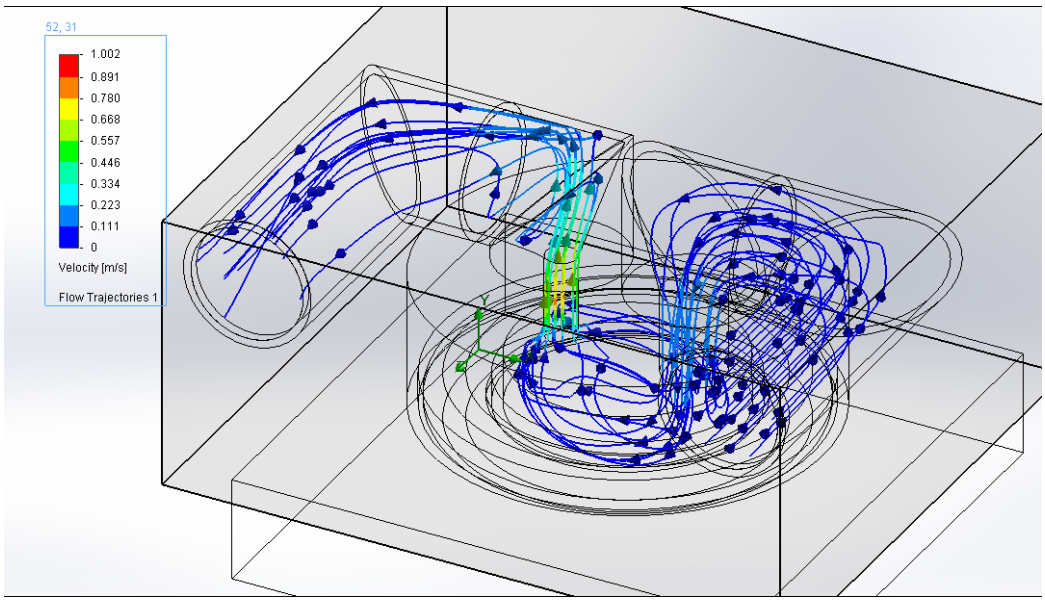

Figure 25: FEM simulated flow trajectory for the final optimized design.

4.4 Device Characterization Example

The final chamber design was set based on the values in Table 12. The chamber was incorporated into a larger module CAD model and fabricated via additive manufacturing or 3D printing. Each part was produce by an Objet Eden 250 [64] system which utilizes photoactive resin for model construction with water soluble support material. Figure 26 shows the final housing part that was produced.

In Chapter 3, we examine the use of a USB 3.0 port as a radio frequency communication bus [65]. We look to test the performance of this module with a printed circuit board (PCB) designed test bench with ceramic pin grid array (CPGA) packaging from NTK Technologies [66]. The width and spacing of PCB traces and via fences are designed according to recommendation from previous work [50] (Fig. 26). Previously designed zinc oxide (ZnO) surface mounted resonators (SMR) [4] are fabricated on a silicon wafer, diced, soldered and wire bonded to the CPGA packaging for electrical characterization via a network analyzer.

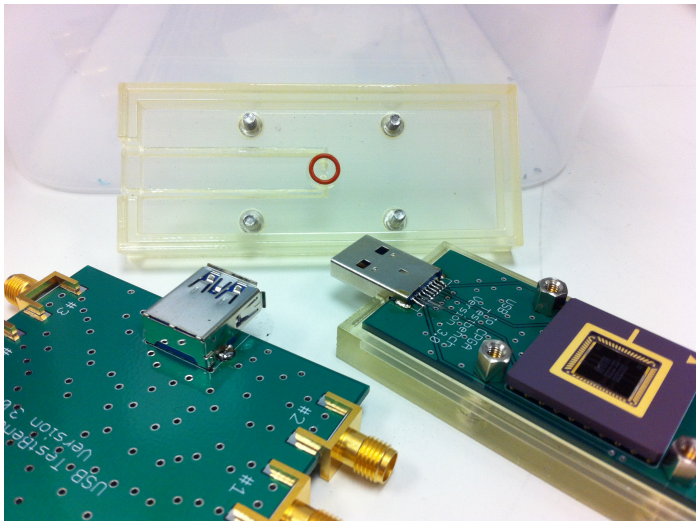

Figure 26: USB module with part, board, CPGA, and die.

Figure 27 shows the characterization of the thickness shear mode (TSM) from a ZnO SMR with various chemicals flown over the sensor. ZnO SMR are gravimetric sensors that can detect changes not only in mass but viscosity and other properties of a sample loaded on the surface of the device [4]. Figure 27a is the sensor's response to air and Figure 27b

is the response to DI water. Figure 27c,d are the sensor's response to other types of buffer solutions typically used in applications such as medical patient sample dilution.

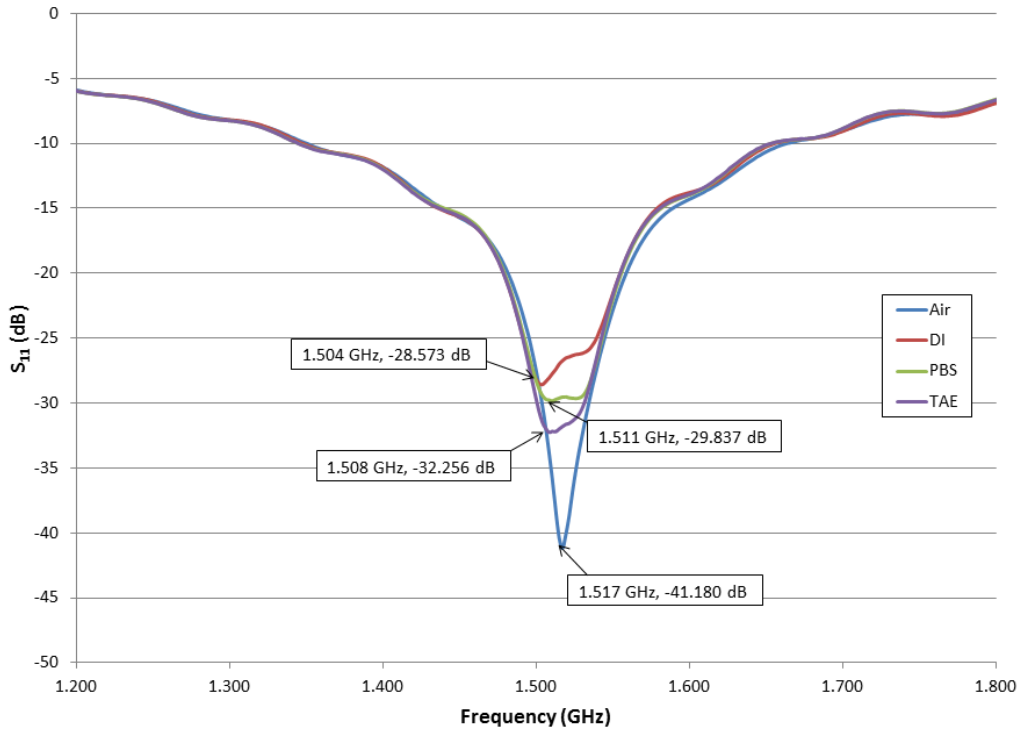

Figure 27: Example S_{11} parameter characterization of Zinc Oxide (ZnO) solidly mounted resonator (SMR) thickness shear mode (TSM) measured with mass loaded with various liquids (DI water, PBS, and TAE buffers) and air.

4.5 Conclusion/Discussion

A design for a fluidics USB module was optimized with the differential evolution algorithm. The design space was determined by specifying a range of acceptable values for each objective parameter. Random initial designs were subsequently evaluated based on objective cost functions such as the design's Reynolds number and material volume. Each design solution is then iteratively evolved based on the optimization algorithm's control variables and selection strategy. At the end of the optimization, the solution with the lowest design cost was selected and fabrication via additive manufacturing and then used to characterize a microelectromechanical system (MEM) device under different environmental conditions.

This optimization algorithm can be applied to different types of fluidics designs in order to find the optimal solution for a desired application and technology.

CHAPTER 5

LIQUID PHASE VALIDATION OF ZINC OXIDE SURFACE MOUNT RESONATORS

5.1 Introduction

The objective of the following chapter is to demonstrate the ability of the complete module system (wafer die, USB circuit board and fluidics packaging) to operate as a biosensing platform. First, a description of the functionalization protocol is provided. Antibodies specific to fluorescein isothiocyanate (FITC) are immobilized and subsequently exposed to the antigen. FITC serves as the target antigen for this chapter because of its fluorescence properties allowing for the use of imaging to verify the binding event. Next with the same antibody-antigen interaction, several bonding trials are performed with both quartz crystal microbalance (QCM) and ZnO lateral field excitation (LFE) solidly mounted resonators (SMR). Some devices are functionalized for binding the FITC molecule, while others are prepared without antibodies to serve as reference sensors.

5.2 Surface Chemistry

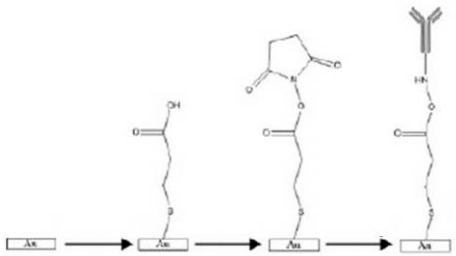

Figure 28: Chemical structure and steps for constructing the self-assembling monolayer.

For all aqueous measurements, self-assembling monolayers (SAM) immobilize antibodies on the surface of each device. A gold substrate is required for the initial thiol covalent bond. Figure 28 outlines the steps to construct the SAM layer. The following are the treatment steps for preparing each of the devices for antibody immobilization:

1. All surfaces were cleaned with a solvent waste. Acetone, Isopropanol and methanol then subsequently rinsed with deionized (DI) water and dried with a nitrogen gun.

2. For 10 minutes, the gold substrate of the top electrode was exposed to a 0.01 M concentration of 3,3'-Dithiodipropionic acid (3,3"-DTP) in ethanol for the formation of the initial sulfide bond. The surface was again rinsed with DI water and left to dry.

3. For an additional 10 minutes, the surface of the device was treated with a 0.42 M of 1-ethyl-3-(3-dimethylamino-propyl) carbodiimide (EDC) and 0.67 M of N-Hydroxysuccinimide (NHS) dilution in TAE buffer. Again the surface is rinse with DI water. This step creates the amine-terminated head group atop the immobilized alkanethiol that will be reactive to the primary amine groups of any subsequent antibody or protein.

4. Next for over 30 minutes, the prepared surface is exposed to monoclonal mouse anti-FITC (Sigma-Aldrich) antibodies at a concentration of 20 μg/ml in PBS. After a final rinse of DI water the device are now prepared to be exposed to the target antigen.

Phosphate buffered saline (PBS) solution was selected as the solvent of choice for each of the trials as it presents a similar ion concentration as that of human serum [67]. It contains concentrations of sodium chloride, potassium phosphate and other common biological ions, and has been widely used in the biological research field. However the target antigen, Fluorescein Isothiocyanate (FITC) is only slightly soluble in water-based solutions (such as PBS buffer). Therefore, we have selected a fluorescein sodium salt (Sigma-Aldrich) derivative to increase the water solubility of the antigen. Although this molecule is a derivative of the target FITC molecule, it still maintains a high binding affinity for the selected Anti-FITC antibodies that will be verified in the following section with fluorescence imaging and has been used in previous experiments [30]. The buffer solution was purchased as a 1X dilution of PBS from Sigma-Aldrich stored at room temperature. The solution with FITC was prepared in a 1 mM dilution in PBS buffer by constant agitation for several minutes.

5.3 Fluorescence Imaging

Other environmental factors can alter a sensor's response separate from the actual detection of the target antigen. These noise sources can stem from causes such as temperature changes, interfering antigens, and human error. It is essential to differentiate a true detection event from noise signals to properly analyze a sample. Reference sensors that are not functionalized for the target antigen yet are exposed to the same sample can serve as a control for the experiment. They allow the user to isolate the true detection response from the noise signals.

With the array configuration outlined in Section 2.3.2, the inclusion of reference sensors requires that devices are separately functionalized. Using the fluorescence of the FITC molecule, Figure 29 is an example of separate device treatment for a ZnO multi-modal SMR array. SAM layers were constructed based on the protocol in the previous section in order to immobilize anti-FITC molecules on specific devices. Subsequently, each device was exposed to the target antigen and imaged with a GE Typhoon™ Trio Plus imager. Table 13 outlines the typical excitation/emission wavelengths for the FITC molecule and the selected excitation laser and filter for the imaging system.

The SMR device array shown in the image is not molded in electrical packaging or in the developed USB module for this dissertation. The diced die was positioned on top of the scanner with several standard droplets to verify correct operation of the system. These device were not used for the trials following this section, only for the creating the images to verify the surface chemistry.

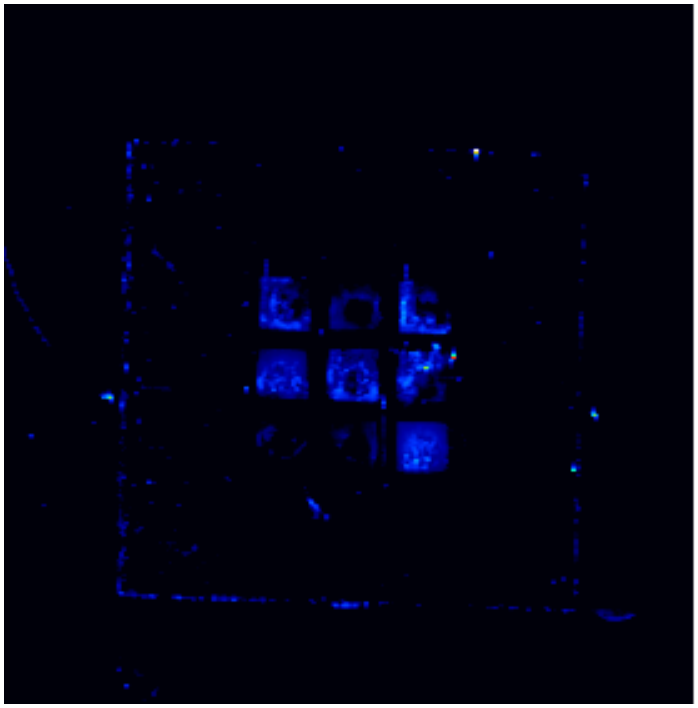

Figure 29: Fluorescence image of ZnO multi-modal SMR array.

Table 13: Optimal excitation/emission wavelengths from FITC molecule. Actual GE Typhoon Trio settings for fluoresence imaging.

Fluorescein Material Properties	Excitation Wavelength	Emission Wavelength
	460 nm	515 nm
GE Typhoon Settings	Excitation Laser	Emission Filter
	488 nm (Blue)	520 ± 20 nm

5.4 QCM Measurements

As mentioned in Section 1.3.6, QCM devices are the most widely used gravimetric sensors for biological detection. Here we use these devices as a benchmark to compare the performance of the proposed system (ZnO SMR). The purpose of the comparison is to serve as a validation of operation rather than proving the superiority of the proposed technology as that is outside the scope of this work.

Two QCM devices were treated with the antibody immobilization protocol described in Section 5.2 to functionalize the devices for FITC; while the other two QCM devices where left untreated to serve as reference sensors. Due to the size and orientation of the devices

(top electrode diameter has a surface area of 130.70 mm^3) the flow cell designed for these devices can only expose one sensor at a time. Therefore, each measurement was repeated for each device and the final results were then compared and are reported in Section 5.6. Syringe pumps were utilized to control the flow rate of the buffer/antigen solutions for each trial ($\approx$ 4 ml/min). 1X PBS buffer solution was flowed over the sensors prior to the exposure of a 1 mM concentration of FITC and lastly PBS buffer again to remove any unadsorbed antigens.

5.5 ZnO SMR Measurements

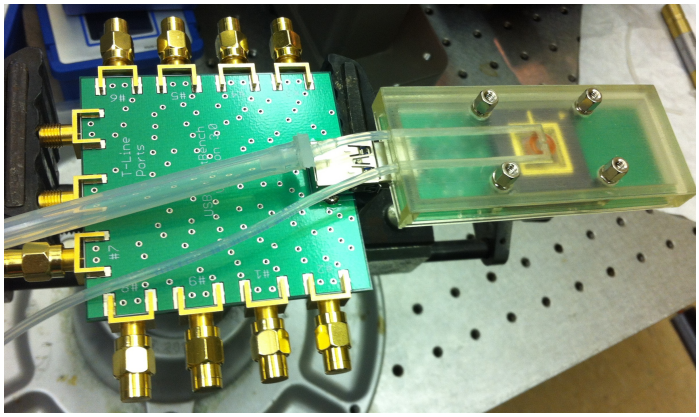

Figure 30: Complete module setup for aqueous measurements.

Figure 30 shows the experimental setup for the electrical characterization and solution exposure of the ZnO LFE SMR devices to the FITC solution. Similar to the array in Figure 29, prior to the trial three devices were functionalized for FITC, and two devices served as reference sensors. The same exposure protocol for the QCM devices was used for the module, 1X PBS buffer, 1 mM concentration of FITC and lastly PBS buffer solution to rinse away any unbound antigens.

Although the test bench is set up for simultaneously characterizing multiple devices in real time, the characterization system (HP 8853 vector network analyzer) is only capable of taking one port measurement at a time (S_{11} Parameter). Therefore, one functionalized device was selected for a prolonged monitoring. Each solution exposure was allowed to

reach equilibrium within several minutes and then all other devices were characterized. After the complete trial was performed once, the trial was repeated again for the reference sensor plot to be established.

5.6 Results Comparison

Figures 31 and 32 show the sensor response for two devices; one functionalized for FITC and one as a reference. Figure 31 displays the sensor response for the QCM devices; showing the transition from the initial 1X PBS buffer solution to the initial exposure of the FITC solution. Figure 32 shows the sensor response for the ZnO SMR devices for the same transition (from PBS to FITC solution). However, for this plot we apply a window average to both the functionalized and reference sensor response. In order to better illustrate the transition of the anti-FITC sensor as these measurements were broadband to include all device resonances and consequently had low resolution. Also, the standard deviation of the reference sensor response was higher than normal (±3.13 MHz) likely due to device connectivity issues. The raw sensor response plots are included in Appendix A.2. Table 14 outlines the average and standard deviation property values for each sensor type based on the initial loading event caused by the PBS buffer solution.

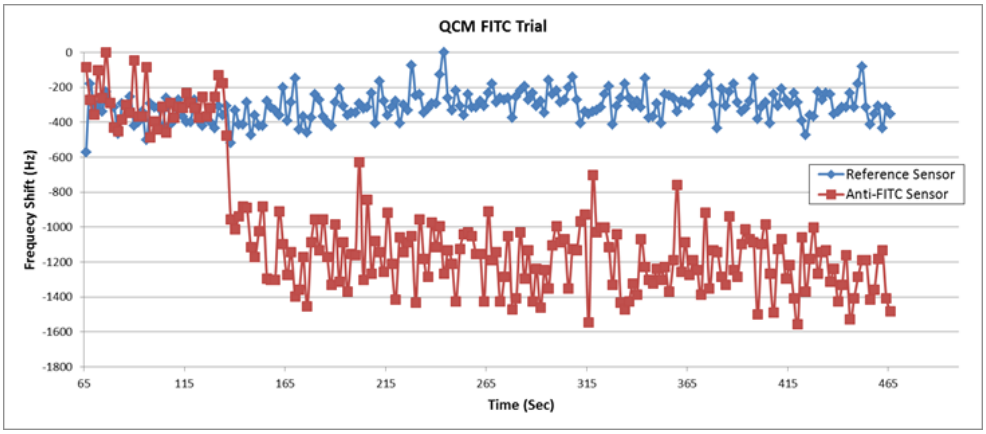

Figure 31: QCM sensor response plot to 1X PBS buffer solution (<120 sec) and 1 mM solution of FITC (>120 sec) for both anti-FITC functionalized and reference sensors.

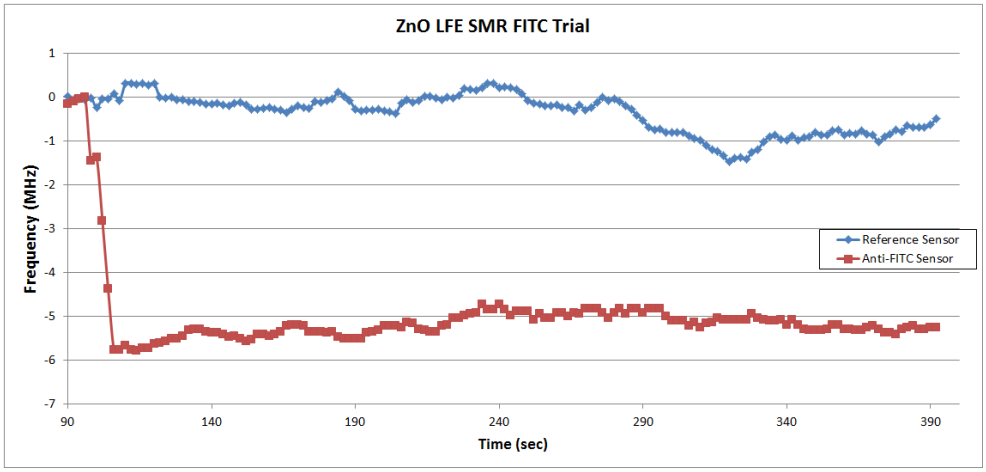

Figure 32: ZnO LFE TFBAR sensor response plot to different solutions. 1X PBS buffer and 1 mM solution of FITC for both anti-FITC functionalized and reference sensors.

Table 14: Average device properties and standard deviations for 4 devices of the QCM and 5 devices of ZnO SMRs used. The unloaded, loaded resonant peak and frequency shift values are based on the loading event caused by the PBS buffer solution.

Device Type	Unloaded Frequency (MHz)	Unloaded Peak Power (dB)	Loaded Frequency (MHz)	Loaded Peak Power (dB)	Average Frequency Shift
QCM	29.97±0.021	-13.28±9.225	29.96±0.021	-1.831±0.323	4.176±1.543 (KHz)
SMR	1124.94±101.54	-27.945±2.42	818.47±96.07	-15.895±7.484	241.32±129.20 (MHz)

While Figures 31 and 32 illustrate the frequency shifts over the allotted time for the each trial, we now examine the individual shifts of the S_{11} parameters for individual devices; both for the reference and the functionalized sensors. For the QCMs, we display the characterization curves of the reference sensor (Figure 33a) and the anti-FITC sensor (Figure 33b). The reference sensor was initial unloaded as it was not treated with the antibody immobilization protocol; therefore, it demonstrates the large change in Q factor that is expected from liquid loading of a gravimetric sensor. The zoomed in plot shows the minor difference in the resonant frequency before and after the introduction of the FITC antigen. While the anti-FITC sensor, shows a significant shift upon exposure to the target molecule in reference to the PBS buffer sensor response.

For the ZnO LFE SMRs, the S_{11} characterization plot for the reference sensor is shown in Figure 33c and the anti-FITC sensor is in Figure 33d. As discussed prior, the reference sensor in this situation was characterized in a separate trial after the initial trial for the anti-FITC sensor. Therefore, even with the introduction of air into the chamber, the device remained liquid loaded and exhibits minimal differences between the air and the PBS/FITC response curves. For the anti-FITC sensor, we see the expected performance for the device; a larger negative shift in the resonance with the initial loading of the PBS buffer and a smaller response to the binding of the FITC molecules to the surface of the device.

Figure 34 display the magnitude of the impedance for both of the devices (QCM, Figure 34a and SMR, Figure 34b). These plots are based on the S_{11} parameter data from the anti-FITC devices exposed to the different environments. From these plots we can extract information such as the series and parallel resonances, which are the local minimum and maximum impedance respectively around the resonant frequency. However for the measurements conducted in this experiment, the measurement range was determined in order to provide the required resolution to properly monitor shifts in the resonant frequency and at times it excludes the series resonance from the measurement (especially for the QCM devices, Figure 34a).

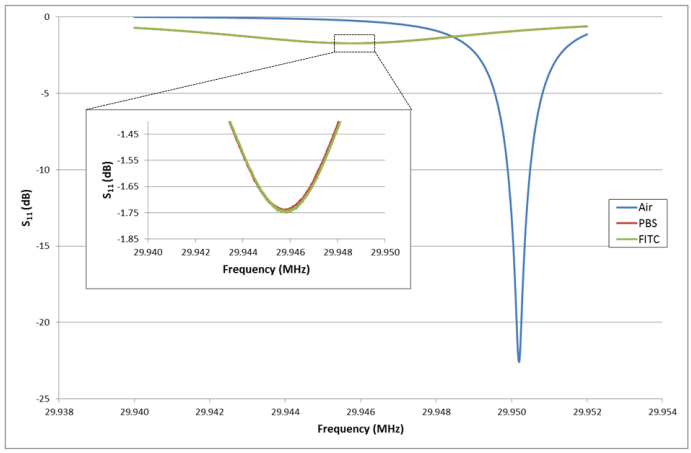

(a)

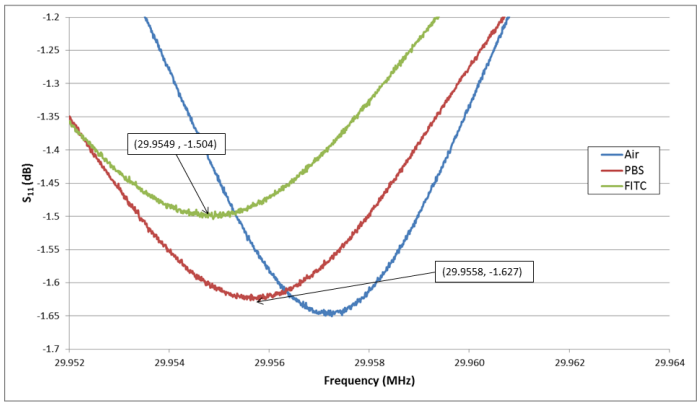

(b)

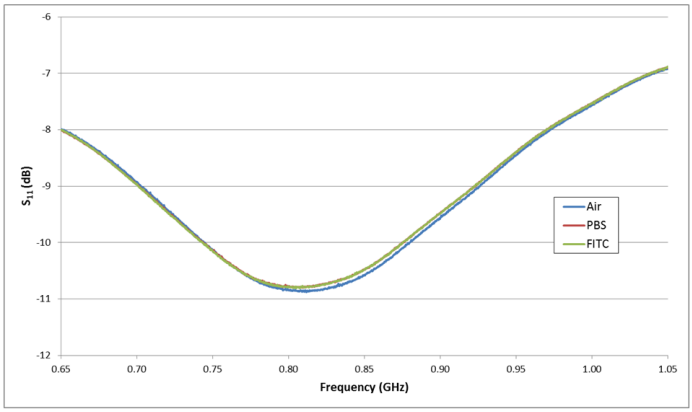

(c)

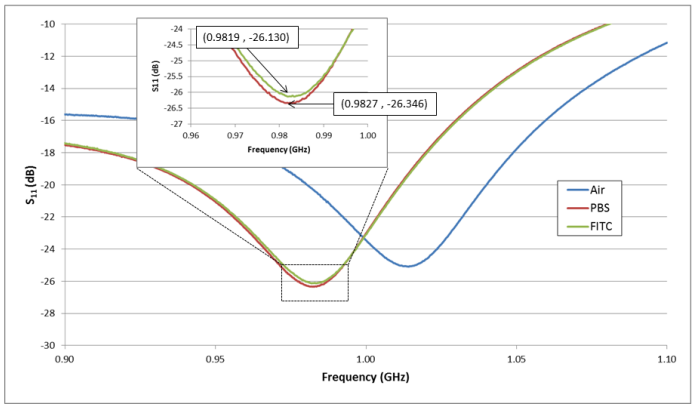

(d)

Figure 33: S_{11} characterization plots for a) QCM reference, b) QCM anti-FITC, c) SMR reference, d) SMR anti-FITC sensors exposed in order to air, PBS buffer and FITC solution.

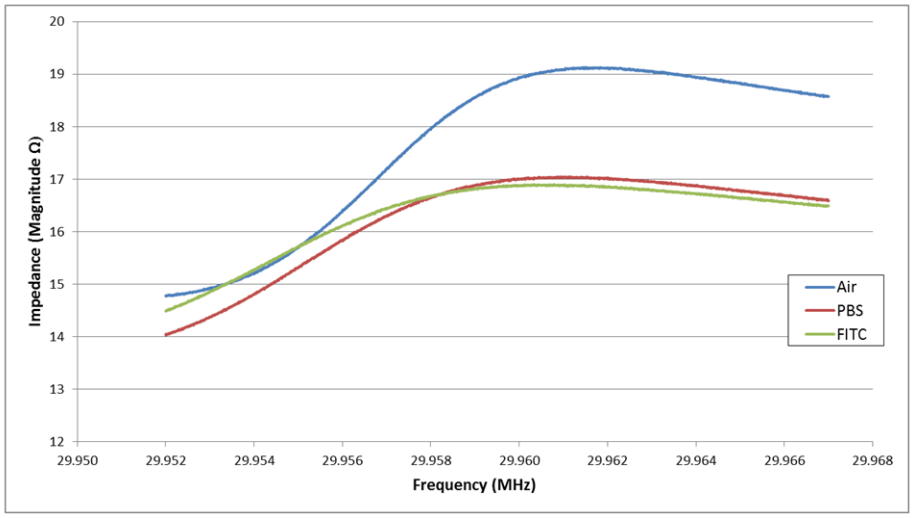

(a)

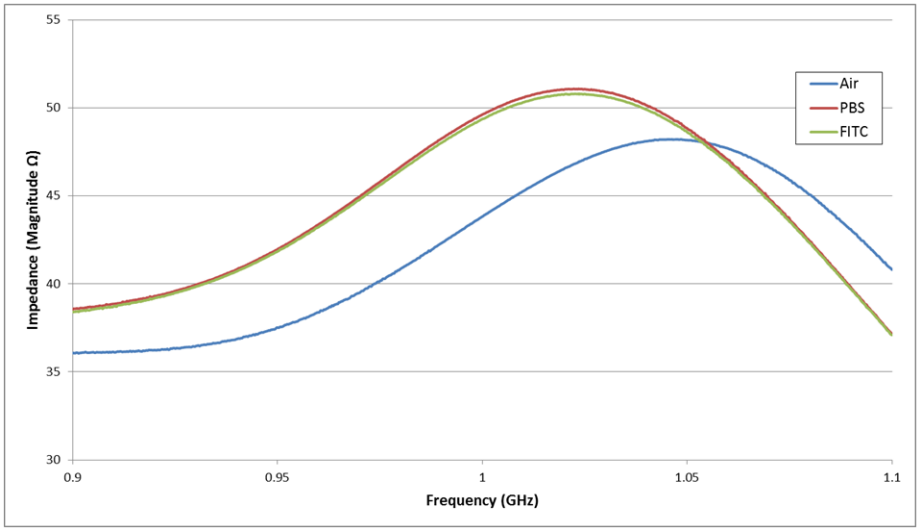

(b)

Figure 34: Magnitude of impedance response curves for a) QCM and b) SMR functionalized with anti-FITC and exposed in order to air, PBS buffer and FITC solution.

5.7 Theoretical Extrapolation of Sensor Parameters

Based on the measure values of previous trials, the following is a derivation of the sensor parameters for each device (QCM, ZnO SMR). For the QCM measurement, two sensors were functionalized with anti-FITC, and two sensors were untreated and served as reference. For the ZnO SMRs, two sensors were functionalized, and three sensors served as reference. Table 16 shows the average frequency shifts and device properties.

Table 15: Average device properties and resultant frequency shifts.

Device Type	Resonant Frequency (MHz)	Surface Area (m^2)	FITC Binding Shift (MHz)	Reference Shift (MHz)
QCM	29.9508	$0.1307x10^{-3}$	$8.898x10^{-4}$	$5.81x10^{-5}$
ZnO SMR	859.50	$0.48x10^{-6}$	1.8808	0.086

Biosensors are assessed based on their performance for a particular application. The metrics that quantify biosensors are their detection limit, saturation level, dynamic range, sensitivity, and selectivity. These values are determined based on the selected sensor's response curve for a particular application. Figure 35 shows an example of a gravimetric device response curve to varying concentration of the analyte (antigen) and how the response correlates to these parameters.

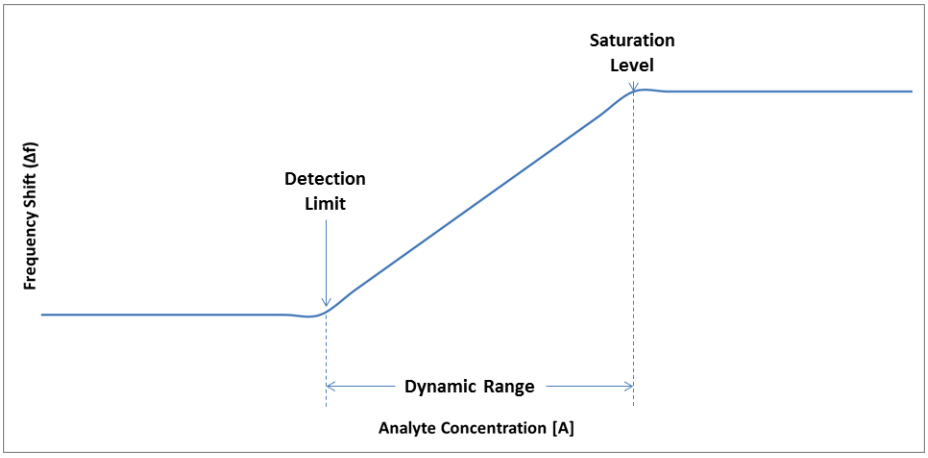

Figure 35: Example gravimetric sensor response correlated to biosensor parameters.

The Detection limit can be represented as the antigen concentration or amount of adsorbed mass on the biosensor at which the binding event can no longer be distinguished

from noise signals. For this derivation, the frequency shift of the reference sensors will serve as the detection limit as it represents the noise floor of the trial.

The saturation level is the concentration or amount of adsorbed massed at which all binding sites are occupied and any higher antigen concentrations will give the same sensor response, e.g., frequency shift. Li et al. performed a tapping-mode atomic force microscopy (TM AFM) analysis of antibody-antigen interactions utilizing a similar SAM gold substrate immobilization as the one outlined in Section 5.2 [5]. Figure 36 is the image which Li et al. demonstrated the observed surface density of the adsorbed immunoglobulin proteins. Based on this image, we utilize a surface density of 0.3225 ng/mm^2, each device's surface area, and the two binding sites for each selected antibody to determine the maximum binding sites (Table 17).

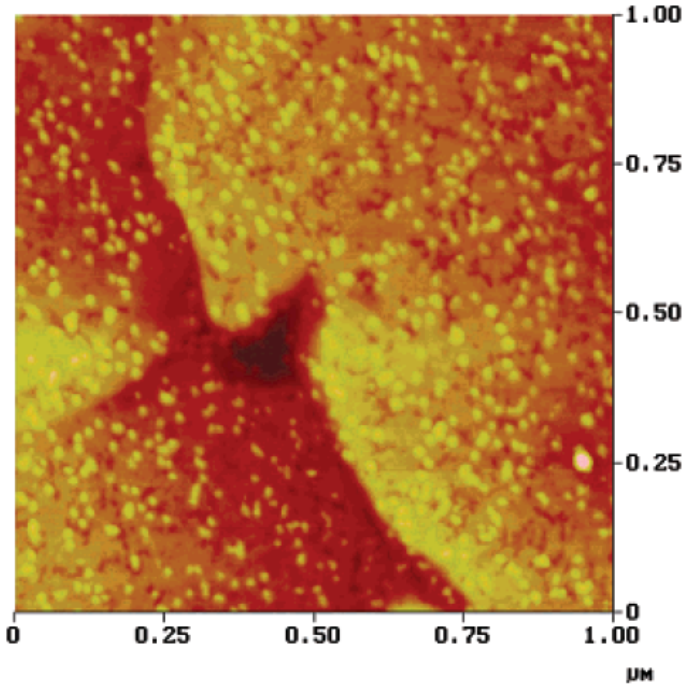

Figure 36: TM AFM image of immobilized antibodies for 100% C15COOH SAM immobilization presented by Li et al. [5].

Sensitivity is the ratio of loaded mass to shifts in the detection mechanism of the sensor, for example, resonant frequency. In order to determine this parameter, we need to utilize the governing equation for the device that couples the detection mechanism to the loaded

mass. Several equations have been developed to emulate the biolayer formation on the surface of a gravimetric sensor such as equation developed by Hunt et al. presented in Section 2.1.1. However, for this trial we do not have enough data to determine equation variables such as viscosity changes.

Therefore, we will utilize the Sauerbrey equation (Equation (1)) to define the sensitivity of each device. Typically, the Sauerbrey equation is not applicable for aqueous sensing environments as it assumes that loaded mass has similar density and stiffness to the underlining substrate. Instead, we will modify the equation to simulate the mass loading caused by the last layer of the biofilm, i.e., the antigen adsorption. Instead of using the density/stiffness of the device substrate, we use the density of the target antigen and solve for the stiffness introduced to the device which should take into account the "softness" of the biolayer. Equation (23) is the algebraically reordered form of the Sauerbrey equation to solve for the sensitivity (Δm/Δf). Table 16 outlines all of the known material properties for the biomolecules within each trial from the manufacturer (Sigma-Aldrich) and a chemical properties repository.

$$\frac{\Delta m}{\Delta f} = \frac{A\sqrt{\rho\mu}}{2f_o^2} \tag{23}$$

Table 16: Molecular properties for FITC and anti-FITC.

	FITC Molecular Weight (M_A) [68]	Anti-FITC Molecular Weight (M_B) [69]	Density of FITC [70]
Value	376.3	150,000	1543.0 kg/m^3

The Dynamic range is the difference between the detection limit and the saturation level. This linear region (Figure 35) denotes the concentration range at which the device can properly operate for the target antigen. Selectivity is a measurement of the robustness of a sensor's dynamic range with increasing concentrations of an interfering antigen. For now, we will not define this value as it is specific for a type of interfering analyte and the sample used in this trial consisted of purified FITC molecules dissolved in buffer solution with no anticipated interferants.

Gravimetric sensors signal response is directly correlated to the amount of mass adsorbed on the surface of the device. In order to correlate the immobilized mass to the solution concentration, we apply a Langmuir isotherm model to represent the linear region of the sensor response curve. An isotherm equation describes the equilibrium behavior of the adsorption process based on an unbound analyte molar concentration in the surrounding solution [71]. Equation (24) is the Langmuir isotherm equation.

$$Q = Q_{max}\frac{K[A]}{1 + K[A]} \tag{24}$$

Q and Q_{max} are the current/maximum adsorption capacity. $Q = p * M_A/M_B$, were p is the number of occupied binding sites and M_A and M_B are the molecular mass of the antigen and antibody respectively. K is the equilibrium constant which is the ratio of the kinetic association and dissociation rate constants. $[A]$ is the molar concentration of the antigen within the bulk of the solution [71].

In order to determine the equilibrium constant (K) in equation (24), we utilize a protocol developed by Skládal [72]. A non-linear regression is applied to fit both the equilibrium and dissociation regions of a gravimetric sensor's response (frequency shift vs time). Based on equation (25) and (26), the kinetic rate constants, association k_f and dissociation k_r, can be determined.

$$f = \frac{k_f c f_{max}}{k_f c + k_r}\left\{1 - exp\left[-(k_f c + k_r)t\right]\right\} \tag{25}$$

$$f = f_{max} exp\left(-k_r t\right) \tag{26}$$

f (f_{max}) is the current (maximum) frequency shift of the device and c is the molar concentration of the analyte. After determining both rate constants, the equilibrium constant is determined because $K = k_f/k_r$.

5.7.1 Solution Steps and Results

As mentioned previously, all following derivations are based on the average values presented in Table 15. We make the assumption that the bulk concentration of the analyte is

above the saturation level for each device; therefore, all binding sites are occupied at equilibrium. The following are the derivation steps to determine all unknown values/constants in both the Sauerbrey and Langmuir isotherm equations:

1. Determine the stiffness constant (μ) by calculating total change in mass (Δm) assuming all available binding sites are occupied (p_{max}) by the target antigen (FITC).

2. Determine the sensitivity of each device with the stiffness found in Step 1 and based on Equation (23).

3. Utilize the protocol developed by Skládal [72], to determine the kinetic association (k_f) and dissociation (k_r) rate constants and subsequently the equilibrium constant (K) for each device.

4. Utilizing equation (24), the equilibrium constant (K) from Step 3, and the sensitivity ($\Delta m/\Delta f$) for each device from Step 2, to determine the molar antigen concentration at the extremes of the dynamic range. The detection limit is determined by establishing the amount of mass adsorbed at the noise floor (i.e. the frequency shift of the reference sensors). The saturation level is determined at the point in which 97% of the binding sites are occupied.

Table 17 outlines all of the intermediate constant values; and Table 18 shows the final sensor parameters after the complete derivation. These values are serve as estimates; typically, biosensor parameters are determined after multiple experiments by varying analyte concentrations over the dynamic range [73]. However, the primary focus of this chapter was to provide evidence that ZnO SMR can serve as immunosensors within aqueous environment. Future work would need to be conducted to properly determine these application specific biosensor parameters.

Table 17: All values of the intermediate constants for this process.

Device Type	Total binding sites (p_{max})	Stiffness (μ) (N/m)	Sensitivity (g/Hz)	Association Constant (k_f)	Dissociation Constant (k_r)	Equilibrium Constant (K)
QCM	$3.384\text{x}10^{11}$	$6.899\text{x}10^{-9}$	$2.377\text{x}10^{-13}$	$4.26\text{x}10^{-4}$	$3.68\text{x}10^{-8}$	$1.16\text{x}10^{4}$
ZnO SMR	$1.243\text{x}10^{9}$	$1.0472\text{x}10^{-9}$	$4.130\text{x}10^{-19}$	0.365	$4.87\text{x}10^{-6}$	$7.48\text{x}10^{4}$

Table 18: Derived biosensor parameters.

Device Type	Detection Limit	Saturation Level	Sensitivity	Dynamic Range
QCM	10.57 pg/cm^2 @ 6.023 μM	323.58 pg/cm^2 @ 2.863 mM	0.238 pg/Hz	0.006 - 2.8 mM
ZnO SMR	7.40 pg/cm^2 @ 0.641 μM	161.95 pg/cm^2 @ 0.432 mM	0.413 fg/kHz	0.0006 - 0.4 mM

5.8 Conclusion/Discussion

The complete proposed module system (wafer die, USB circuit board and fluidics packaging) was tested experimentally as a biosensing platform. The functionalization protocol was first verified with florescence imaging of antibodies binding FITC molecules. Next, a binding trial was performed with QCM sensors to verify proper operation with gravimetric sensors. Subsequently, ZnO LFE SMR devices were characterized within the module system during exposure of a FITC solution, containing both reference and FITC-sensitive devices. Based on the measurements of both FITC binding trials, each sensor's parameters were derived by applying both Sauerbrey and Langmuir isotherm equations.

Figure 32 shows the ability of the proposed system (ZnO SMR) to serve as transducers for biological sensing. The sensor response plot is essential to biosensors, as monitoring shifts in the detection mechanism serves as the means to extract the analytical information from a sample under test. The following chapter outlines a protocol for extracting features from this type of plot to further probe the data. Although the following protocol is based on QCM frequency shift data, the procedure can be applied to sensor data from an array of ZnO SMR devices.

CHAPTER 6

DEVELOPMENT OF CLASSIFICATION MODELS FOR IMMUNOSENSOR MEASUREMENTS

Raw immunosensor data requires further processing in order to extract analytical information from the device characterization. Discrete features, for instance, changes in the detection mechanism of the device, serve as the means for drawing conclusions about the environment under test. For piezoelectric resonators, the primary feature is the total shift in resonant frequency of the device after the target antigen adheres to the surface and subsequently, unbound antigens are washed away. The resultant value can then be correlated to biomarker concentrations or other features of the aqueous sample, for example, changes in viscosity.

The focus of this chapter is to apply pattern recognition algorithms to immunosensor data in order to produce classification models using a facilitated learning process. We develop a protocol for three types of classifiers, two linear classifiers and one Bayesian classifier from an initial training set. This protocol was applied to a label-free QCM-D based immunosensor functionalized by an alkanethiol self-assembling monolayer (SAM) with binding affinities for pAkt, γH2AX, β-Actin, and FITC biomarkers. Each model separated the training trials into two classes: HPV-positive (SCC47) and HPV-negative (TU212). The aforementioned technology and target proteins were selected as an example to illustrate the protocols ability to define classification models. However, this protocol can be applied to other types of sensing platforms customized for other diseases (i.e. ZnO SMR for cancer detection).

6.1 Training Set

For the aforementioned system, we have selected oropharyngeal or head and neck cancer (HNC) for the disease of choice to test out this protocol. HNC accounts for about 3%

(34,540 cases) of new cancer cases per year in the United States and about 2% (7,880 causalities) of all cancer deaths in 2010 [1]. High risk human papillomavirus (HPV16) has been identified as a causative agent in oropharyngeal cancer pathogenesis [74], and it has been estimated that HPV-positive cancers account now for about 70% to 80% of all oropharyngeal tumors [75]. Recent clinical data suggest that HPV-positive status is an important prognostic factor associated with a favorable outcome in head and neck cancer patients [76, 77].

In this study, the expression of four proteins in cell lysates, which are extract from cancer cells, were evaluated from HPV-positive (SCC47) and HPV-negative (Tu212) HNC cell lines. In particular, the expression of two proteins, γH2AX and pAkt, have been shown to correlate with cellular survival in response to radiation treatment [78, 79]. In the field of molecular biology, protein concentrations are determined in order to evaluate gene expressions with in a sample. These measurements are typically normalized by a positive control which is a protein that is equally expressed in all samples. For this study, we will use β-Actin as a positive control [80] because the expression pattern is conserved between both HPV-positive and HPV-negative cell types. Antibodies for FITC were used as a negative control to negate any non-specific binding.

6.2 Sensor Platform

Quartz crystal microbalance (QCM) biosensors have been used as a means to detect the presence and properties of target molecules within both vapor and aqueous applications [26]. QCM sensors are bulk acoustic wave (BAW) cavity resonators consisting of a piezoelectric crystalline substrate, as discussed in Section 1.3.6. Biolin-Scientific has developed a system called Q-Sense E4 module, a quartz crystal microbalance with dissipation measurements (QCM-D) platform that provides real-time tracking of both resonant frequency and energy dissipation. For the following study, only frequency shift measurements are

used to correlate this data with other types of immunosensors with only one type of detection mechanism (i.e. ZnO SMR).

6.3 Introduction to Pattern Recognition Techniques

Pattern recognition techniques allow for the identifying and extraction of more beneficial information from a data set also known as data mining. Historically, cancer biomarker detection has focused solely on the presence or variations in concentration levels of the target molecule [81]. This type of analysis has led to much debate about the validity of each individual biomarker as elevated concentration levels vary from patient to patient and can derive from multiple causes. Even currently accepted biomarkers such as prostate specific antigen (PSA) have again been questioned by new research data [39]. Therefore, pattern recognition algorithms may provide more robust models for reducing false positives and increase diagnostic accuracy.

Several types of pattern recognition algorithms have been previously appllied to analyze antibody-antigen interactions for different biological applications. Tsai et al. utilized multivariate statistical analysis of ELISA measurements to determine the influence of surface-bound fibrinogen on platelet adhesion to biomaterials [82]. Wagner et al. utilized principal component analysis to characterize absorbed protein films for biological implants based on time-of-flight secondary ion mass spectrometry measurements [83].

In this study, we have utilized several types of pattern recognition algorithms to develop each classification model. For the linear classifiers, Kozinec's algorithm creates an optimal discriminant function that maximizes the marginal separation from the training data set [84]. One downside of linear classifiers is that they require the data set to be linearly separable or rather that the Gaussian regions that define the data set to have minimal intersection. Bayesian classifiers utilize a priori probability to minimize the risk of a misclassification [85]. The optimal solution to this problem then leads to the creation of the Bayesian divisor. This divisor defines regions of which subsequent trial values have a high probability to be

assigned to the respective class, even for cases in which data is not linearly separable [85].

Franc and Hlaváč developed a statistical pattern recognition toolbox (SPRTool) that incorporates both algorithms for open source use and incorporation into developed systems [84]. All classification models were developed with SPRTool and results are reported for each model.

6.3.1 Kozinec's Algorithm

The Kozinec's algorithm [86] is an iterative process for developing a linear classifier with maximal margin from the training data sets. Schlesinger improved the algorithm by incorporation of a marginal solution condition allowing for faster convergence [6]. Franc and Hlaváč further developed this algorithm expanding its capability to solve non-linear and non-separable data sets [6]. However, we limit our scope to linearly separable data sets utilizing supervised learning approach.

The goal for Kozinec's algorithm is to define a separating hyperplane which completely separates 2 data sets. The hyperplane has the form seen in equation 27.

$$< \omega \cdot x > + b = 0 \tag{27}$$

Where $\omega \in R^N$ is a vector of size N, the number of selected features which is further expounded upon in Section 6.5. $x \in X_1 \cup X_2$ is one of the data vectors from either of the training sets. The $< \cdot >$ notation serves as the dot product and $b \in R$ is a scalar offset.

Initially, the Kozinec's algorithm performs a transformation on the training data vectors and the hyperplane. The modified hyperplane now passes through the origin and all indices in both training sets are inverted with respect to the hyperplane. Figure 37 and equation 28 shows an example of the transformation (X' is the transformed data vectors of the training set, see Reference [6] for more details).

$$< \omega' \cdot x' >= 0; \quad \omega' = [\omega \; b]; \quad x' \in X' \tag{28}$$

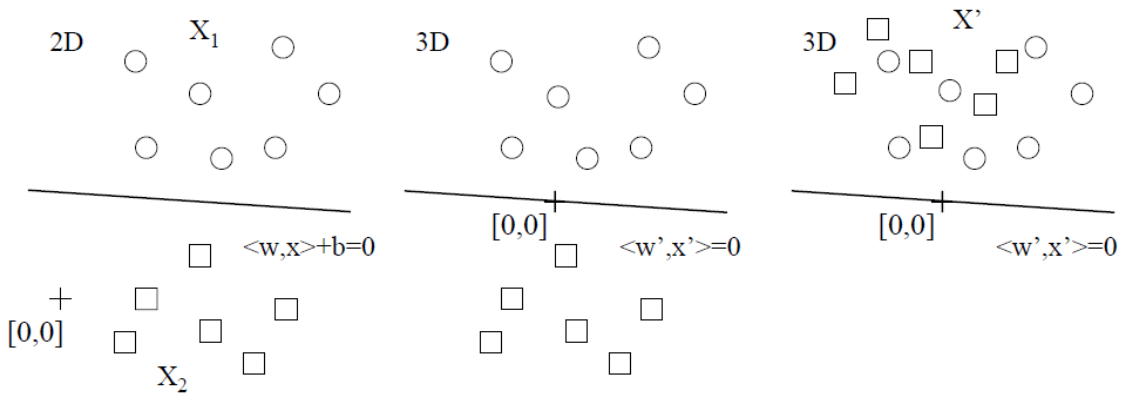

Figure 37: Example transformation space performed for Kozinec's algorithm [6].

Utilizing the transformation space, the algorithm iteratively looks for a value of ω' that satisfies the formula $< \omega' \cdot x' > > 0, \forall x'$. Below is an overview of the steps taken by the algorithm.

1. Initialize ω' with random values.
2. Find any data vector $x' \in X'$ where $< \omega' \cdot x' > < 0$; If none exist within the set then stop loop and ω' is the solution.
3. Compute a new ω', return to step 2.

Franc and Hlaváč's implementation of the Kozinec's algorithm requires that the user specify the training data sets and ϵ. ϵ serves as a control variable that determines the stop condition of the algorithm. If $\epsilon < 0$, then the previous stop condition mentioned in step 2 above is used. If $\epsilon \geq 0$, then the value is used to solve for the ϵ-optimal solution according to Schlesinger's algorithm. For this project, we set $\epsilon = 0.01$ in order to utilize obtain a near optimal solution [84].

6.3.2 Bayesian's Algorithm

Classifiers developed with the Bayesian algorithm require two separate processes. First, probability density functions (PDFs) are developed in order to best characterize the data

set with minimal complexity. Second, a probabilistic algorithm is executed on the modified data set in order to define a divisor line based on decreasing the probability of making a false classification. This process can provide solutions to sets that are not linearly separable providing more analytical information from training sets that show no apparent statistically significant separation.

Gaussian Mixture models (GMMs) are utilized to develop the underlining PDFs. These GMMs are formulated by Maximum-Likelihood (ML) estimation. Each of the initial GMMs parameters (mean, covariance, and weight) are modified by ML estimation [84, 87]. This approach is similar to an agglomerative hierarchical clustering method, in which GMMs are merged to simplify the data set representation [87]. For this study, we select the SPRTool's mlcgmm function to perform the estimation, along with specifying the shape of the covariance matrix as diagonal.

With the assumption that the formulated GMMs best represent the complete training data set, we then apply a Bayesian risk reduction algorithm. The process involves developing a decision rule that classifies each data point without a priori information about its classification. This decision rule is iteratively modified to minimize probably of misclassification for each data point. This algorithm can also be implement on incomplete data set (for instance, if a comprehensive clinical data is not available); however we assume that the data set completely represents the problem space [84]. For this study, we utilize SPRTools bayescls Bayesian algorithm to develop the classifier seen in Section 6.8 below.

6.4 Experimental Setup

Materials: All antibodies were monoclonal IgG1 for β-Actin (Sigma-Aldrich), FITC (Santa Cruz), γH2AX (Cell Signaling), and pAkt (Cell Signaling). Reactants for the surface chemistry include 3,3'-Dithiodipropionic acid (3,3"-DTP), 1-ethyl-3-(3-dimethylamino-propyl) carbodiimide (EDC) and N-Hydroxysuccinimide (NHS) were obtained from Sigma-Aldrich. Squamous cell carcinoma of the head and neck (SCCHN) human cell line (TU212) used

for this study was established from a primary hypopharyngeal tumor. It was obtained from Dr. Gary L. Clayman's laboratory (The University of Texas M.D. Anderson Cancer Center, Houston, TX). The HPV-16-positive SCCHN cell line (UM-SCC47) was obtained from Dr. Thomas Carey, University of Michigan. The tumor cell line was grown in DMEM/F12 (1:1) with supplemented 5% fetal bovine serum.

6.4.1 Protocols and Procedures

Antibody Immobilization: Each gold plated QCM sensors was exposed to UV/Ozone treatment for 10 minutes, then submerged in a $H_2O/H_2O_2/NH_4$ (5:1:1) heated (75^o C) solution for 5 minutes, and subsequently rinsed with DI water and exposed to UV/Ozone treatment for an additional 10 minutes. Each sensor was then housed in the QCM-D chambers and initial resonant frequency values were obtained for each device. A self-assembled monolayer was then constructed on the surface of each sensor using 0.01M 3,3'-DTP in ethanol for 10 minutes, and exposed to a 0.42M/0.67M EDC/NHS dilution in TAE buffer for an additional 10 minutes [88]. Each of the four sensors was then inoculated with a different antibody (β-Actin, FITC, γH2AX, and pAkt) at a concentration of 10 ng/ml diluted in PBS buffer until the frequency drift is less than 2 Hz/min.

Cell Line Preparation: Whole cell lysates were extracted using lysis buffer containing 50mM Tris-Cl (pH 8.0), 150mM NaCl, 0.02% Sodium azide, 0.2% SDS, 2% Igepal CA-630, 0.5% sodium deoxycholate and protease inhibitor cocktail (Sigma Aldrich).

QCM Protocol: All trials were conducted in the flow chambers of the Q-Sense E4 module providing control of environmental factors, e.g., flow rate and temperature. After antibody immobilization and a PBS buffer wash off, lysate samples (1:20 dilution in PBS) of either SCC47 or TU212 were flown across all the sensors followed by a final PBS buffer wash off.

6.5 Feature Extraction Process

As mentioned previously, the designation of discrete features is essential for obtaining analytical information from raw sensor data. In this study, we utilize QCM-D sensors and monitor shifts within the resonate frequencies of each device. However, instead of just determining the value of the frequency shift prior to exposure to the target molecule and after a wash off set, we look to expand the feature set. We include the maximum to minimum frequency shift over the total period of lysate exposure (Fig. 38a). Previous studies have utilized the slope of resonant frequency shifts as a data feature in association with the antibody affinity and dissociation constants for the target antigen [82, 89]. Poitras & Tufenkji [90] developed a rapid detection biosensor for Escherichia coli (E. coli) utilizing the frequency shift within the first few minutes of sample exposure, focusing solely on the initial loading event. Utilizing the same approach, three regions of interest have been defined in which linear regression models were fitted to determine the slope. Each region correlates to the binding events between the antibody and target antigen [binding affinity (Fig. 38c), equilibrium (Fig. 38d), and dissociation (Fig. 38e)].

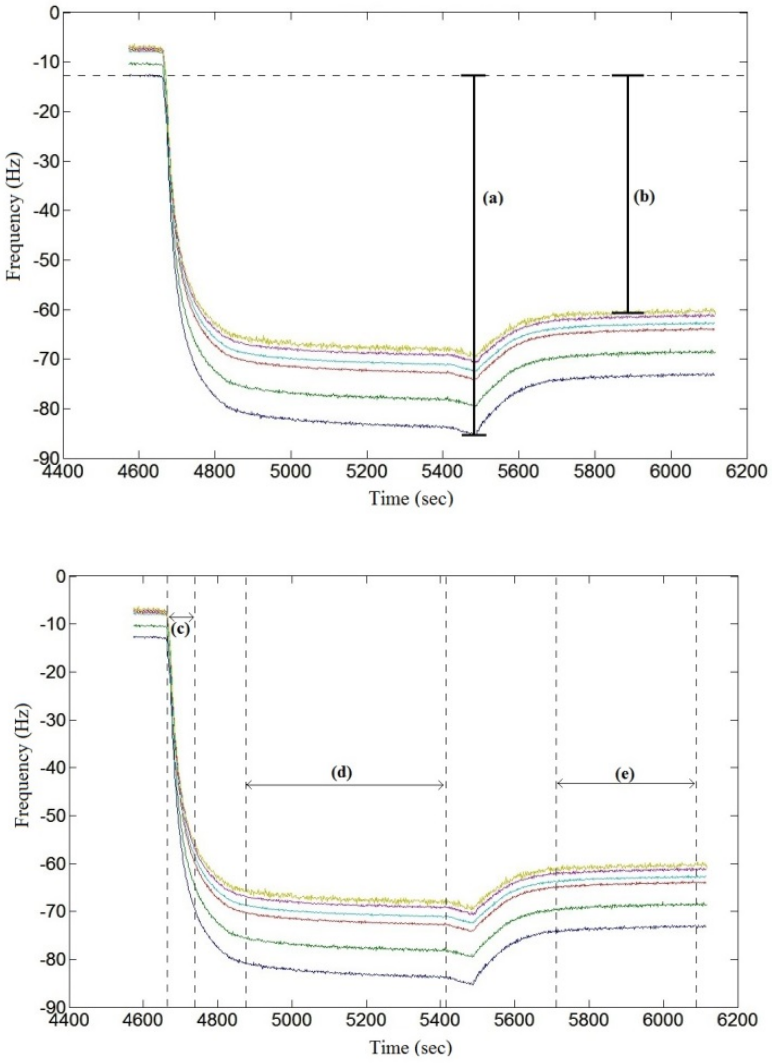

Figure 38: Definition of discrete features from raw frequency shift plots. With (a) Max-min and (b) normal frequency shifts and (c) binding affinity, (d) equilibrium, and (e) dissociation slopes.

6.6 Classification Model Development

Three trials for each lysate sample (6 trials total) were evaluated as the ”training” data set for developing each classification model. Each trial's feature sets were then normalized based on the value of the negative control (FITC) in order to remove the effects of non-specific binding (Eq. 29). Two or more features were then selected based on minimal standard deviations and maximum separation from the mean values; an example of a desirable selection is shown in Figure 39a.

$$X_f = X_{ij} - X_{kj} \tag{29}$$

X_f is the final feature value, i correlates to the selected target molecule (β-Actin, pAkt, γH2AX), j is the selected harmonic frequency value (3^{rd} to 13^{th}); therefore, X_{ij} is the raw feature value. Then, k is for the FITC value and X_{kj} serves as the negative control feature value.

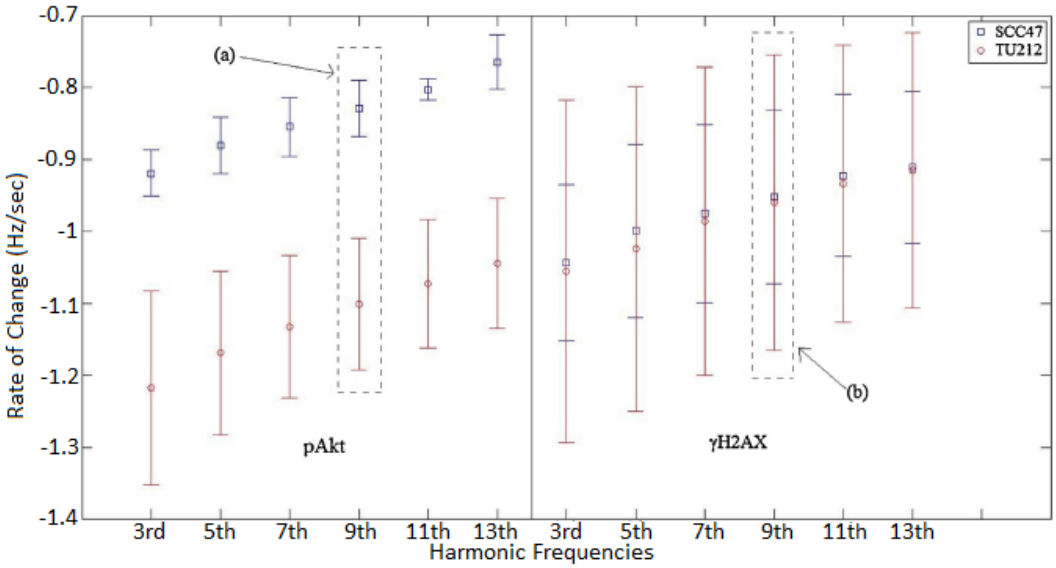

Figure 39: Example of the desire data separation.

6.7 Linear Classifiers

Gaussian distribution regions were plotted based on the selected features' mean and standard deviations values (Fig. 40). These regions define areas in which there is a high probability that subsequent trial frequency values would fall. The Kozinec's algorithm was then applied to define a linear classifier model. Prior to normalizing the data with the positive control, we observe several regions of statistical separation between feature values; this finding aligns with previous work [90]. Therefore, the 11^{th} harmonic values for β-Actin and 7^{th} harmonic values for pAkt were selected to develop the model seen in Figure 40.

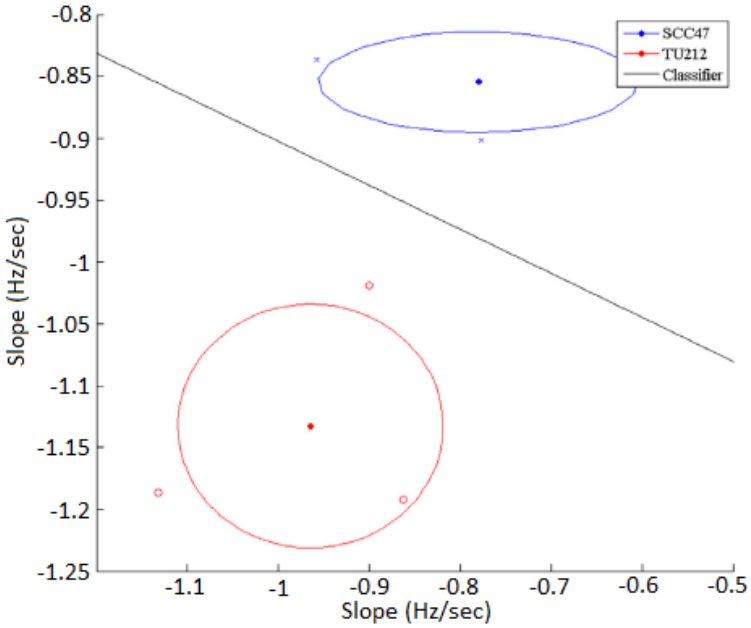

Figure 40: 2D classification model.

Table 19: Mean and standard deviation values for all initial loading slope features of test set prior to positive normalization.

Target Antigen	Value Type (Slope)	3rd Harmonic	5th Harmonic	7th Harmonic	9th Harmonic	11th Harmonic	13th Harmonic
β-Actin	SCC47	-0.89±0.183	-0.86±0.180	-0.83±0.177	-0.80±0.171	-0.78±0.176	-0.75±0.198
	TU212	-1.10±0.219	-1.06±0.218	-1.03±0.198	-0.99±0.171	-0.96±0.146	-0.93±0.111
pAkt	SCC47	-0.92±0.032	-0.88±0.040	-0.85±0.041	-0.83±0.039	-0.80±0.014	-0.76±0.038
	TU212	-1.22±0.135	-1.17±0.114	-1.13±0.099	-1.10±0.092	-1.07±0.089	-1.04±0.090
γH2AX	SCC47	-1.04±0.109	-1.00±0.120	-0.98±0.124	-0.95±0.121	-0.92±0.113	-0.91±0.105
	TU212	-1.06±0.238	-1.02±0.226	-0.99±0.215	-0.96±0.206	-0.93±0.192	-0.92±0.192

Many of the other feature values however displayed minimal statistical separation following only the negative control normalization. However, it can be noted that there were similar trends for several of the antigen expressions across harmonic values, alluding to more empirical information that can be utilized for model development (Table 19). We now utilized the feature values for β-Actin to serve as the positive control and the rest of the data is normalized based on the mean value of all the harmonic values for each individual trial (Eq. 30).

$$\mu = \frac{\sum_j X_{kj}}{6}, X_f = \frac{X_{ij}}{\mu} \tag{30}$$

k is the negative control normalized value for β-Actin and μ is the mean value of all the harmonic feature values for β-Actin. i correlates to the remaining target molecules (pAkt, γH2AX), and j is each individual harmonic (3^{rd} to 13^{th}); therefore, X_{ij} is the negative control normalized feature value for each harmonic mode.

After both positive and negative normalizations, the γH2AX (9th harmonic, equilibrium slope), pAkt (5th harmonic, total frequency shift), and γH2AX (7th harmonic, dissociation slope) were selected for developing the 3D model shown in Figure 41. The Kozinec's algorithm was incorporated to define a linear classifier model (not pictured for improved image quality).

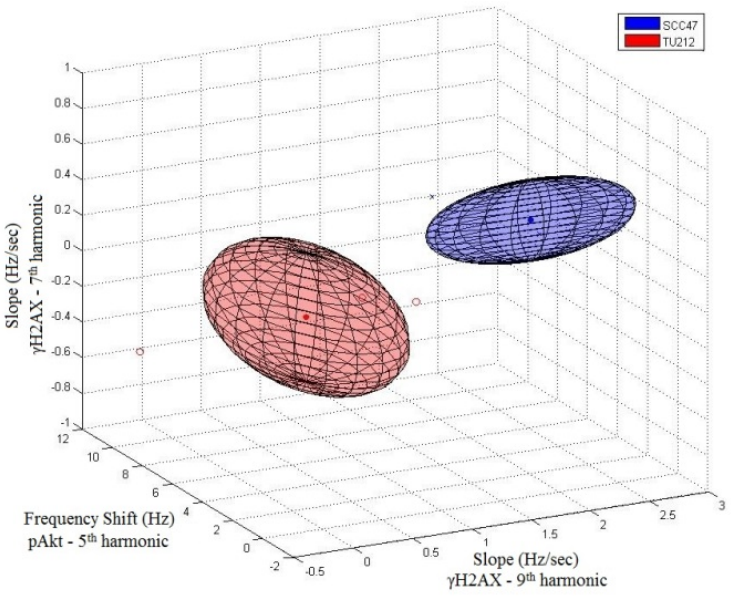

Figure 41: 3D classification model.

Table 20: Mean and standard deviation values for the 3D model after positive data normalization.

Equilibrium Slope Features Values							
Antigen	(Slope)	3rd Mode	5th Mode	7th Mode	9th Mode	11th Mode	13th Mode
pAkt	SCC47	-0.15±1.456	0.02±1.156	0.05±1.199	0.12±0.988	-0.05±1.109	-0.14±1.109
	TU212	1.73±0.606	1.83±0.834	1.87±0.788	1.85±0.885	1.76±0.797	1.74±0.864
γH2AX	SCC47	0.86±0.382	0.80±0.364	1.06±0.546	0.98±0.647	0.90±0.596	1.03±0.470
	TU212	0.65±0.840	0.55±0.928	0.59±0.693	0.47±0.594	0.39±0.787	0.33±0.807
Regular Frequency Shift Feature Values							
Antigen	(Shift)	3rd Mode	5th Mode	7th Mode	9th Mode	11th Mode	13th Mode
pAkt	SCC47	0.80±0.811	0.76±0.874	1.15±0.965	0.69±0.822	0.68±0.866	-0.13±1.964
	TU212	-0.74±1.888	-0.53±1.537	-0.37±1.568	-0.55±1.543	-0.38±1.474	-0.55±0.985
γH2AX	SCC47	19.91±31.14	4.76±5.081	11.31±16.52	8.08±11.026	6.50±8.668	11.86±18.26
	TU212	48.55±83.41	17.69±29.94	16.84±28.51	16.77±28.41	21.59±37.05	20.71±35.79
Dissipation Slope Features Values							
Antigen	(Slope)	3rd Mode	5th Mode	7th Mode	9th Mode	11th Mode	13th Mode
pAkt	SCC47	1.47±1.148	1.49±1.388	1.27±0.932	1.25±0.865	1.10±1.026	1.12±0.823
	TU212	0.35±0.584	0.59±0.284	0.50±0.226	0.19±0.615	0.24±0.313	0.28±0.207
γH2AX	SCC47	-0.10±1.649	0.51±0.847	0.20±0.995	0.76±0.527	1.24±1.110	1.33±1.674
	TU212	-3.56±4.565	-0.94±1.224	-0.10±0.362	0.23±0.331	0.29±0.570	0.46±0.894

6.8 Bayesian Classifier

In order to develop a more complex classification model, a Bayesian decision rule algorithm with Gaussian mixer models was incorporated. Although this model is capable of separating highly correlated feature sets, for simplicity and visualization purposes, a linearly separable training set with a training set of 30 values was selected. The training set for this model was extracted from the harmonic frequency values of the binding affinity slope in addition to the respective harmonic frequency values of the equilibrium slope for γH2AX. Only the 3^{rd} through the 11^{th} harmonic values were included because of the poor regression fits for the 13^{th} harmonic equilibrium region slope values (0.75±0.11). This feature set was selected to show the model's ability for class differentiation utilizing the normalize feature values of one target molecule (Fig. 42).

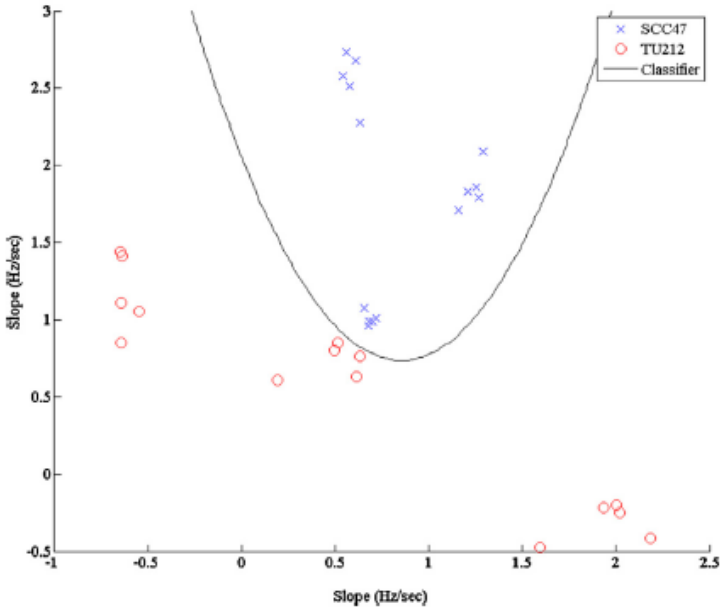

Figure 42: Bayesian classification model.

6.9 Conclusion/Discussion

A protocol for the creation of a set of classification models was developed to differentiate between biological samples based on immunosensor measurements. Sensor data was gathered using Au Quartz Crystal Microbalance with Dissipation (QCM-D) sensors inoculated with an alkanethiol self-assembling monolayer functionalized for the detection of pAkt, γH2AX, β-Actin, and FITC antigen expression. Oropharyngeal cancer lysate samples, both positive (SCC47) and negative (TU212) for high risk human papillomavirus (HPV16), were used to gather the classification model training data set. Subsequently, linear and Bayesian classifiers were formulated based on the extracted feature values and defined linear discriminant functions to distinguish between two classes: HPV-positive or HPV-negative cell lines.

This study serves to show the ability of this protocol to develop classification models based on the sensing platform and selected disease for immunosensor measurement. However, these models are not to serve as a comprehensive classification systems for HPV cell lysate samples. Developing such a system would require a more extensive training set taking into account biological variables for the selected disease. The goal of the classification would be to assist in the medical staff in reaching a particular prognosis for a patient. Figure 43 outlines an example in which features extracted from sensor response data can be correlated to potential disease diagnosis, e.g., cancer recurrence.

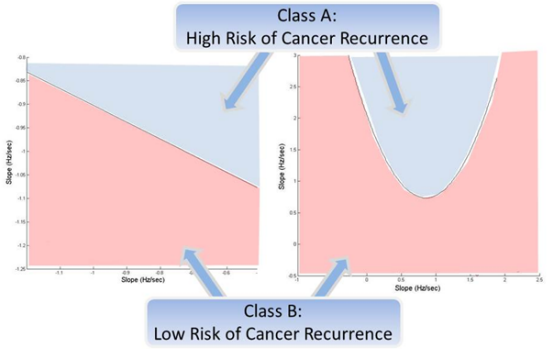

Figure 43: Example classification models for diagnosis of cancer recurrence.

Also, each developed model would require further validation by comparing it to existing models and/or verifying with an extensive testing set based on clinical research, which is outside the scope of this study. Additionally, each of these models are capable of differentiating multi-class scenarios with higher feature set dimensionality. However, we only focused on the differentiation for the binary case (two classes) with lower dimension feature sets (i.e. 2D, 3D) in order to provide visual representation of each model.

CHAPTER 7

CONCLUSION

7.1 Summary

The purpose of this work is the development of a sensing platform utilizing zinc oxide (ZnO) surface mount resonators (SMR) for cancer biomarker detection. The ultimate goal of this work is for the creation of a point-of-care (POC) system which can be operated by non-technical medical staff for proactive patient screening of terminal diseases such as cancer. The design of the device housing module incorporates both the high frequency microelectromechanical (MEM) devices and a separation of the fluidics needed for the proper interrogation of patient samples in real time. The following is a list of specific contributions attributed to the author for this work.

7.2 Contributions

- Designed an array configuration of ZnO SMR devices for liquid phase applications. Wafer dies were fabricated, diced and wire bonded using Georgia Tech's cleanroom facilities.

- Performed both a simulated and experimental verification for using USB 3.0A connectors as a nine-port radio frequency device characterization bus.

- Designed and optimized a fluidics chamber module utilizing the differential evolution algorithm. The module design was then fabricated using additive manufacturing (3D printing).

- Verified device operation within the fully packaged system (ZnO SMR array, USB 3.0, and fluidics chamber) for the detection of FITC with immobilized antibodies.

- Developed a protocol for the formulating pattern recognition models for antibody sensing applications. Each model is developed by classifying a training data set into

classes, e.g., cancer recurrence or remission.

7.3 Future Work

For this thesis, all chemical functionalization has been completely dependent on self-assembling monolayers [88]. Typically these layers suffer from their lack of selectivity without properly blocking unoccupied regions. There are many other protocols for device functionalization utilizing gels, solid support bilayers and other layers to immobilize selective biological materials, for example, aptamers, DNA, and different types of proteins. Several protocols should be selected to assess for their ability to improve device selectivity as ZnO SMR can be top coated with any necessary substrate material.

With the use of a characterization bus, each electrical signal can either be isolated or combined. Additionally with resonator sensing devices, analytical information is extracted from shifts in the resonate frequency. Therefore, it is advantageous for the design of a wideband characterization technique such as a network analyzer which can monitor multiple devices at once for large resonance shifts. However, network analyzers are bulky and expensive for system integration. Farasat et al. [91] examined the possibility of using a white noise source for wideband and low cost simultaneous characterization of multiple devices. The implementation of such a system would be essential to the design of a point-of-care system.

For the frequency range of ZnO SMR between 0.5 - 4.0 GHz, there can be electrical issues that compromise the signal integrity. One such issue is the transmission line insertion losses throughout the path of the signal from characterization instrument to the unit under test. On the wafer die, the Bragg reflector serves as a complicated substrate with an interchange of dielectric and conductive materials. An analytical study would need to be performed to develop a model to design electrical long (> 1 mm) signal pathways on the wafer die.

After the aforementioned suggestions are implemented, a full point-of-care system

should be feasible. This system would need to be fully designed tested and verified for robustness in different settings. Subsequently, the system can be distributed to medical facilities in order to perform clinical studies. Depending on the patient population, the initial data can be used as a training set for developing classification models dependent on a particular disease using the protocol presented in Chapter 6.

APPENDIX A

SUPPLEMENTAL DATA

The following section provides additional plots and data to further expound upon the work presented in this dissertation. Each section provides supplement information for the denoted chapter, primary for the benefit of the reader or any future researchers looking to continue the work of this project.

A.1 Chapter 3

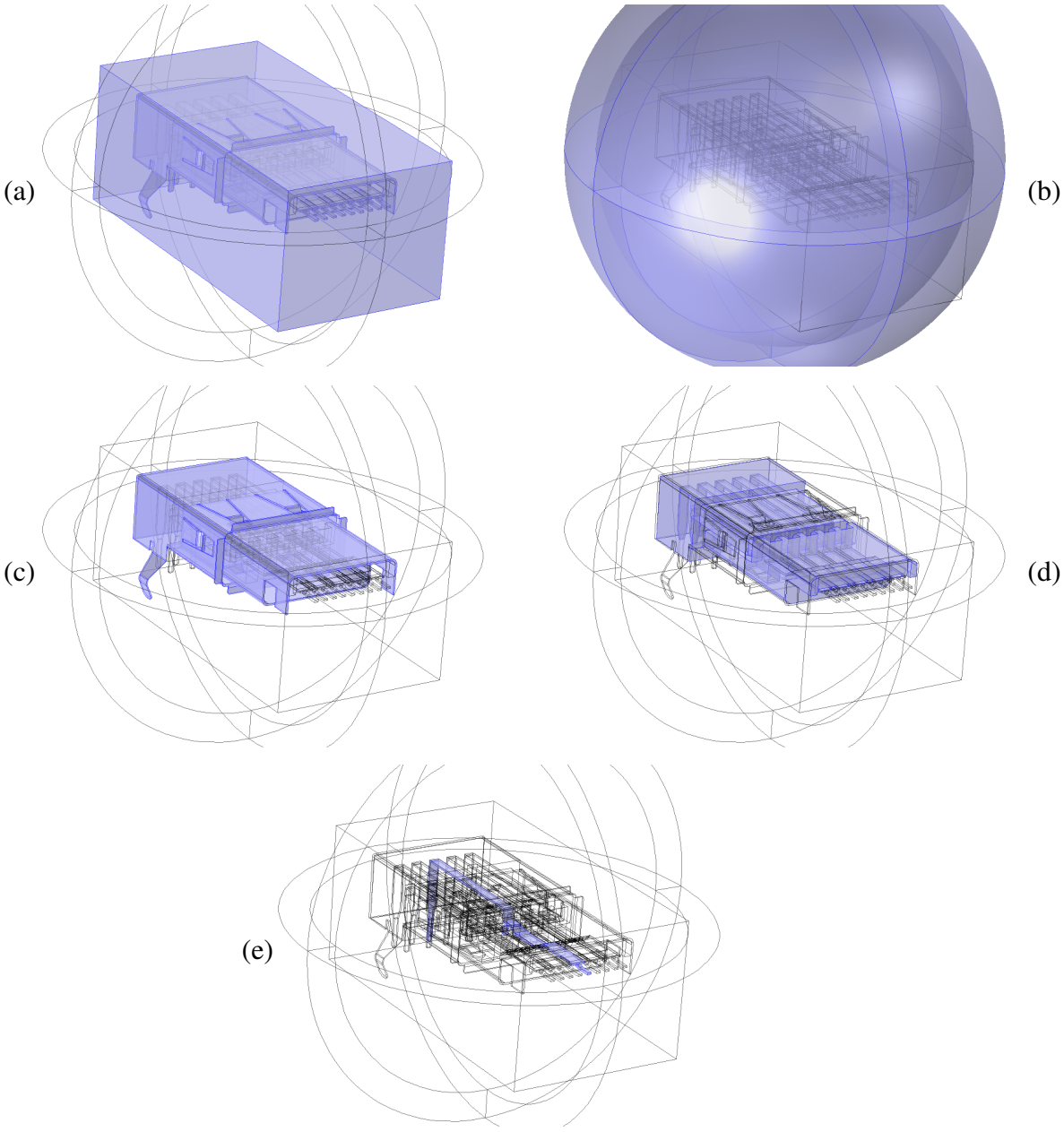

Figure 44: 3D regions for the FEM CAD model. Each image denotes a different region defined for the solution. The (a) cubic region in which all metal traces are subtracted to solve for the electric field outside of all conductors. The (b) surrounding sphere which a matched boundary condition is applied to assume the far field beyond this point does not affect the solution. The (c) outer shell of the connector serves as the ground and (d) the internal housing region where the LCP permittivity value is applied. Lastly, an (e) example electrical trace that has the terminal condition applied to solve for the capacitance of the complete trace.

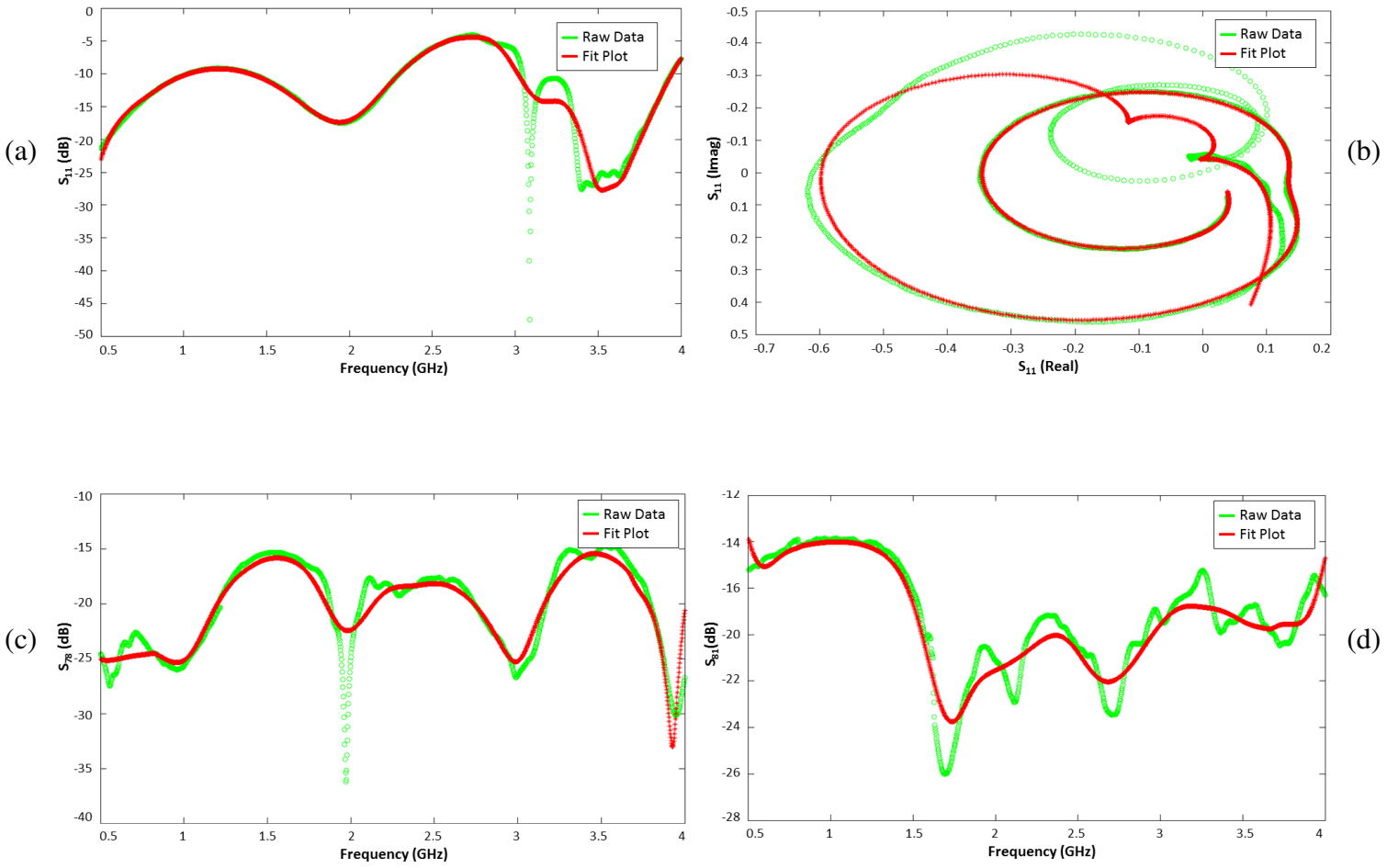

Figure 45: Example characterization plots to which a smoothing algorithm was applied for removal of resonances from measured values; in order to properly obtain capacitance values from wideband S-parameter data. Raw data plots were processed with Matlab's smooth function selecting a window size of 301 points (out of 1601) and a local regression 2^{nd} degree polynomial model. The S_{11} data is displayed with both (a) magnitude and (b) real-imaginary plots. In addition, several plots from other ports are provided, such as (c) S_{78} and (d) S_{81} magnitude plots.

(a)

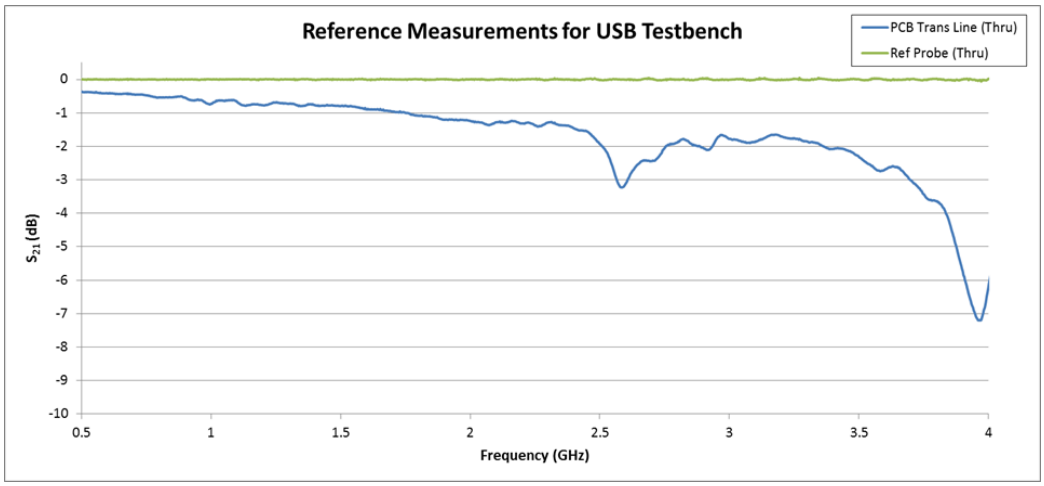

(b)

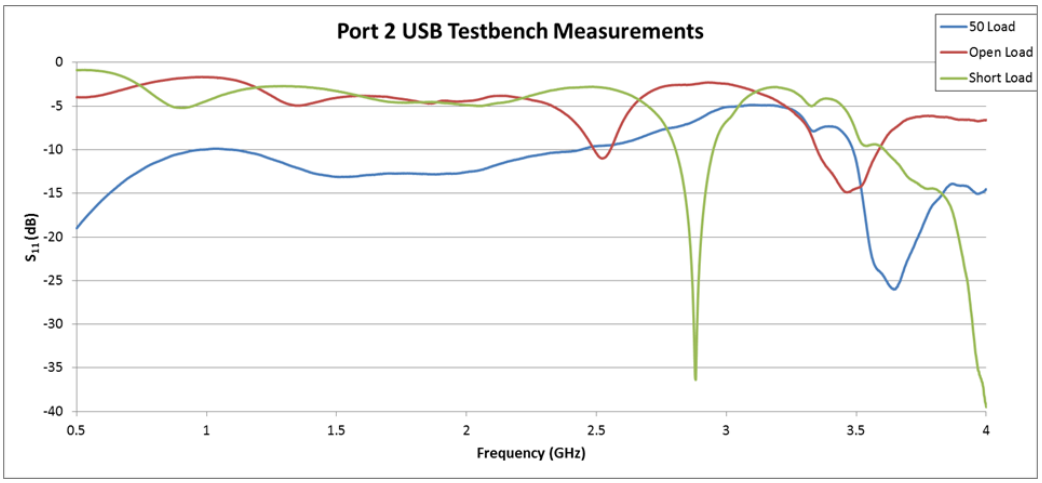

(c)

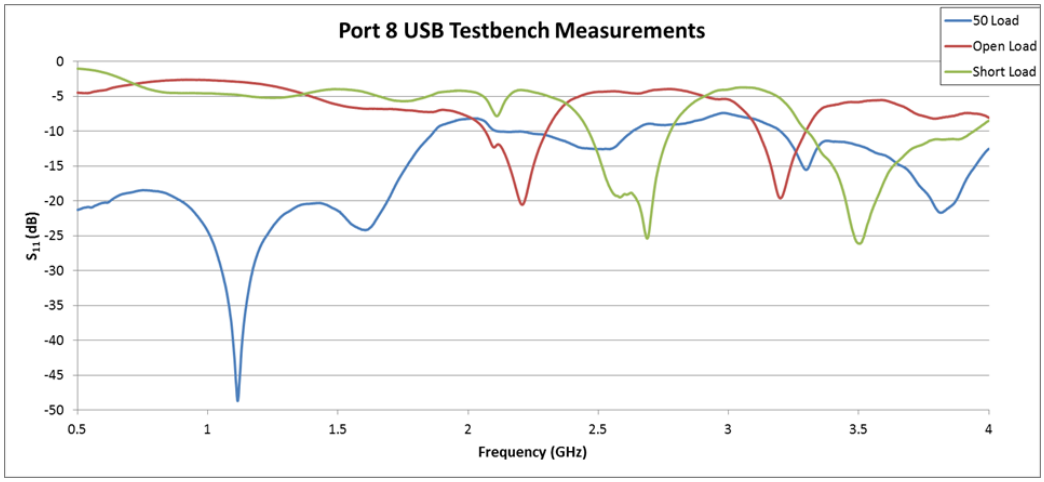

Figure 46: Wideband characterization plots for the USB testbench. The S_{21} measurements for the (a) coax connector of the network analyzer and a reference transmission line on the PCB illustrates the effects caused by the board. An example wideband S_{11} characterization plot of (b) port 2 and (c) port 8 with various types of line termination. The resonant peaks that hinder the operation range of the USB 3.0 seem to be correlated to the parasitics of the termination.

A.2 Chapter 5

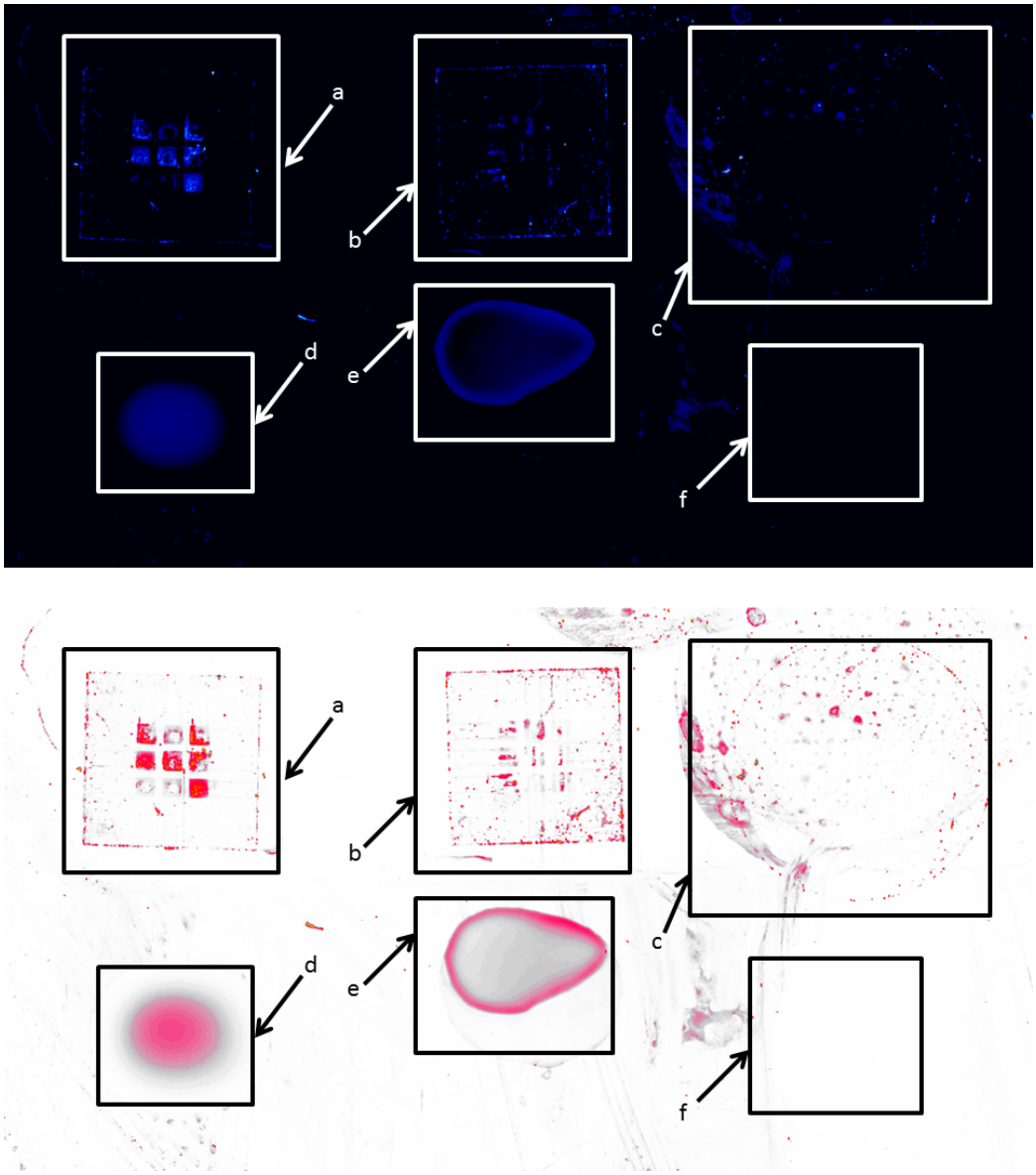

Figure 47: Two versions of the complete fluorescence image captured by the GE Typhoon™ Trio Plus system. The image was taken after each device was treated with the surface functionalization steps outlined in section 5.2 and exposure to the target antigen (FITC 1mM). The devices shown are (a) MM ZnO SMR, (b) LFE ZnO SMR and (c) QCM BAW resonators. The image is accompanied with droplets of (d) FITC 1mM in PBS, (e) PBS buffer solution, and (f) DI water droplet. The image signature of the PBS buffer solution droplet can be due to contamination or the existence of another product with fluorescent properties.

(a)

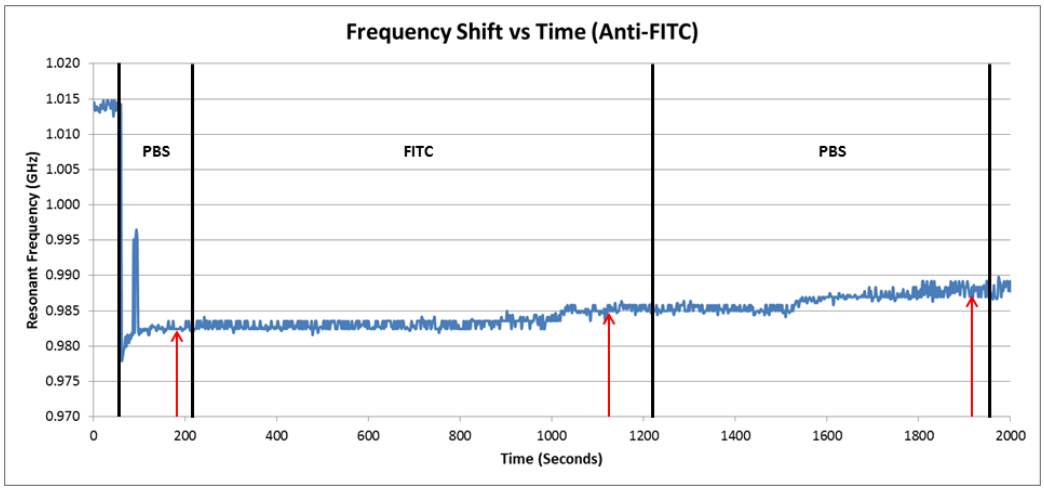

(b)

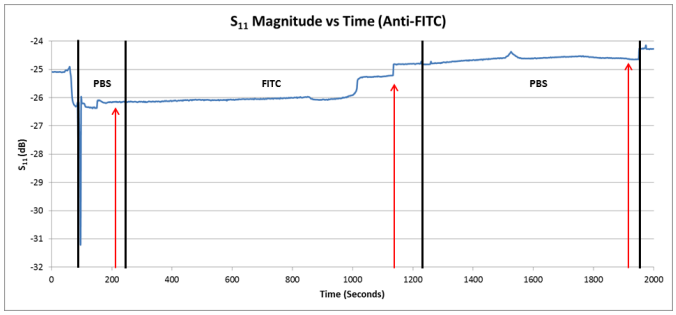

(c)

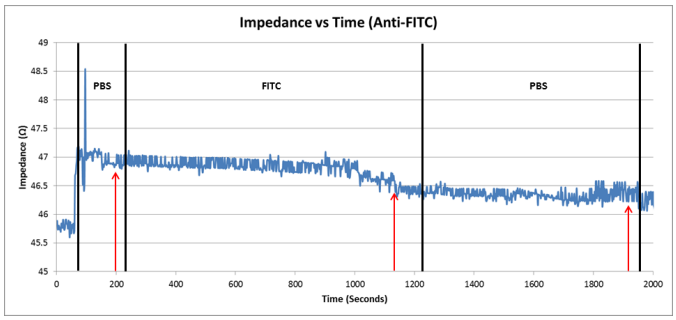

(d)

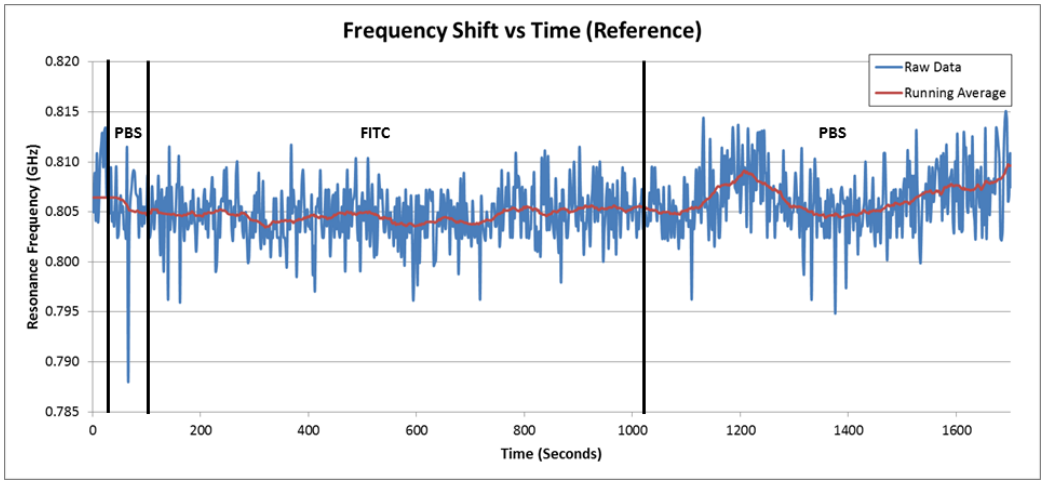

Figure 48: S_{11} resonant frequency property shifts verses time for each device. The plots are correlated to the (a) operational frequency, (b) energy level of the peak, and (c) magnitude of impedance for the functionalized device (anti-FITC) and the (d) operational frequency of the reference sensor. Regions are denoted on each plot to show what solution was exposed to the sensor during that time period. The arrows on each plot of the functionalized device shows the time which the measurement was halted to measure the other devices on the test bench. This interruption in the measurement may have contributed to the upward drift in the resonant frequency toward the end of the experiment.

A.3 Chapter 6

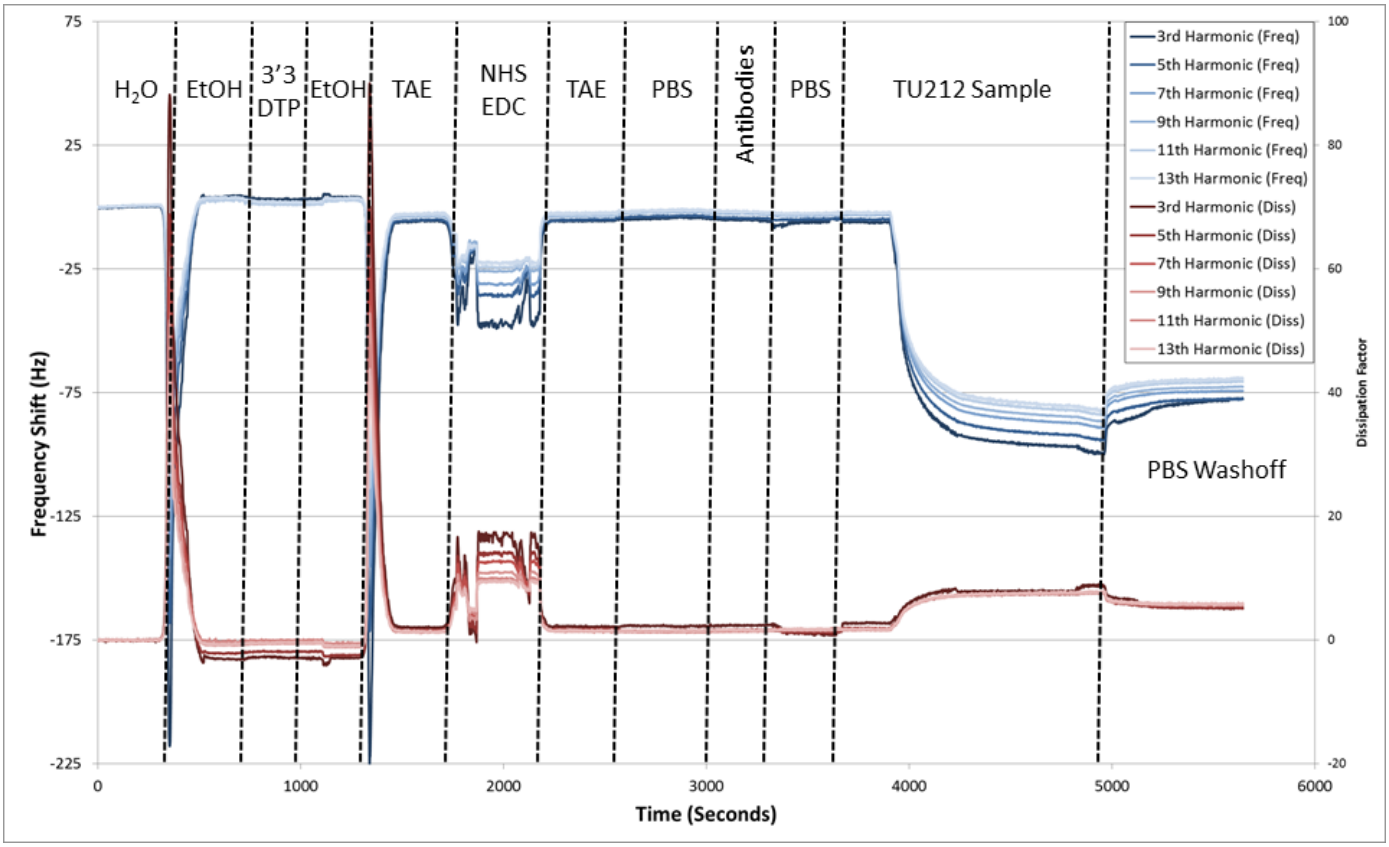

Figure 49: An example of the resonant frequency shift over time plot from one of the QCM-D sensors used in the experiment. Each device had a total of 7 harmonic resonant frequencies measured in real time (sampling rate $\approx$ 1 Hz) of the device recording both frequency and dissipation factor shift values. The exposed solution for the sensor is denoted on the plot to describe the cause of any features in the plot.

Table 21: Complete data selected for creating the classification models

2D Model											
Feature	Harmonic	SCC47 Trial 1	SCC47 Trial 2	SCC47 Trial 3	Mean	SD	TU212 Trial 1	TU212 Trial 2	TU212 Trial 3	Mean	SD
Initial Loading Slope	pAkt 7th	-0.957	-0.605	-0.777	-0.780	0.176	-0.862	-0.900	-1.132	-0.964	0.146
Initial Loading Slope	β-Actin 11th	-0.837	-0.825	-0.901	-0.854	0.040	-1.193	-1.019	-1.187	-1.133	0.099

3D Model											
Feature	Harmonic	SCC47 Trial 1	SCC47 Trial 2	SCC47 Trial 3	Mean	SD	TU212 Trial 1	TU212 Trial 2	TU212 Trial 3	Mean	SD
Equilibrium Slope	pHistone 9th	1.858	2.732	0.963	1.851	0.885	-0.217	0.853	0.765	0.467	0.594
Regular Freq Shift	pAkt 5th	0.216	1.771	0.301	0.763	0.874	10.38	0.501	3.388	4.757	5.081
Dissolution Slope	pHistone 7th	0.450	0.309	0.751	0.504	0.226	-0.514	0.163	0.046	-0.101	0.361

GMM Model											
Feature	Harmonic	SCC47 Trial 1	SCC47 Trial 2	SCC47 Trial 3	Mean	SD	TU212 Trial 1	TU212 Trial 2	TU212 Trial 3	Mean	SD
Equilibrium Slope	3rd	1.832	2.276	1.077	1.728	0.606	-0.252	1.410	0.800	0.653	0.840
	5th	1.793	2.680	1.012	1.828	0.834	-0.413	1.438	0.629	0.551	0.928
	7th	2.091	2.515	0.989	1.865	0.788	-0.199	1.108	0.853	0.588	0.692
	9th	1.858	2.732	0.963	1.851	0.885	-0.217	0.853	0.766	0.467	0.594
	11th	1.708	2.578	0.987	1.757	0.797	-0.477	1.052	0.607	0.394	0.787
Initial Loading Slope	3rd	1.208	0.632	0.654	0.831	0.326	2.021	-0.640	0.494	0.625	1.335
	5th	1.265	0.609	0.719	0.865	0.352	2.182	-0.649	0.615	0.716	1.418
	7th	1.291	0.579	0.699	0.856	0.381	2.004	-0.644	0.513	0.624	1.327
	9th	1.253	0.560	0.677	0.830	0.371	1.935	-0.644	0.633	0.641	1.290
	11th	1.160	0.542	0.681	0.794	0.324	1.594	-0.548	0.192	0.413	1.088
Regular Freq Shift	3rd	0.245	0.461	-2.913	-0.736	1.888	144.7	-0.060	0.844	48.55	83.41
	5th	0.196	0.514	-2.293	-0.528	1.537	52.25	0.011	0.796	17.69	29.94
	7th	0.141	0.878	-2.131	-0.371	1.568	49.75	-0.033	0.792	16.84	28.51
	9th	0.126	0.538	-2.317	-0.550	1.543	49.57	-0.001	0.739	16.77	28.41
	11th	0.084	0.797	-2.036	-0.385	1.474	64.37	0.077	0.322	21.59	37.05
Max-Min Freq Shift	3rd	-0.185	-6.215	4.092	-0.770	5.178	8.640	1.126	0.040	3.269	4.683
	5th	-0.236	-3.766	4.760	0.252	4.284	6.542	0.775	0.164	2.493	3.519
	7th	-0.191	-6.797	2.717	-1.424	4.875	6.001	1.296	0.244	2.514	3.066
	9th	-0.200	-4.156	3.753	-0.201	3.955	5.995	1.497	0.205	2.566	3.040
	11th	-0.207	-10.63	3.588	-2.416	7.360	6.318	-1.316	-0.180	1.607	4.119

REFERENCES

[1] A. Jemal, R. Siegel, J. Xu, and E. Ward, "Cancer statistics, 2010," *CA: a cancer journal for clinicians*, vol. 60, no. 5, pp. 277–300, 2010.

[2] P. Muralt, *Piezoelectric Films for Innovations in the Field of MEMS and Biosensors*, pp. 351–376. Springer, 2008.

[3] A. Ballato, "Modeling piezoelectric and piezomagnetic devices and structures via equivalent networks," *IEEE transactions on ultrasonics, ferroelectrics, and frequency control*, vol. 48, no. 5, pp. 1189–1240, 2001.

[4] F. Munir, A. Wathen, and W. Hunt, "A ghz range, single structure, multi-mode zno solidly-mounted bulk acoustic resonator," in *Ultrasonics Symposium (IUS), 2010 IEEE*, pp. 853–856, IEEE, 2010.

[5] L. Li, S. Chen, S. Oh, and S. Jiang, "In situ single-molecule detection of antibody-antigen binding by tapping-mode atomic force microscopy," *Analytical chemistry*, vol. 74, no. 23, pp. 6017–6022, 2002.

[6] V. Franc and V. Hlav, "An iterative algorithm learning the maximal margin classifier," *Pattern Recognition*, vol. 36, no. 9, pp. 1985–1996, 2003.

[7] E. Engvall and P. Perlmann, "Enzyme-linked immunosorbent assay (elisa) quantitative assay of immunoglobulin g," *Immunochemistry*, vol. 8, no. 9, pp. 871–874, 1971.

[8] J. M. Faupel-Badger, B. J. Fuhrman, X. Xu, R. T. Falk, L. K. Keefer, T. D. Veenstra, R. N. Hoover, and R. G. Ziegler, "Comparison of liquid chromatography-tandem mass spectrometry, ria, and elisa methods for measurement of urinary estrogens," *Cancer Epidemiology Biomarkers & Prevention*, vol. 19, no. 1, pp. 292–300, 2010.

[9] S. P. Mohanty and E. Kougianos, "Biosensors: a tutorial review," *Potentials, IEEE*, vol. 25, no. 2, pp. 35–40, 2006.

[10] P. Vadgama and P. W. Crump, "Biosensors: recent trends. a review," *Analyst*, vol. 117, no. 11, pp. 1657–1670, 1992.

[11] Y.-K. Yen, C.-Y. Huang, C.-H. Chen, C.-M. Hung, K.-C. Wu, C.-K. Lee, J.-S. Chang, S. Lin, and L.-S. Huang, "A novel, electrically protein-manipulated microcantilever biosensor for enhancement of capture antibody immobilization," *Sensors and Actuators B: Chemical*, vol. 141, no. 2, pp. 498–505, 2009.

[12] C. Ricciardi, S. Fiorilli, S. Bianco, G. Canavese, R. Castagna, I. Ferrante, G. Digregorio, S. L. Marasso, L. Napione, and F. Bussolino, "Development of microcantilever-based biosensor array to detect angiopoietin-1, a marker of tumor angiogenesis," *Biosensors and Bioelectronics*, vol. 25, no. 5, pp. 1193–1198, 2010.

[13] S. Sang, Y. Zhao, W. Zhang, P. Li, J. Hu, and G. Li, "Surface stress-based biosensors," *Biosensors and Bioelectronics*, vol. 51, pp. 124–135, 2014.

[14] B. N. Johnson and R. Mutharasan, "Biosensing using dynamic-mode cantilever sensors: a review," *Biosensors and Bioelectronics*, vol. 32, no. 1, pp. 1–18, 2012.

[15] D. Virzonis, G. Vanagas, A. Ramanaviciene, A. Makaraviciute, D. Barauskas, A. Ramanavicius, W. Wen, and R. Kodzius, "Resonant gravimetric immunosensing based on capacitive micromachined ultrasound transducers," *Microchimica Acta*, pp. 1–9, 2014.

[16] A. Ramanaviciene, D. Virzonis, G. Vanagas, and A. Ramanavicius, "Capacitive micromachined ultrasound transducer (cmut) for immunosensor design," *Analyst*, vol. 135, no. 7, pp. 1531–1534, 2010.

[17] J. Andle and J. Vetelino, "Acoustic wave biosensors," *Sensors and Actuators A: Physical*, vol. 44, no. 3, pp. 167–176, 1994.

[18] E. Berkenpas, S. Bitla, P. Millard, and M. P. da Cunha, "Pure shear horizontal saw biosensor on langasite," *Ultrasonics, Ferroelectrics and Frequency Control, IEEE Transactions on*, vol. 51, no. 11, pp. 1404–1411, 2004.

[19] J. K. Perng, W. D. Hunt, and P. J. Edmonson, "Development of a shear horizontal saw rfid biosensor," in *Sensors, 2007 IEEE*, pp. 691–694, IEEE.

[20] L. Fertier, M. Cretin, M. Rolland, J.-O. Durand, L. Raehm, R. Desmet, O. Melnyk, C. Zimmermann, C. Djous, and D. Rebire, "Love wave immunosensor for antibody recognition using an innovative semicarbazide surface functionalization," *Sensors and Actuators B: Chemical*, vol. 140, no. 2, pp. 616–622, 2009.

[21] N. Moll, E. Pascal, D. H. Dinh, J.-P. Pillot, B. Bennetau, D. Rebire, D. Moynet, Y. Mas, D. Mossalayi, J. Pistr, and C. Djous, "A love wave immunosensor for whole e. coli bacteria detection using an innovative two-step immobilisation approach," *Biosensors and Bioelectronics*, vol. 22, no. 910, pp. 2145–2150, 2007.

[22] K. Kalantar-Zadeh, W. Wlodarski, Y. Y. Chen, B. N. Fry, and K. Galatsis, "Novel love mode surface acoustic wave based immunosensors," *Sensors and Actuators B: Chemical*, vol. 91, no. 1, pp. 143–147, 2003.

[23] G. Sauerbrey, "Use of quartz vibration for weighing thin films on a microbalance," *J. Physik*, vol. 155, pp. 206–212, 1959.

[24] B. Becker and M. A. Cooper, "A survey of the 20062009 quartz crystal microbalance biosensor literature," *Journal of Molecular Recognition*, vol. 24, no. 5, pp. 754–787, 2011.

[25] F. Hk, M. Rodahl, P. Brzezinski, and B. Kasemo, "Energy dissipation kinetics for protein and antibody-antigen adsorption under shear oscillation on a quartz crystal microbalance," *Langmuir*, vol. 14, no. 4, pp. 729–734, 1998.

[26] M. Rodahl, F. Hook, A. Krozer, P. Brzezinski, and B. Kasemo, "Quartz crystal microbalance setup for frequency and q-factor measurements in gaseous and liquid," *Review of Scientific Instruments*, vol. 66, no. 7, p. 3924, 1995. Rodahl, Michael Hook, Fredrik Krozer, Anatol Brzezinski, Peter Kasemo, Bengt; Source Info: Jul1995, Vol. 66 Issue 7, p3924; Subject Term: QUARTZ crystal microbalances; Subject Term: MICROBALANCES; Subject Term: QUARTZ crystals; Number of Pages: 7p; Illustrations: 4 Diagrams, 6 Graphs; Document Type: Article.

[27] G. Wingqvist, J. Bjurstrm, A. C. Hellgren, and I. Katardjiev, "Immunosensor utilizing a shear mode thin film bulk acoustic sensor," *Sensors and Actuators B: Chemical*, vol. 127, no. 1, pp. 248–252, 2007.

[28] Z. Yan, X. Y. Zhou, G. K. H. Pang, T. Zhang, W. L. Liu, J. G. Cheng, Z. T. Song, S. L. Feng, L. H. Lai, J. Z. Chen, and Y. Wang, "Zno-based film bulk acoustic resonator for high sensitivity biosensor applications," *Applied Physics Letters*, vol. 90, no. 14, pp. –, 2007.

[29] J. Curie and P. Curie, "An oscillating quartz crystal mass detector," *Rendu*, vol. 91, pp. 294–297, 1880.

[30] W. D. Hunt, D. D. Stubbs, and S.-H. Lee, "Time-dependent signatures of acoustic wave biosensors," *Proceedings of the IEEE*, vol. 91, no. 6, pp. 890–901, 2003.

[31] S. Butterworth, "On a null method of testing vibration galvanometers," *Proceedings of the Physical Society of London*, vol. 26, no. 1, p. 264, 1913.

[32] K. Van Dyke, "The piezo-electric resonator and its equivalent network," *Radio Engineers, Proceedings of the Institute of*, vol. 16, no. 6, pp. 742–764, 1928.

[33] Z. Yan and X.-j. Zhou, "Simulation of zno based film bulk acoustic resonator by modified butterworth-van dyke model," in *Piezoelectricity, Acoustic Waves and Device Applications (SPAWDA), 2010 Symposium on*, pp. 491–496, IEEE, 2010.

[34] F. Nye, *Physical properties of crystals*. Clarendon Press Oxford, 1964.

[35] G. Heckmann, "The lattice theory of solids," *Ergeb. exakt. Naturwiss*, vol. 4, pp. 100–153, 1925.

[36] A. D. Wathen, F. Munir, and W. D. Hunt, "Trapped hybrid modes in solidly mounted resonators based on c-axis oriented hexagonal crystals," *Journal of Applied Physics*, vol. 108, no. 11, p. 114503, 2010.

[37] W. Newell, "Face-mounted piezoelectric resonators," *Proceedings of the IEEE*, vol. 53, no. 6, pp. 575–581, 1965.

[38] C. D. Corso, A. Dickherber, and W. D. Hunt, "Lateral field excitation of thickness shear mode waves in a thin film zno solidly mounted resonator," *Journal of Applied Physics*, vol. 101, no. 5, p. 054514, 2007.

[39] J. R. Prensner, M. A. Rubin, J. T. Wei, and A. M. Chinnaiyan, "Beyond psa: the next generation of prostate cancer biomarkers," *Science translational medicine*, vol. 4, no. 127, pp. 127rv3–127rv3, 2012.

[40] F. Martin, P. Muralt, M.-A. Dubois, and A. Pezous, "Thickness dependence of the properties of highly c-axis textured aln thin films," *Journal of Vacuum Science and Technology A*, vol. 22, no. 2, pp. 361–365, 2004.

[41] S. Krishnaswamy, B. McAvoy, W. Takei, and R. Moore, "Oriented zno films for microwave shear mode transducers," in *1982 Ultrasonics Symposium*, pp. 476–479, IEEE, 1982.

[42] B.-H. Seo, S.-H. Lee, J. H. Seo, J.-H. Jeon, and H. Choe, "Study on the wet etch behavior of a zinc-oxide semiconductor in acid solutions," *Journal of the Korean Physical Society*, vol. 53, no. 1, pp. 402–405, 2008.

[43] U. S. B. Specification, "Revision 3.0, 2013," *Compaq Computer Corporation, Hewlett-Packard Company, Intel Corporation, Lucent Technologies Inc, Microsoft Corporation, NEC Corporation, Koninklijke Philips Electronics NV*.

[44] "3d cad design software solidworks," 2014. Internet: http://www.solidworks.com/.

[45] C. Warner, "Usb connector 3.0 - a female type, dip 90' 15d', for pcb mount," 2011.

[46] C. Warner, "Usb connector 3.0 - smt low profile, a male type 15u", for pcb mount," 2011.

[47] "Comsol multiphysics," 2014. Internet: http://www.comsol.com/.

[48] "Introduction to the ac/dc module," 2012.

[49] S. Musa and M. Sadiku, "Fast computation of capacitance matrix and potential distribution for multiconductor in non-homogenous multilayered dielectric media," *Proc. COSMOL*, 2009.

[50] A. Suntives, A. Khajooeizadeh, and R. Abhari, "Using via fences for crosstalk reduction in pcb circuits," in *IEEE International Symposium on Electromagnetic Compatibility*, vol. 1, pp. 34–37, Kluwer Academic.

[51] B. Young and A. K. Sparkman, "Measurement of package inductance and capacitance matrices," *Components, Packaging, and Manufacturing Technology, Part B: Advanced Packaging, IEEE Transactions on*, vol. 19, no. 1, pp. 225–229, 1996.

[52] J. M. Faupel-Badger, B. J. Fuhrman, X. Xu, R. T. Falk, L. K. Keefer, T. D. Veenstra, R. N. Hoover, and R. G. Ziegler, "Comparison of liquid chromatography-tandem mass spectrometry, ria, and elisa methods for measurement of urinary estrogens," *Cancer Epidemiology Biomarkers and Prevention*, vol. 19, no. 1, pp. 292–300, 2010.

[53] J. S. Lee, B. Ettinger, F. Z. Stanczyk, E. Vittinghoff, V. Hanes, J. A. Cauley, W. Chandler, J. Settlage, M. S. Beattie, and E. Folkerd, "Comparison of methods to measure low serum estradiol levels in postmenopausal women," *The Journal of Clinical Endocrinology and Metabolism*, vol. 91, no. 10, pp. 3791–3797, 2006.

[54] J. F. Rusling, C. V. Kumar, J. S. Gutkind, and V. Patel, "Measurement of biomarker proteins for point-of-care early detection and monitoring of cancer," *Analyst*, vol. 135, no. 10, pp. 2496–2511, 2010.

[55] R. Storn and K. Price, "Differential evolutiona simple and efficient heuristic for global optimization over continuous spaces," *Journal of global optimization*, vol. 11, no. 4, pp. 341–359, 1997.

[56] K. V. Price, R. M. Storn, and J. A. Lampinen, "Differential evolution a practical approach to global optimization," 2005.

[57] R. Storn and K. Price, "Differential evolution (de) for continuous function optimization," 2013.

[58] K. Deb, "Multi-objective optimization," *Multi-objective optimization using evolutionary algorithms*, pp. 13–46, 2001.

[59] "3d cad design software solidworks," 2014. Internet: http://www.solidworks.com/.

[60] "Flow simulation 2012 technical reference," Waltham, MA, 2012.

[61] G. M. Whitesides, "The origins and the future of microfluidics," *Nature*, vol. 442, no. 7101, pp. 368–373, 2006. 10.1038/nature05058.

[62] O. Reynolds, "An experimental investigation of the circumstances which determine whether the motion of water shall be direct or sinuous, and of the law of resistance in parallel channels. [abstract]," *Proceedings of the Royal Society of London*, vol. 35, pp. 84–99, 1883.

[63] J. E. Matsson, *An Introduction to SolidWorks Flow Simulation 2013*. SDC Publications, 2013.

[64] "3d printer site," 2014. Internet: http://www.stratasys.com/3d-printers/design-series/precision/objet-eden260v.

[65] S. Mobley and W. Hunt, "Electrical characterization of universal serial bus (usb) 3.0 a for radio frequency circuitry applications," *Unpublished*, 2015.

[66] "Ceramic pin grid array (cpga) - ceramic pga - ntk technologies inc.," 2014.

[67] C. LLC, "Pbs (phosphate-buffered saline)," 2015. Internet: http://www.researchgate.net/.

[68] "Fluorescein sodium salt used as fluorescent tracer," 2015. Internet: http://www.sigmaaldrich.com/catalog/product/sial/f6377?lang=en&region=US.

[69] "Technical support in antibody basics — sigma-aldrich," 2015. Internet: http://www.sigmaaldrich.com/life-science/cell-biology/antibodies/learning-center/antibody-explorer/technical-support/antibody-basics.html.

[70] "Fluorescein isothiocyanate (spiro form) — c21h11no5s — chemspider," 2015. Internet: http://www.chemspider.com/Chemical-Structure.2043359.html.

[71] Y. Liu, "Some consideration on the langmuir isotherm equation," *Colloids and Surfaces A: Physicochemical and Engineering Aspects*, vol. 274, no. 1, pp. 34–36, 2006.

[72] P. Skldal, "Piezoelectric quartz crystal sensors applied for bioanalytical assays and characterization of affinity interactions," *Journal of the Brazilian Chemical Society*, vol. 14, no. 4, pp. 491–502, 2003.

[73] R. A. Vijayendran and D. E. Leckband, "A quantitative assessment of heterogeneity for surface-immobilized proteins," *Analytical Chemistry*, vol. 73, no. 3, pp. 471–480, 2001.

[74] M. Gillison, W. Koch, R. Capone, M. Spafford, W. Westra, L. Wu, M. Zahurak, R. Daniel, M. Viglione, and D. Symer, "Evidence for a causal association between human papillomavirus and a subset of head and neck cancers," *Journal of the National Cancer Institute*, vol. 92, no. 9, pp. 709–720, 2000.

[75] A. Kreimer, G. Clifford, P. Boyle, and S. Franceschi, "Human papillomavirus types in head and neck squamous cell carcinomas worldwide: a systematic review," *Cancer Epidemiology Biomarkers and Prevention*, vol. 14, no. 2, pp. 467–475, 2005.

[76] K. Ang, J. Harris, R. Wheeler, R. Weber, D. Rosenthal, P. Nguyen-T¢n, W. Westra, C. Chung, R. Jordan, and C. Lu, "Human papillomavirus and survival of patients with oropharyngeal cancer," *New England Journal of Medicine*, vol. 363, no. 1, pp. 24–35, 2010.

[77] P. Lassen, J. Eriksen, S. Hamilton-Dutoit, T. Tramm, J. Alsner, and J. Overgaard, "Effect of hpv-associated p16ink4a expression on response to radiotherapy and survival in squamous cell carcinoma of the head and neck," *Journal of Clinical Oncology*, vol. 27, no. 12, pp. 1992–1998, 2009.

[78] A. Gupta, W. McKenna, C. Weber, M. Feldman, J. Goldsmith, R. Mick, M. Machtay, D. Rosenthal, V. Bakanauskas, and G. Cerniglia, "Local recurrence in head and neck cancer relationship to radiation resistance and signal transduction," *Clinical Cancer Research*, vol. 8, no. 3, pp. 885–892, 2002.

[79] A. Menegakis, A. Yaromina, W. Eicheler, A. Drfler, B. Beuthien-Baumann, H. Thames, M. Baumann, and M. Krause, "Prediction of clonogenic cell survival curves based on the number of residual dna double strand breaks measured by h2ax staining," *International journal of radiation biology*, vol. 85, no. 11, pp. 1032–1041, 2009.

[80] J. B. de Kok, R. W. Roelofs, B. A. Giesendorf, J. L. Pennings, E. T. Waas, T. Feuth, D. W. Swinkels, and P. N. Span, "Normalization of gene expression measurements in tumor tissues: comparison of 13 endogenous control genes," *Laboratory investigation*, vol. 85, no. 1, pp. 154–159, 2004.

[81] M. S. Pepe, R. Etzioni, Z. Feng, J. D. Potter, M. L. Thompson, M. Thornquist, M. Winget, and Y. Yasui, "Phases of biomarker development for early detection of cancer," *Journal of the National Cancer Institute*, vol. 93, no. 14, pp. 1054–1061, 2001.

[82] W.-B. Tsai, J. M. Grunkemeier, and T. A. Horbett, "Variations in the ability of adsorbed fibrinogen to mediate platelet adhesion to polystyrene-based materials: A multivariate statistical analysis of antibody binding to the platelet binding sites of fibrinogen," *Journal of Biomedical Materials Research Part A*, vol. 67A, no. 4, pp. 1255–1268, 2003.

[83] M. S. Wagner and D. G. Castner, "Characterization of adsorbed protein films by time-of-flight secondary ion mass spectrometry with principal component analysis," *Langmuir*, vol. 17, no. 15, pp. 4649–4660, 2001.

[84] V. Franc and V. Hlavc, "Statistical pattern recognition toolbox for matlab," *Prague, Czech: Center for Machine Perception, Czech Technical University*, 2004.

[85] P. Paalanen, J.-K. Kamarainen, J. Ilonen, and H. Klviinen, "Feature representation and discrimination based on gaussian mixture model probability densitiespractices and algorithms," *Pattern Recognition*, vol. 39, no. 7, pp. 1346–1358, 2006.

[86] B. Kozinec, "Recurrent algorithm separating convex hulls of two sets," *Learning algorithms in pattern recognition*, pp. 43–50, 1973.

[87] C. Fraley and A. E. Raftery, "How many clusters? which clustering method? answers via model-based cluster analysis," *The computer journal*, vol. 41, no. 8, pp. 578–588, 1998.

[88] K. L. Prime and G. M. Whitesides, "Self-assembled organic monolayers: model systems for studying adsorption of proteins at surfaces," *Science (New York, N.Y.)*, vol. 252, no. 5010, pp. 1164–1167, 1991. Research Support, U.S. Gov't, Non-P.H.S.

[89] P. Skldal, "Piezoelectric quartz crystal resonators applied for immunosensing and affinity interaction studies," *Biosensors and Biodetection Methods and Protocols*, vol. 2, pp. 37–50, 2009.

[90] C. Poitras and N. Tufenkji, "A qcm-d-based biosensor for e. coli o157:h7 highlighting the relevance of the dissipation slope as a transduction signal," *Biosensors and Bioelectronics*, vol. 24, no. 7, pp. 2137–42, 2009. Poitras, Charles Tufenkji, Nathalie eng Research Support, Non-U.S. Gov't England 2009/01/03 09:00 Biosens Bioelectron. 2009 Mar 15;24(7):2137-42. Epub 2008 Nov 27.

[91] F. Munir, A. Wathen, and W. D. Hunt, "A new method for wideband characterization of resonator-based sensing platforms," *Review of scientific instruments*, vol. 82, no. 3, p. 035119, 2011.

[92] K. M. M. Aung, X. Ho, and X. Su, "Dna assembly on streptavidin modified surface: A study using quartz crystal microbalance with dissipation or resistance measurements," *Sensors and Actuators B: Chemical*, vol. 131, no. 2, pp. 371–378, 2008.

[93] A. Chaturvedi, E. Engels, W. Anderson, and M. Gillison, "Incidence trends for human papillomavirusrelated andunrelated oral squamous cell carcinomas in the united states," *Journal of Clinical Oncology*, vol. 26, no. 4, pp. 612–619, 2008.

[94] L. Civit, A. Fragoso, and C. K. O'Sullivan, "Electrochemical biosensor for the multiplexed detection of human papillomavirus genes," *Biosens Bioelectron*, vol. 26, no. 4, pp. 1684–7, 2010. Civit, L Fragoso, A O'Sullivan, C K eng Evaluation Studies Research Support, Non-U.S. Gov't England 2010/07/30 06:00 Biosens Bioelectron. 2010 Dec 15;26(4):1684-7. Epub 2010 Jul 7.

[95] D. Dell'Atti, M. Zavaglia, S. Tombelli, G. Bertacca, A. O. Cavazzana, G. Bevilacqua, M. Minunni, and M. Mascini, "Development of combined dna-based piezoelectric biosensors for the simultaneous detection and genotyping of high risk human papilloma virus strains," *Clin Chim Acta*, vol. 383, no. 1-2, pp. 140–6, 2007. Dell'Atti, Daniela Zavaglia, Michele Tombelli, Sara Bertacca, Gloria Cavazzana, Andrea O Bevilacqua, Generoso Minunni, Maria Mascini, Marco eng Validation Studies Netherlands 2007/06/19 09:00 Clin Chim Acta. 2007 Aug;383(1-2):140-6. Epub 2007 May 21.

[96] R. Gabl, H.-D. Feucht, H. Zeininger, G. Eckstein, M. Schreiter, R. Primig, D. Pitzer, and W. Wersing, "First results on label-free detection of dna and protein molecules using a novel integrated sensor technology based on gravimetric detection principles," *Biosensors and Bioelectronics*, vol. 19, no. 6, pp. 615–620, 2004.

[97] L. Garca-Gancedo, Z. Zhu, E. Iborra, M. Clement, J. Olivares, A. J. Flewitt, W. I. Milne, G. M. Ashley, J. K. Luo, X. B. Zhao, and J. R. Lu, "Aln-based baw resonators with cnt electrodes for gravimetric biosensing," *Sensors and Actuators B: Chemical*, vol. 160, no. 1, pp. 1386–1393, 2011.

[98] A. R. Grayson, R. S. Shawgo, A. M. Johnson, N. T. Flynn, Y. Li, M. J. Cima, and R. Langer, "A biomems review: Mems technology for physiologically integrated devices," *Proceedings of the IEEE*, vol. 92, no. 1, pp. 6–21, 2004.

[99] T. R. Holford, F. Davis, and S. P. Higson, "Recent trends in antibody based sensors," *Biosensors and Bioelectronics*, vol. 34, no. 1, pp. 12–24, 2012. Holford, Timothy R J Davis, Frank Higson, Seamus P J eng Research Support, Non-U.S. Gov't Review England 2012/03/06 06:00 Biosens Bioelectron. 2012 Apr 15;34(1):12-24. Epub 2011 Oct 20.

[100] N. V. Lavrik, M. J. Sepaniak, and P. G. Datskos, "Cantilever transducers as a platform for chemical and biological sensors," *Review of scientific instruments*, vol. 75, no. 7, pp. 2229–2253, 2004.

[101] C. R. Lowe, "An introduction to the concepts and technology of biosensors," *Biosensors*, vol. 1, no. 1, pp. 3–16, 1985.

[102] J. C. Pyun, H. Beutel, J. U. Meyer, and H. H. Ruf, "Development of a biosensor for e. coli based on a flexural plate wave (fpw) transducer," *Biosensors and Bioelectronics*, vol. 13, no. 78, pp. 839–845, 1998.

[103] X.-L. Su and Y. Li, "A self-assembled monolayer-based piezoelectric immunosensor for rapid detection of escherichia coli o157:h7," *Biosensors and Bioelectronics*, vol. 19, no. 6, pp. 563–574, 2004.

[104] O. Tigli, L. Bivona, P. Berg, and M. E. Zaghloul, "Fabrication and characterization of a surface-acoustic-wave biosensor in cmos technology for cancer biomarker detection," *Biomedical Circuits and Systems, IEEE Transactions on*, vol. 4, no. 1, pp. 62–73, 2010.

[105] J. Wang, "Electrochemical biosensors: Towards point-of-care cancer diagnostics," *Biosensors and Bioelectronics*, vol. 21, no. 10, pp. 1887–1892, 2006.

[106] Y. Wang, M. Chen, L. Zhang, Y. Ding, Y. Luo, Q. Xu, J. Shi, L. Cao, and W. Fu, "Rapid detection of human papilloma virus using a novel leaky surface acoustic wave peptide nucleic acid biosensor," *Biosens Bioelectron*, vol. 24, no. 12, pp. 3455–60, 2009. Wang, Yunxia Chen, Ming Zhang, Liqun Ding, Yi Luo, Yang Xu, Qinghua Shi, Jianfeng Cao, Liang Fu, Weiling eng Research Support, Non-U.S. Gov't England 2009/06/03 09:00 Biosens Bioelectron. 2009 Aug 15;24(12):3455-60. Epub 2009 May 3.

[107] A. D. Wathen, "Acoustic wave biosensor arrays for the simultaneous detection of multiple cancer biomarkers," 2011.

[108] Y. Wong, S. Ng, M. Ng, S. Si, S. Yao, and Y. Fung, "Immunosensor for the differentiation and detection of salmonella species based on a quartz crystal microbalance," *Biosensors and Bioelectronics*, vol. 17, pp. 676–684, 2001.

[109] L. Xu, H. Yu, M. S. Akhras, S. J. Han, S. Osterfeld, R. L. White, N. Pourmand, and S. X. Wang, "Giant magnetoresistive biochip for dna detection and hpv genotyping," *Biosens Bioelectron*, vol. 24, no. 1, pp. 99–103, 2008. Xu, Liang Yu,

Heng Akhras, Michael S Han, Shu-Jen Osterfeld, Sebastian White, Robert L Pourmand, Nader Wang, Shan X eng 1U54CA119367-01/CA/NCI NIH HHS/ P01-HG000205/HG/NHGRI NIH HHS/ U54 CA119367-010001/CA/NCI NIH HHS/ Research Support, N.I.H., Extramural Research Support, U.S. Gov't, Non-P.H.S. England 2008/05/07 09:00 Biosens Bioelectron. 2008 Sep 15;24(1):99-103. Epub 2008 Apr 8. Enough HPV Sensors...

[110] S. Yang and C. Chang, "A piezoresistive bridge-microcantilever biosensor by cmos process for surface stress measurement," *Sensors and Actuators B: Chemical*, vol. 145, no. 1, pp. 405–410, 2010.

[111] N. Zari, A. Amine, and M. M. Ennaji, "Label-free dna biosensor for electrochemical detection of short dna sequences related to human papilloma virus," *Analytical Letters*, vol. 42, no. 3, pp. 519–535, 2009.